LOADING AND STRUCTURAL RESPONSE MODELS FOR TRANSVERSE DEFLECTION OF CIRCULAR PLATES SUBJECTED TO NEAR FIELD EXPLOSIONS

BY ELAN BORENSTEIN

A dissertation submitted to the

Graduate School—New Brunswick

Rutgers, The State University of New Jersey

in partial fulfillment of the requirements

for the degree of

Doctor of Philosophy

Graduate Program in Mechanical and Aerospace Engineering

Written under the direction of

Dr. Haym Benaroya

and approved by

Haym Baruh
Husam Najm
Ellis Dill
Haym Benaroya

New Brunswick, New Jersey

October, 2010

ABSTRACT OF THE DISSERTATION

Loading and Structural Response Models for Transverse Deflection of Circular Plates Subjected to Near Field Explosions

by Elan Borenstein

Dissertation Director: Dr. Haym Benaroya

This dissertation develops loading and structural response models to estimate the elastic deformation of a circular plate due to near field explosions. The loading model generates the nonuniform loading characteristic of a near field explosion on a circular plate. This loading model is unique as it uses the TNT equivalence factors for pressure and impulse separately when deriving the pressure profile. Most loading models either average the two factors together or use only one of them.

An analytical model and two finite element models were developed to capture the response of the circular plate due to this nonuniform loading. The analytical model utilizes the von Kármán thin plate equations with a new assumed deformation profile developed in this dissertation. The typical deformation profile for a circular plate uses two constants to satisfy the boundary conditions. By adding torsional springs to the boundary of the plate and equating the springs' moment to the plate's internal moment, as well as carrying through with the von Kármán model, a new assumed profile is derived which has one parameter representing the boundary. This allows for a sensitivity analysis to be performed on the boundary condition parameter. In addition, this parameter has physical meaning, as it represents the stiffness of the torsional springs.

The two finite element models were created using ANSYS Workbench. One is a simplified model with a constant thickness, circular plate geometry while the other has the actual geometry of the plate used in the experiments. The finite element models were created in a way to allow for the spatial and time dependent pressure loadings to be applied to the proper surface.

Four experimental deformation data sets were provided by the U.S. Department of Homeland Security via the Transportation Security Laboratory. Each data set was compared to the analytical model and the two finite element models. The plate center deflection for the three structural models was found to be in good agreement with the experimental data. The results show that the loading becomes less accurate at very small scaled distances.

Using the analytical model, the sensitivity of the maximum plate center deflection to parameter changes was estimated. The maximum deflection was found to be most sensitive to plate thickness. In addition, the sensitivity of maximum deflection to parameter uncertainties was calculated for the loading parameters. Depending upon the loading configuration, the greatest sensitivity to maximum deflection was found to depend on the uncertainty of a different parameter. This can be attributed to the highly nonlinear nature of this model.

Acknowledgements

First and foremost, I acknowledge my research advisor Professor Haym Benaroya. No words can describe the greatness of Professor Benaroya. He is extremely caring for his students as well as for all other students. He always gives time to listen to students (even if they are not his student) whether they have personal or technical issues. His work ethic is amazing. As an advisor he guided me when I needed to be guided but also gave me a chance to learn and figure things out for myself. Professor Benaroya, thank you so much for your guidance and always looked out for me. Also, thank you for your support and providing me with an amazing working environment.

A very big acknowledgement goes to Dr. Jason Florek who has become a great colleague and friend of mine. From the start he has helped me to understand the subject of blast loads and supplied me with many journal articles and books on the subject. I have incorporated some of his work as the foundation of my current work. He is always willing to help answer any questions I have. Jason, we have become great friends over the years and I enjoy each moment we get to hang out together. Thank you so much and I hope our friendship and collaboration will continue to grow.

I acknowledge Dr. Yuriy Gulak for all his assistance with everything from theoretical to computational issues. It is amazing the vast knowledge that Yuriy knows in any subject matter. Yuriy, thank you so much for everything, I can always count on you to have the correct answer. You are truly an amazing person.

I would like to thank my committee members; Professor Haim Baruh, Professor Ellis Dill and Professor Husam Najm. Professor Haim Baruh was the graduate director when I first joined the Mechanical and Aerospace Graduate Department at Rutgers University. He has always been a great professor and friend, and has made my stay here more pleasurable. Professor Baruh, thank you very much for everything you have done for me. Professor Ellis

Dill has helped me a great deal with my computational finite element issues. He was also a great professor in the classes I took with him. Professor Dill, thank you so much for all your help, you are truly a great man. I would like to thank my external committee member, Professor Husam Najm for taking his time and being on my committee. In addition, I had the pleasure of taking a Civil Engineering Structural Steel class under the supervision of Professor Najm. He is a great professor and willing to take his time to helping his students. I enjoyed our discussions on the subject matter immensely. Professor Najm, thank you very much.

A big acknowledgement goes to the U.S. Department of Homeland Security, in particular the Transportation Security Laboratory for all their support. They have provided the experimental results and access to technical material which this work would not have been possible without. I would like to thank Charles Chen, for being the liaison and providing the experimental data and technical direction of this work. A big thanks goes to Mark Nansteel who provided a great deal of technical information on various topics within the blast loading field. I would like to thank Nelson Carey and his former colleague Joseph Gatto for sharing their knowledge on experimental setups. In particular I would like to thank them for the opportunity to witness aircraft blast testing at Aberdeen Proving Grounds. I would like to thank Mark Fry for making sure I got the experimental data I needed and showing interest in my work. The opportunity to do this work would not have been possible if it was not for Christopher Smith. Chris, thank you very much for this opportunity and your technical insight. In addition, I would also like to thank Howard Fleisher for his support.

I thank Rutgers University and in particular, the Department of Mechanical and Aerospace Engineering for the great education they provide and their support. I would like to acknowledge the administrative assistants of our department, in particular Aiesha Long, who has always been caring for the students and capable of accomplishing any task needed. I would like to thank Professor William Bottega. As his predecessor, Professor Baruh, he has been doing a great job as graduate director. In addition, I have been fortunate to have Professor Bottega as my professor in many classes. He is truly a great teacher. Thank you for all the knowledge you have bestowed upon me.

I would also like to thank the Center for Structures in eXtreme Environments for giving me a great place to work and making my stay here at Rutgers pleasurable. A good part of that is due to the contributions of Patricia Mazzucco and of course my advisor Professor Haym Benaroya. I also want to thank the Center for Structures in eXtreme Environments and the Department of Mechanical and Aerospace Engineering for their financial support. In addition, I would like to thank the Center for Mathematics, Science and Computer Education for their financial support while completing this work as well.

I want to thank all my officemates (Yuriy Gulak, Jason Florek, Paola Jaramillo, David Gabbai, Nir Pony, Tushar Saraf, Paul Bonness and Sohrob Mottaghi), my fellow graduate students and the MAE United soccer team for making my time here at Rutgers pleasurable. I would like to thank my former lunch mate, Megan Smith, and my current lunch mate, Kellie Anderson, for wonderful and exciting conversations. I would like to thank Pam Carabetta for being a great friend through my time here at Rutgers. I thank Christel Seitel for taking over the tough job of being the instructor for Senior Design and giving me all the guidance when I took it over. Christel, thank you for being a good friend and providing me hugs when I needed them. I thank Yaru Fan for being such a good friend and making my time here more enjoyable. A huge thanks goes to Paola Jaramillo and Jason Florek. Those two have become amazing friends whom I shared countless hours in the office together. You two have made my earlier years here a pleasure. In addition, In addition, I would like to thank Lucian Iorga, Pedro Romero, Carlos Correa and Maria Velez who also made my earlier years here a pleasure. I would like to thank Wendy Choi for always being supportive of me. I would also like to thank Jaime Zinger for giving me support, kindness and the ability to constantly improve myself.

As I have been lucky to have the best advisor I can ask for, I also have the best parents that I can imagine. I would like to give a big thanks to my parents who have been extremely supportive of me while I have been in school. They have given me encouragement and are always there for me when I need them. Mom and dad, I love you both very much. In addition, I would also like to thank my brother, Oren, for being supportive of me. He has truly been a great brother to me.

Dedication

To my parents, Esther and Ralph Borenstein.

Table of Contents

List of Tables

List of Figures

Chapter 1

Introduction

1.1 Motivation

Due to the rise of terrorism, there is a need for a better understanding of the effects of explosions on structures. For instance, the commercial aviation industry has a great need to understand the effects of an on-board explosion to improve the future design of containers and aircraft. It is also important to locate the areas of the aircraft that are most vulnerable to an explosive load. Knowing these locations and the amount of loading needed to cause critical failures provides a baseline of the amount of explosives which must be detected on passengers and cargo. Buildings, bridges, trains, ships, oil rigs, and a variety of other structures and vehicles are also prime targets for terrorist attacks.

In order to estimate the structural response due to explosions, many experiments are being performed, all of which are very costly and time consuming. As an alternative, there is a large number of finite element codes that can help analyze the response of a structure to a given loading. However, these codes can be rather time consuming to prepare and analyze. Therefore, the availability of an accurate but simplified model of the response of a structure subjected to a variety of blast loads would be of great use.

Aside from a simplified response model, an accurate loading model is needed. Many experiments have been performed to characterize the variety of explosives. During these complex and costly blast experiments, a variety of sensors and devices are used to capture the loading on the structure. The positioning of the sensors and the accuracy of the devices generally leads to uncertainties exclusive of the random characterization associated with the explosives. Terrorist attacks targeting structures or vehicles tend to detonate close to the target, having a small standoff distance. At small standoff distances, there is a greater uncertainty in the various loading parameters due to inconsistent data [3]. In addition, these near field explosions cause complex and nonuniform loading on the target. Therefore, a good nonuniform loading model is necessary for analyzing these types of problems.

1.2 Problem Introduction

The main goal of this study is to create loading and structural models that accurately predict a circular plate's deflection when subjected to a near field explosion for which data exist. Near field explosions occur when an explosive is detonated close enough to the target, where the target is within the high pressure zone before the principal energy of the explosion is lost.

Figure 1.1 shows a schematic of the experimental setup conducted by the Department of Homeland Security [2]. A heat treated 4340 steel circular plate is bolted to a steel bulkhead with 36 bolts resulting in a clamped boundary. With reference to Figure 1.1, the explosive is positioned on the left side of the plate and acts along its axis of symmetry. Two high-speed cameras are positioned on the right side of the plate capture the deformation of the plate [6].

The quantity and type of explosive used are known, as is the distance from the origin of the explosive to the plate. The material properties and geometry of the plate are also known. With this information, the loading and structural response models need to accurately predict the plate deformation. Since the deflections are extremely small and the plate does not yield, only the elastic behavior of the plate needs to be modeled. The plate's maximum deflection, which occurs at the center of the plate, is calculated using the simplified models and then compared with experimental results.

1.3 Dissertation Outline and Contributions

In Chapter 2, a brief review is presented on blast loading and relevant structural response models. Chapter 3 discusses the complex behavior of explosives and develops a simplified nonuniform loading model. This nonuniform loading model is unique as it retains both TNT equivalent factors for pressure and impulse while calculating the various loading parameters. Corrected curve fit equations are generated for certain loading parameters in specific scaled

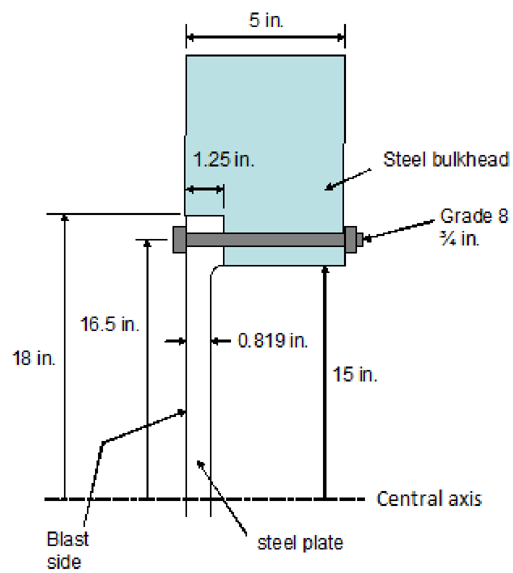

Figure 1.1: Schematic with dimensions of the experimental setup [2].

distance ranges. In addition, a graphical user interface (GUI) program is developed (and given to our research sponsors) that produces the spatial and time dependant nonuniform loading due to an explosion. This program contains many features and options that give the user flexibility to generate the proper type of loading which accurately models their problem.

Chapter 4 presents the derivation of the analytical model that is based on the von Kármán model for thin, circular plates. The von Kármán model is modified by utilizing a new assumed shape which is derived in this study. This new assumed shape has one physical parameter that describes the boundary condition whereas the original assumed shape which uses two coefficients with no physical meaning. Since the boundary condition is characterized with just one parameter, this new assumed shape also allows for a sensitivity analysis to be performed on the boundary condition. The solution of the von Kármán model using this new assumed shape is also presented. The Runge-Kutta method is implemented to numerical calculate the time dependent function of the von Kármán model.

Chapter 5 presents the finite element models that are used for verification of the analytical model. Two different geometries are used, a simplified thin, circular plate and one representing the actual plate configuration. These finite element models were created in a way to be able to use the spatial and time dependant surface loading generated from the nonuniform loading model of Chapter 3. They also include detailed properties, such as material damping, calculated using the experimental data provided by our sponsors.

Chapter 6 presents the results and discusses them. The three models (analytical model and two finite element models) are compared with each other as well as with the experimental results for four different explosions. The deformation contours are presented, as well as the comparison of the estimated deflections at the center of the plate. The maximum center plate deflection is analyzed and compared. Various results are shown that verify the proposed loading model. Overall, the loading and structural models allow us to reasonably match experimental results for deflection. It was also proven that the parameters describing the time-history loading are not accurate at small scaled distances.

Chapter 7 presents uncertainty analyses associated with the analytical model. This includes a measure of the sensitivity of the maximum plate deflection to various loading and structural parameters. In addition, a sensitivity analysis is presented of the maximum plate deflection to loading parameters' uncertainties.

Chapter 8 provides a summary of key results and future work. Appendix A includes certain equations and coefficient values which were too long to be incorporated into the text.

Chapter 2

Literature Review on Blast Loading and Plate Deformation

Understanding the dynamics of blast loading and developing simplified loading models are topics of research that have been pursued in academia and government. A good amount of the government work is classified; however, there is some literature available to the general public. Following is an overview of some of the books and papers related to blast load modeling.

There have been a few books dedicated to explosive loading. Kinney and Graham produced a very comprehensive book, "Explosive Shocks in Air" [7], which explains many different aspects and characteristics of explosive loads. Another extensive book on blast loading is "Explosions in Air" [4] by Baker. Aside from an overview of explosive loading this book includes a compilation of experimental equipment and data, as well as some computational methods. A much cited book that deals with explosive loads is "Explosion Hazards and Evaluation" [8] by Baker et al. This book has an extensive compilation of various experimental works. A slightly more current book with a good overview of explosive loading is "Blast and Ballistic Loading of Structures" [9] by Smith and Hetherington. "The Dynamics of Explosion and Its Use" [10] by Henrych is another very comprehensive book on this subject. "Dynamic Loading and Design of Structures" [11] edited by A. J. Happos provides sections on various loadings including explosions and impacts.

In addition to books, there have been a number of review papers. Florek and Benaroya [12] provide an extensive review on pulse-loading effects on structures. Their review studies various pulse shapes and their effects on the deflection of structures. In addition, they summarize efforts to reduce or eliminate these pulse shape effects, which can be done for many rigid-plastic geometries with a uniform load. A detailed description is provided of research on pressure-impulse isodamage curves along with some background on the sensitivity of various loading models.

Remennikov [13] gives a brief overview of current available analytical and numerical techniques to predict loads on structures subjected to an explosion. He discusses the widely used US Department of the Army technical manual TM 5-1300 [5] and TM 5-855-1 [14]. Ngo et al. [15] also discuss these technical manuals, as well as others, and provide an extensive overview of blast effects on structures. Rajendran and Lee [16] provide a review on plates subjected to blast loading. Their review discusses explosions in air and underwater.

Bashara [17] provides an extensive review of the analysis of unconfined blast loading from different sources for aboveground rigid structures. Bashara discusses the use of TNT equivalency and blast scaling laws, as well as the difference of overpressure, reflective pressure and dynamic pressure. From reviewing the available unclassified literature, Bashara concluded that “precise loading information is hard to obtain and may be not justified because of the many uncertainties involved in the interaction process between the blast wave and the structure and the ideal gas assumption in the derivation of relevant relations...” In addition, Bashara adds that the way a blast load affects the response of a structure does not only depend upon the magnitude of the load, but also on its duration, rise time and general shape. The implication is that a good blast loading model is important.

Chock and Kapania [18] provide a review of blast scaling, particularly the Hopkinson-Cranz and the Sachs blast scaling. They then compare two methods for calculating explosive blasts in air. One method is from Baker [4], which uses Sachs scaling and the other method is from Kingery and Bulmash [19], which uses Hopkinson-Cranz scaling. They concluded that the reflected peak pressures are of a similar order of magnitude but there is a difference in the specific impulses delivered to the target. For the case given in Chock and Kapania, Baker’s method has a much lower impulse and an earlier arrival time than Kingery and Bulmash’s method. Chock and Kapania mention that this could be attributed to the difference in duration time, as well as a change in the way that the decay values are determined. They were unable to determine which of the two methods are more precise because both methods are based on experimental data, with little or no repeated tests.

Esparza [20] performed experiments on TNT and other high explosives at small scaled distances. He states that using a single equivalent weight ratio may not be appropriate, especially at small scaled distances because there is insufficient experimental verification. In regards to TNT equivalency, he mentions that an equivalence system with only one blast parameter may not be accurate because TNT equivalence can be significantly different depending on the scaled distance of the explosive, even with the same type of explosive. Esparza did a study and comparison to published data [19] on the peak overpressure, arrival time, impulse and positive duration of the blast loads in his experiments. He noticed that the TNT equivalency for some of the parameters can be significantly different than one based on heat of detonation. In addition, for small scaled distances, the impulse and positive duration parameters are not as well defined as the pressure and arrival time parameters.

Hargather and Settles [21] discussed optical shadowgraphy and high-speed digital imaging techniques to measure the shock wave caused by an explosion. Using their technique, they were able to calculate the TNT equivalence of the explosives used. They concluded that a single TNT equivalence value is inadequate to fully describe an explosive yield, but rather TNT equivalence factor and overpressure duration should be presented as functions of scaled distance.

Gatto and Krznaric [22] performed experiments on explosive loads in aircraft luggage containers. They measured the pressure profiles on the container panels due to explosions with different amounts of luggage inside. They noticed that additional luggage reduces the pressure on the container significantly. In addition, the location of the bag with the explosives has a significant effect on the loading the container experiences.

Veldman et al. [23, 24] performed experiments on pre-pressurized plates under blast loading. The plates in Reference [24] included rivet-attached stiffeners in order to model the fuselage skin of a commercial aircraft. They used high-speed cameras to capture the deformation and failures of plates. Their results show that for weak blast loads the pre-pressurization is not a large factor, however, for stronger blast loads the pre-pressurization causes a significant increase in panel damage.

Simmons and Schleyer [25] did experimental work and performed finite element analysis of the response and failure modes of stiffened, aluminum alloy panels with conventional riveting and laser welding. They used a pressure chamber that theoretically gives a triangular pressure pulse on the test structure. They concluded that riveted joints have greater energy absorbing capacity than laser-welded joints. In addition, they noted that the joints' energy absorption is sensitive to the load rate.

There have been studies [26–28] on saturated impulse phenomena for pulse-loaded perfectly plastic beams and elastic-plastic plates. These studies show that there is a limit on how much impulse applied to a structure will affect its deformation. This is because the membrane forces, which are induced by large deflections, give the plates a greater capacity to withstand loads. The saturation duration is the time during which the loading affects the deformation of the structure. Any additional load after this saturation duration time will have no further contribution on the structural deformation. Zhu and Yu [27] point out that the saturation duration is a function of plate geometry and material properties, and not of the pressure loading.

Brode performed numerical analyses [29] of spherical blast waves. Brode also did a computational analysis [30] of a blast wave from a spherical charge of TNT. In his analyses Brode was able to observe the rarefaction waves and their interaction with multiple shocks.

Gantes and Pnevmatikos [31] proposed a response spectra based on a blast pressure profile with an exponential distribution and then compare it to one with a triangular distribution. In their work, they used a technique recommended by the US Department of the Army TM 5-1300 [5], which is based upon substituting the structural element by a stiffness equivalent, single degree-of-freedom system, and using elastic-plastic response spectra to predict the maximum response of the system. They found that a triangular distribution with time can sometimes be slightly unconservative, particularly for flexible structural systems. In addition, it can be significantly overconservative for stiffer structures. They stated that since exponential loading decreases faster than a triangular one, the differences between the two are influenced more in elastic-plastic situations than in purely elastic ones. In addition, ranges of certain parameters are given for when differences in blast loading profiles play significant roles in the response. Referring to Watson [32], the response depends on the synchronization with the rebound of the structure, which means that a good knowledge of blast load time and space variation are critical to obtain the correct response. In addition, Watson writes that the influence of damping on these systems can be neglected because the peak response of the system occurs within the first few cycles. This allows for a much simpler response equation.

Neuberger et al. [33] performed experimental and numerical simulations on circular plates to determine if scaling laws are valid for large and close-range spherical explosions in air. Their results show the validity of the scaling laws.

Bogosian et al. [34] used experimental data to compare a variety of simplified models, including BlastX, ConWep and SHOCK, and to measure the inherent uncertainty in these blast model codes. The data they analyze is restricted to a scaled range of 3 to 100 ft/lb$^{(1/3)}$. Although their final test database comprised of 303 individual gage records, they noted that not all were of sufficient duration and/or quality. Some have bad peak pressure readings and therefore could not produce reliable impulses. In addition, the test data comprised of a wide range of configurations from cylindrical to spherical to hemispherical charges. Different types of explosives were also used, including TNT, C-4 and ANFO, which were converted into their TNT equivalent load before computing the scaling factors. This shows how difficult it is to obtain a complete and accurate set of experimental work to analyze and understand the entire spectrum of blast loadings. However, Bogosian et al. were able to show that of the tools they analyzed, ConWep best represented the test data in an overall sense. They also show that BlastX provides values that are close to the data set, but SHOCK significantly underpredicts reflected positive pressure and overpredicts reflected positive impulse. By calculating the standard deviations of the test data, they noticed that their two-sigma values range from 1/3 to 2/3 in magnitude, which indicates a very wide range of uncertainty.

ABS Consulting Ltd prepared a research report [35] that uses a tool they developed, call BlastSTAR, to perform multiple analysis of simple structures that are subjected to blast loadings with different geometries, durations and peak pressures. BlastSTAR finds the force-displacement and equivalent mass characteristics of an equivalent simplified system by utilizing the results of a static FE analysis. Their results analyze the maximum displacements obtained from a variety of loading scenarios acting on various structures.

Nansteel and Chen [6] discuss a procedure using high-speed cameras to capture plate deflections and strains. Their procedure does not incorporate any devices which are in contact to the plate. The high-speed cameras are coupled with digital image correlation techniques and are capable of capturing the full transient motion of the entire plate.

Hargather and Settles [36] performed experiments utilizing high-speed cameras to measure the deformation of aluminum plates subjected to explosions. They concluded that the maximum dynamic plate deformation is a straightforward function of the applied explosive impulse.

Ballantyne et al. [37] analytically analyzed the effects of a blast wave hitting a structure with a finite width. Due to the finite width a phenomenon called clearing is created. Clearing occurs when the reflected wave reaches the section extremities and causes vortices to shed and a low pressure wave to generate. This low pressure wave propagates inwards towards the expanding wave which causes the expanding wave to decay quicker. This phenomenon reduces the impulse on the structure however does not affect the peak reflected pressure.

Bauer [38] and Singh and Singh [39] provide mathematical models to predict the deflection of an elastic plate subjected to an exponentially decaying pulse, representative of blast loads.

Trying to obtain a simplified, yet accurate model for blast loadings is a topic still being examined. These publications, which are mainly focused on loading models, show there is a great amount of uncertainty involved when dealing with blast load modeling. In addition, many of the publications show that the response of a structure is very sensitive to the loading model.

Chapter 3

Blast Loading Model

The first step in modeling the plate's response to near field explosions is to develop a blast loading model. In this chapter, a brief explanation of the complex phenomenon of explosive blasts is presented. A simplified loading model for uniform loading is then discussed. This simplified uniform loading model is then converted to a nonuniform loading model, suitable for near field explosions. The model is unique as it retains both TNT equivalence factors for pressure and impulse while calculating the various loading parameters. It also utilizes corrected curve fit equations which are used to obtain certain loading parameters in specific scaled distance ranges. The nonuniform loading model is used to formulate the computational loading model, including a graphical user interface program.

3.1 Explosions

Generally speaking, an explosion is a phenomenon that produces a rapid release of energy. This release of energy is so sudden that there is a local accumulation of energy at the site of the explosion. This accumulated energy gets dissipated through blast waves, propulsion of fragments, and/or thermal radiation. Although the release of energy may cause pressure or shock waves in air (airblast), groundshock, cratering, fragmentation, thermal radiation, or any of these combinations, here will only be dealing with airblasts. Depending on the reaction speed of the released energy, explosions are classified as a detonation or deflagration. If the reaction speed is less than the speed of sound, the explosion causes pressure waves and is classified as a deflagration. Explosions that are thermal in nature undergo a relatively slow process and tend to cause deflagration. Since these reaction speeds are slower, external conditions such as ambient pressure play a bigger role in the characteristics of the explosive response. On the other hand, if the explosion's reaction speed is equal or greater than the speed of sound, it causes shock waves and is classified as a detonation. Detonations are primarily mechanical in nature, meaning that the released energy is transmitted mechanically through neighboring material. This mechanical transmission of energy is relatively independent of external conditions and therefore ambient pressure does not play a significant role in the characteristics of the explosive response. High explosives, such as TNT (symmetrical 2, 4, 6-trinitrotoluene) and C-4 (Composition 4), cause detonations. Implosions are the same as explosions except the energy released is initially directed inwards. In this work, only detonations are considered.

3.2 Overview

Figure 3.1 shows the pressure-time history of a typical blast wave at a specific point some finite distance away. Initially, there is a period of time from detonation to when the airblast reaches the target, called the arrival time, t_a. At that point in time, the detonated airblast waves tend to have an almost instantaneous rise from ambient pressure, P_0, to their peak overpressure, $P(t) = P_{max}$, and then decay exponentially. The pressure $P(t)$ decays back to the ambient pressure in the positive phase duration time, T_s. The area under the pressure-time curve during this positive pressure phase is called the specific impulse, i_x, given by

$$i_x = \int_{t_a}^{t_a+T_s} \left(P(t) - P_0\right) dt, \tag{3.1}$$

where i_x can represent i_r or i_s for specific side-on impulse or reflective impulse, respectively. Note that this impulse has units of pressure multiplied by time and not the typical force multiplied by time.

After the positive pressure phase, the pressure continues to decrease (underpressure) below the ambient pressure and then eventually rises back to the ambient pressure. This time period is called the negative pressure phase. It is usually ignored during structural analysis because it is much less significant than the positive pressure phase. There is also considerable difficulty in accurately measuring or computing its characteristics [4]. In addition, the underpressure reduces the amount of transverse deflection. However, in certain

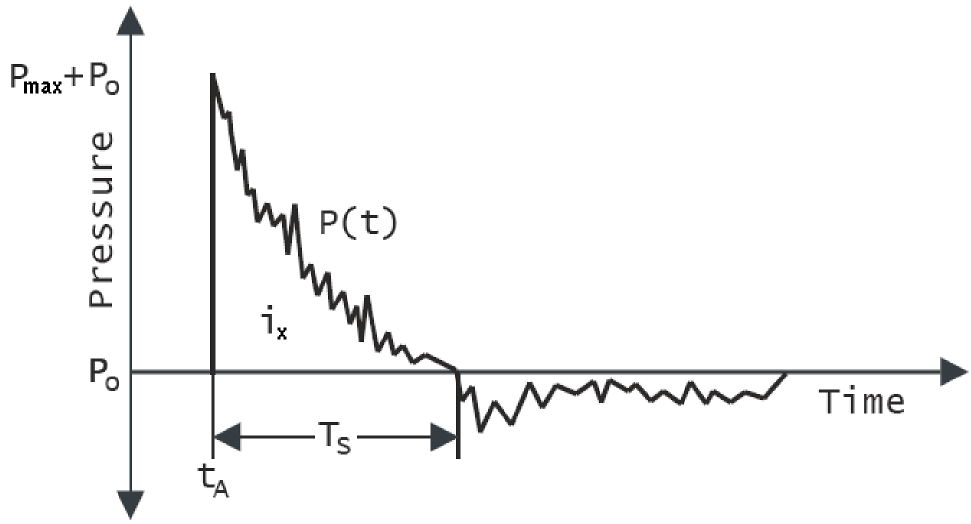

Figure 3.1: Typical blast wave pressure-time history. Modified from [3].

situations the negative phase can become significant, as mentioned in Baker et al. [8]. In this work we ignore the negative pressure phase.

3.3 Uniform Loading Model

For a blast (detonation) load, chemical investigation and experimental data [4,7,8,20,22] show that a good representative simplified model is an exponential time history. One of the most frequently used blast models is an exponential decay model with an instantaneous peak pressure governed by the *modified Friedlander equation*,

$$P(t) = \begin{cases} P_0, & t < t_a \\ P_0 + P_{max}\left(1 - \frac{t-t_a}{T_s}\right)\exp\left[-\alpha\left(\frac{t-t_a}{T_s}\right)\right], & t_a \le t \le t_a + T_s \\ P_0, & t_a + T_s \le t, \end{cases} \tag{3.2}$$

where α is the exponential decay constant. Figure 3.2 is a graphical representation of this simplified loading model. This modified Friedlander equation neglects any negative overpressure phase of a blast load.

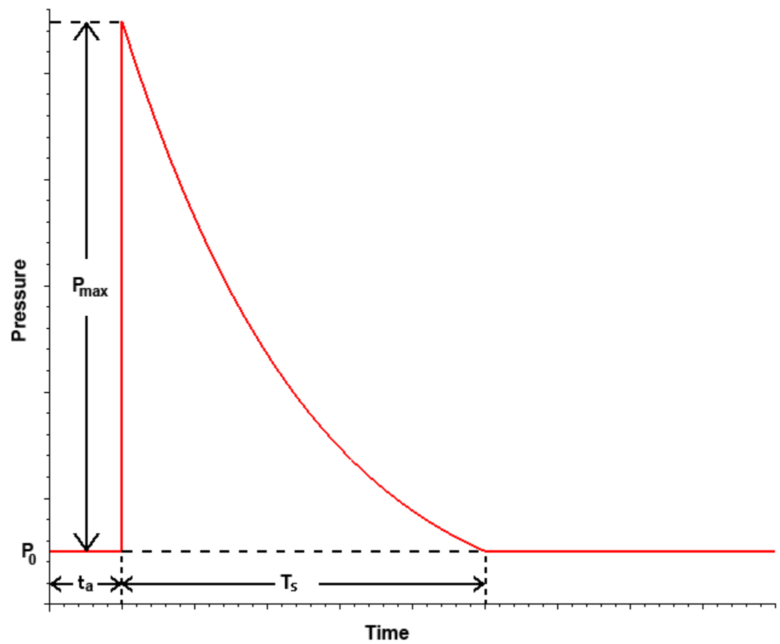

Figure 3.2: Simplified blast loading model representative of the modified Friedlander equation, where the negative overpressure phase after time T_s has been truncated.

3.4 Side-on vs. Reflected Pressure

The maximum overpressure, P_{max}, can represent either the peak side-on overpressure, P_s, or the peak reflected overpressure, P_r. Side-on pressure occurs in free-air and does not account for any of the reflected pressure waves from a surface. When a pressure wave hits a surface, its particles stop abruptly and get reflected by the surface. These reflected particles give the effect of a new shock wave propagating back towards the charge at the same relative velocity as the incident wave. This reflected shock wave moves along the surface adding to the incident shock waves causing an increase in total pressure on the surface.

3.5 Blast Scaling Laws

Blast scaling laws are useful to interpolate a large range of explosive blast loading profiles using a limited number of tests. For explosive analyses which are not at high altitudes, the most common scaling law is the Hopkinson-Cranz [9]. This scaling law is also called cube-root scaling. It states that two explosions of similar geometry, explosive type and

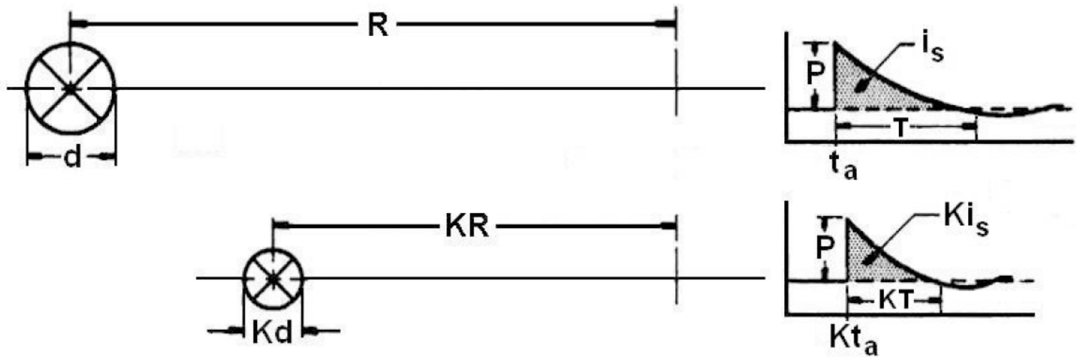

Figure 3.3: Schematic representation of Hopkinson-Cranz blast wave scaling [4].

atmosphere produce self-similar loading profiles if they have the same scaled distance Z,

$$Z = \frac{R}{W^{1/3}}, \tag{3.3}$$

where R is the standoff distance between the spherical charge center and the target in feet, and W is the charge weight (potential blast energy), which is expressed in pound-mass of equivalent TNT. Although W is referred as charge weight in literature dealing with English units, in actuality W is the charge mass with units of pound-mass. However, to be consistent with the convention of previous literature, W will continue to be referred to as charge weight. Figure 3.3 shows a schematic representation of this scaling law. The figure shows that a spherical explosive with diameter d at a distance R away from the target produces the same peak overpressure, as the same explosive with diameter Kd at a distance KR from the target. In addition, the duration time, T_s, and impulse, i_s, scale by the factor K. The Hopkinson-Cranz scaling law assumes gravity and viscosity effects are negligible and for a given type of chemical explosive, the energy is proportional to the total weight. The scaling law relationships have been experimentally proven for a large range of explosive weights [40].

3.6 TNT Equivalence

As mentioned above, charge weight in Hopkinson-Cranz scaling law is typically expressed in TNT-equivalent weight. This is because, as we will see in the next section, all the loading parameters have been collected and tabulated using the weight of TNT. For specimens of known density and crystalline nature, the explosive effects of TNT are repeatable. In order to utilize these collected data for an explosive other than TNT, one must first convert the weight of the explosive used to its TNT equivalent weight. This is done by multiplying the weight of the explosive used by its TNT equivalent weight factor. These factors can be calculated by knowing the heat of detonation of the explosive in question or looked up in tables with values collected via experiments for a variety of different explosives. It is noted in Reference [1] that the table values obtained via experiments are more accurate than the values calculated via the heat of detonation of the explosive. However, the tables do not contain all the different explosives.

Some sources [1, 9, 14] tabulate two different TNT equivalence factors, one for pressure and one for impulse, for each type of explosive. Smith and Hetherington [9] mention that with the two conversion factors, the ability to choose which to use depends on whether the peak overpressure or the impulse delivered is to be matched.

3.7 Obtaining Blast Parameters

The positive phase air blast loading parameters, P_r, P_s, T_s, t_a, i_r and i_s, can be obtained from collected experimental data [1, 5, 8, 14, 19, 41]. Kingery and Bulmash [19] curve-fitted the loading parameter values for a variety of experimental data. These values are widely used, including in the government computer program for weapon effects, ConWep [42]. Figure 3.4 shows these positive phase air blast loading parameter curve-fits for a spherical charge of TNT detonated in free-air at sea level. The parameter values are a function of the Hopkinson-Cranz scaled distance, Z. In addition, note that certain parameters are scaled by the cube-root of the charge's weight. Also, great care must be taken regarding the units in the figures. Some sources represent the scaled distance in units of ft/lb$^{1/3}$ and others in m/kg$^{1/3}$, with the parameters in English or metric units.

The dashed lines in Figure 3.4 represent an increase of TNT equivalent weight of 20% for Z values less than 1 ft/1b$^{1/3}$ which Reference [1] states should be used to compensate for unknown factors when designing structures.

For a certain scaled distance, all the loading parameters can be obtained from this graph except for the decay constant, α. Therefore, α needs to be calculated using the given value for reflective impulse, i_r, or side-on impulse, i_s. Assuming we want the decay constant for the reflective loading pressure, we know that

$$i_r = \int_{t_a}^{t_a+T_s} (P(t) - P_0)\, dt, \tag{3.4}$$

where $P(t)$ is the reflective pressure given by Equation 3.2 with $P_{max} = P_r$, one can find that

$$\frac{P_r T_s e^{-\alpha}(\alpha e^{\alpha} - e^{\alpha} + 1)}{\alpha^2} - i_r = 0. \tag{3.5}$$

Substituting the values of P_r, T_s and i_r into Equation 3.5, one can find α numerically.

3.7.1 ConWep

ConWep [42] can be used to generate the values of various air blast loads. This computer code uses values gathered through experiments given in TM 5-855-1 [14], which makes use of Kingery and Bulmash [19]. According to Esparza [20], Kingery and Bulmash supply polynomial curve fits from values found in Goodman [43], Kingery [44], Reisler et al. [45], Swisdak [46] and Davis et al. [47]. ConWep allows users to input the amount and type of explosive and its standoff distance. It will then generate the various loading parameters, except for the decay constant for reflective pressure. Since ConWep digitally contains the collected data, identical to the information contained in Figure 3.4, it is very convenient to use for obtaining the air blast loading parameters. In addition, it helps prevent potential errors or inaccuracies from reading the log plots.

One difference, ConWep does not use the dashed line data in Figure 3.4. In addition, for TNT equivalences, ConWep averages the pressure and impulse TNT equivalence weight factors [1, 42]. For instance, the TNT pressure and impulse equivalence weight factors for C-4 are 1.19 and 1.37, respectively. In order to determine the loading parameters with a C-4 type explosive, ConWep would utilize the average TNT equivalence weight factor of 1.28 to adjust the weight of the explosive used.

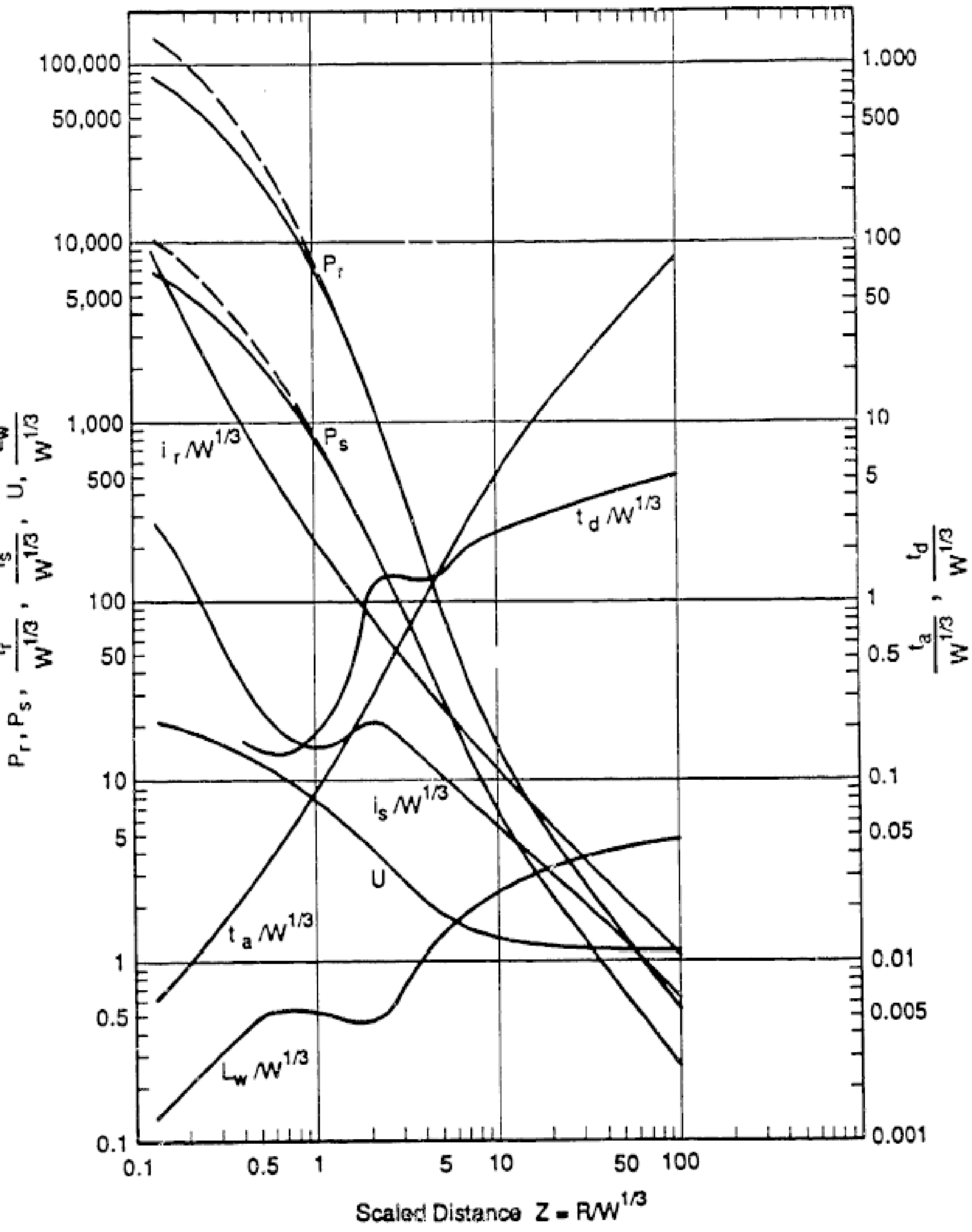

Figure 3.4: Positive phase shock wave loading parameters for a spherical TNT explosion in free air at sea level (English Units) [1, 5]. Scaled distance, Z (ft/lb$^{1/3}$); peak normally reflective overpressure, P_r (psi); peak side-on overpressure, P_s (psi); normally reflected specific impulse, i_r (psi-ms); side-on specific impulse, i_s (psi-ms); shock arrival time, t_a (ms); positive phase duration, t_d (ms); shock front velocity, U (ft/ms); wave length of positive phase, L_w (ft); TNT equivalent weight, W (lb). Note that the positive phase duration, T_s, is labeled as t_d in this figure.

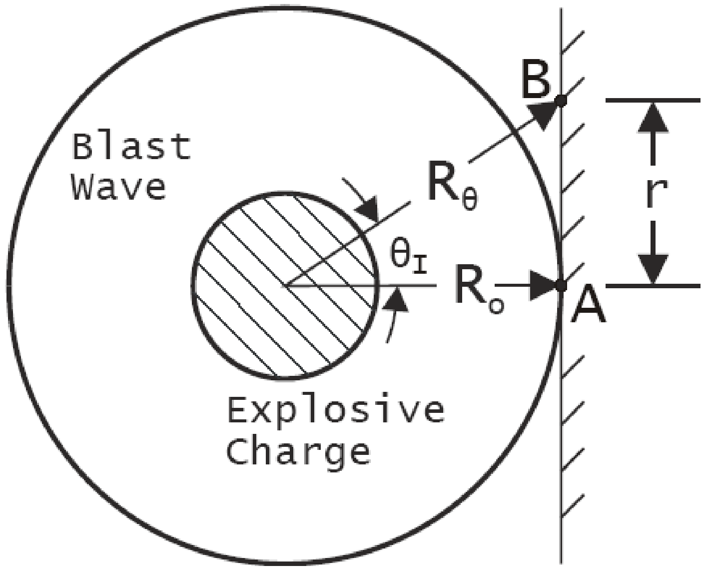

Figure 3.5: Schematic of an ideal spherical blast wave impacting a flat surface [3].

3.8 Nonuniform Loading

To this point, we have discussed how to obtain the pressure loading at a specific point away from the explosive, which can be translated to a uniform loading on a plate. However, when the explosive has a small standoff distance the spherical air blast will result in a nonuniform loading on the plate. Figure 3.5, which is a schematic of an ideal blast wave impacting a flat surface, shows that point A is closer to the center of the charge than point B. This difference in charge distance for various points on the plate becomes important for near-field explosions. The calculation of the loading at point A is the same as the uniform loading method mentioned above. However, for point B the standoff distance is increased, thus increasing the scaled distance, Z. The distance from the center of the charge to point B, labeled as R_θ in Figure 3.5, is called the slant distance, which must be taken into consideration.

Depending on the angle of incidence, θ_I, the reflective pressure will differ. The normally reflective pressure, when $\theta_I = 0°$, yields the greatest reflective pressure on the surface. As the angle of incidence increases the reflective pressure tends to decrease. This relationship is given by [3, 33]

$$P_{net}(Z, \theta_I) = P_r(Z) \cdot \cos^2 \theta_I + P_s(Z) \cdot \left(1 + \cos^2 \theta_I - 2 \cos \theta_I\right), \tag{3.6}$$

where P_{net} is the net maximum overpressure at a specific location on the plate. Similarly, the net specific impulse can be calculated by [3, 42]

$$i_{net}(Z, \theta_I) = i_r(Z) \cdot \cos^2 \theta_I + i_s(Z) \cdot \left(1 + \cos^2 \theta_I - 2 \cos \theta_I\right). \tag{3.7}$$

In these equations, both Z and θ_I are functions of location on the plate. These functions are valid for free air detonation of a spherical charge and ground surface detonation of a hemispherical charge. These functions also ignore any Mach stem effects, a coalescence of the reflected blast wave with a secondary incident wave which occur at an angle of incidence of 40° to 50°.

For this study, we consider a circular plate. Since the circular plate is axisymmetric and the spherical explosive is located on this axis, the problem becomes spatially one dimensional. Therefore, both Z and θ_I become functions of r, the distance from the center of the circular plate. Since we assume the explosive charge is located on the normal going through the center of the plate, as we move further from the center of the plate, Z and θ_I increase. For such axisymmetric systems Equations 3.6 and 3.7 can be rewritten as

$$P_{net}(r) = P_r(r) \cdot \cos^2 \theta_I(r) + P_s(r) \cdot \left(1 + \cos^2 \theta_I(r) - 2 \cos \theta_I(r)\right), \tag{3.8}$$

and

$$i_{net}(r) = i_r(r) \cdot \cos^2 \theta_I(r) + i_s(r) \cdot \left(1 + \cos^2 \theta_I(r) - 2 \cos \theta_I(r)\right). \tag{3.9}$$

3.8.1 Procedure for Calculating Nonuniform Loading

Florek [3] outlined a thorough procedure to calculate nonuniform pressure distribution due to an airblast. These procedures were based on Reference [5]. The following procedure utilized in this work are based on these procedures with a few modifications. One key modification in this procedure is to utilize both pressure and impulse TNT equivalences weight factors. The pressure TNT equivalence weight factor is used to calculate the peak side-on and reflective pressures, while the impulse TNT equivalence weight factor is used to calculate the positive phase duration time, arrival time, side-on and reflective impulses. The decay constant uses both since it is calculated with the positive phase duration, side-on and reflective impulses, as well as the side-on and reflective pressures.

Below are the general steps used to produce the nonuniform blast loading on the axisymmetric circular plate. This procedure can be applied to non-axisymmetric plates by replacing r with the coordinate system parameters of the plate, such as x and y for a typical rectangular plate in Cartesian coordinates.

1. Convert the weight of the explosive used to its TNT equivalence for pressure, W_p, and impulse, W_i. This is done by multiplying the weight of the explosive by its TNT equivalence weight factor for pressure and impulse.

2. For each point on the target surface, determine the standoff (slant) distance, R_θ, and the angle of incidence, θ_I, from the center of the charge.

3. Then for each point on the target, calculate the Z value with the equivalent TNT weight for pressure, Z_p, and the equivalent TNT weight for impulse, Z_i. The equations are

$$Z_p(r) = \frac{R_\theta(r)}{W_p^{1/3}}$$

and

$$Z_i(r) = \frac{R_\theta(r)}{W_i^{1/3}}.$$

4. Using $Z_p(r)$ and the data from Figure 3.4, find the values for P_s and P_r at each point on the target.

5. Using $Z_i(r)$ and the data from Figure 3.4, find the values for T_s, t_a, i_r and i_s, at each point on the target.

6. Using Equations 3.8 and 3.9 calculate the net pressure, P_{net}, and net impulse, i_{net}, at each point on the target.

7. Using Equation 3.5, with $P_r = P_{net}$ and $i_r = i_{net}$, numerically solve for the decay constant, α, for each point on the target.

8. Using the values $T_s(r)$ and $t_a(r)$ (obtained from Step 4), $P_{net}(r)$ and $i_{net}(r)$ (obtained from Step 5), and $\alpha(r)$ (obtained from Step 6), the nonuniform loading can be calculated using the following modified Friedlander equation that is a function of time and location on

the plate:

$$P(r,t) = \begin{cases} P_0, & t < t_a(r) \\ P_0 + P_{net}(r)\left(1 - \frac{t-t_a(r)}{T_s(r)}\right)\exp\left[-\alpha(r)\left(\frac{t-t_a(r)}{T_s(r)}\right)\right], & t_a(r) \le t \le t_a(r) + T_s(r) \\ P_0, & t_a(r) + T_s(r) \le t. \end{cases}$$

3.9 Computational Loading Model

3.9.1 Parameter Value Curve Fits

In order to automate the loading procedure to allow it to be implemented in a computer program, the blast loading parameter data from Figure 3.4 needs to be digitized for access by the computational code. Reference [1] provides curve fit equations for these parameters at various scaled distance ranges. For verification, we used these curve fit equations for TNT spherical free-air explosions and checked them against the data from Figure 3.4 for various values. The reflected pressure curve fit for the scaled range of Z = 0.134 to 100 ft/1b$^{1/3}$ did not match. In addition, the positive phase duration curve fit equation for the scaled range of Z = 5.75 to 100 ft/1b$^{1/3}$ did not match. Due to this, it was necessary to generate accurate curve fits for these loading parameters within those scaled ranges.

To do this more accurately, ConWep was used to evaluate a spherical free-air burst for 1 lb of TNT at a standoff distance of 1 ft. Using the plot feature in ConWep, the values for pressure vs. range were plotted. Using this digitized plot, the various data points along the reflected pressure curve at various ranges were accurately determined. A variety of those data points were taken and used in Maple to find a polynomial curve fit for each range. The same procedure was used for the positive phase duration parameter, except the plot feature in ConWep was used to plot the duration time vs. range as opposed to the pressure vs. range.

In order to get a more accurate curve fit for the reflective pressure in the scaled range of Z = 0.134 to 100 ft/1b$^{1/3}$, the range was split into three smaller scaled ranges; Z = 0.233 to 2.131 ft/1b$^{1/3}$, Z = 2.131 to 5.327 ft/1b$^{1/3}$and Z = 5.327 to 12.317 ft/1b$^{1/3}$. In each of these ranges, Maple was able to obtain a very good curve fit with a polynomial interpolation. 8th, 12th and 2nd degree polynomials were generated for the three scaled ranges, respectively.

Since the applications for this work are near-field explosions with scaled distance ranges of less than 10 ft/1b$^{1/3}$, there was no need to curve fit the rest of the range for the reflective pressure or the positive phase duration. For the positive phase duration time, only one scaled range was calculated. This range is $Z = 5.75$ to 12.3 ft/1b$^{1/3}$. However, in order to obtain a better fit to the data points, a Thiele interpolation was used. The Thiele interpolation returns a continued fraction which fits the data points. In certain situations the Thiele interpolation can produce a denominator of zero, however for our data it was able to produce a very good and valid curve fit.

These new calculated corrected curve fit equations along with the correct curve fit equations given in Reference [1] allow for the computational program to obtain any of the loading parameter values for a specific scaled distance in the range $Z = 0.37$ to 12.3 ft/1b$^{1/3}$.

3.9.2 Chebfun

The nonuniform loading program utilizes a MATLAB® toolbox called chebfun [48]. This toolbox is used to determine the decay constant from Equation 3.5 by finding its roots. It utilizes Chebyshev polynomial expansions to solve for the roots faster than the built in methods of MATLAB.

3.9.3 Graphical User Interface Nonuniform Loading Program

Figure 3.6 shows the graphical user interface (GUI) version of the nonuniform loading program. The first group of options is for *Units*. The user can decide what units (English or SI) are used for the input and results. For the English option, the units are lb, in and psi. For the SI option, the units are kg, m and Pa. For both the English and SI options, the time is in ms. Note that internally, the program does all the calculations in English units.

The next group of options below the *Units* options is the *Basic* Section. In this section the user inputs general information particular to their problem. This includes properties of the explosive, for example, the *Mass of the Explosive* and the *Standoff Distance* to the target. In addition, the user must specify the radius of the target plate. Since this program calculates the nonuniform loading at various points on the plate, the number of locations needs to be specified as well. This is done in the *Radial Divisions* field, where the default

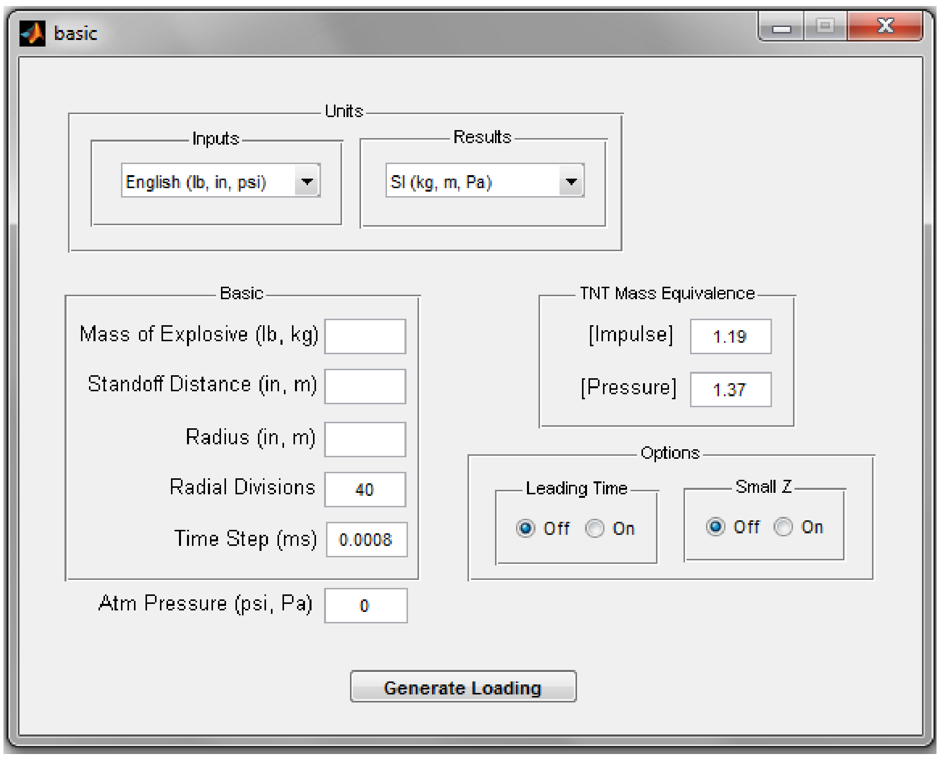

Figure 3.6: Snapshot of the Loading Model GUI Interface.

value is arbitrarily set to 40. The program will evenly divide the target plate into that number of sections and calculate the loading at the nodes of each section. For example, with the default value of 40, the program will output the load on the plate in 41 locations which are evenly distributed. Finally in this group, the *Time Step* needs to be given. The time step value tells the program how much time should be between each calculated value. The default is set to 0.0008 ms. This value is sufficiently small to capture the blast loading values accurately.

The *Atm Pressure* field allows the user to add an atmospheric pressure to the final pressure values. If the user desires only the overpressure of the explosive loading, as in most cases, the value should be set to the default value of 0.

The *TNT Mass Equivalence* group is for specifying the impulse and pressure TNT equivalence weight factors of the type of explosive used. The default values are set for C-4 explosives, which is the type used in this work. The default value for the TNT weight equivalence factors of C-4 is 1.19 and 1.37, for impulse and pressure, respectively.

The *Small Z* option refers to the dashed lines of Figure 3.4. If this option is turned on, the parameter values for side-on and reflective pressure will be taken using the dashed lines as opposed to the sold lines. This is done by use of the pressure factors given in Reference [1], and reproduced here in Table 3.1, for various scaled ranges. A linear interpolation is used for values within each of these factors' ranges. The computer program uses curve fit equations to calculate the side-on and reflective pressure of the solid lines in Figure 3.4. If the Small Z option is turned on, it will multiply the pressure values by the side-on and normally reflected pressure factors to obtain the value of the dashed line.

The *Leading Time* option allows the user to retain or remove all the loading pressure values that occur prior to the first airblast wave hitting the target. When this feature is turned on, the results retain all the leading atmospheric pressure values before the first pressure wave hits the target, which would be the shortest arrival time. This may be useful to keep track of the pressure values in real-time, meaning that time starts from the point of detonation. When this feature is turned off, all the leading atmospheric pressure values get dropped, except for the first row at time 0 seconds. This is beneficial for use in numerical simulations where one wants the loading to be applied right away to save computational

Scaled Distance (ft/1b$^{1/3}$)	Side-on Pressure Factor	Normally Reflected Pressure Factor
0.134	1.40	1.50
0.2	1.34	1.46
0.3	1.25	1.41
0.4	1.15	1.35
0.5	1.13	1.29
0.6	1.10	1.23
0.7	1.08	1.17
0.8	1.05	1.12
0.9	1.02	1.06
1.0	1.00	1.00

Table 3.1: Side-on and normally reflected pressure factors for small scaled distances [1].

time. Note that with both options, the final column of pressures are all set to atmospheric pressure. This guarantees that the loading is no longer applied after the duration time has passed.

Once all the inputs are properly entered, the user presses the Generate Loading button and the program calculates the nonuniform loading. The program outputs a matrix of pressure values (psi or Pa) with the time increasing from left to right and distance from the center of the target increasing from top to bottom. Figure 3.7 shows a partial snap shot of the output. The first column gives values of the distance from the center of the circular plate (in or m). The first row gives values of the time in seconds. The reason the time for the output is set to seconds is to be consistent with the base of the units. This may prevent issues when inputting the loading values into another program.

Figure 3.8 provides sample plots of the pressure loading at various positions on the plate. Each curve in the plot represents the transient pressure profile at a specific point on the plate. This is generated by plotting the pressure values of each row of the loading output file. In this sample, we can see the leading time feature is turned on since the arrival time is not zero. The first curve starting on the left is the transient pressure at the center of the plate. Each curve later in time is the transient pressure for a position located further along the plate. Each of these positions is evenly spaced along the entire plate. We can see that the larger pressures are applied on locations closer to the center of the plate, as expected.

Figure 3.9 is a sample plot of the pressure loading on the plate at various times. Each curve in the plot represents the pressure on the plate at a specific time. This is generated by

	0	8.00E-07	1.60E-06	2.40E-06	3.20E-06	4.00E-06	4.80E-06	5.60E-06	6.40E-06	7.20E-06	8.00E-06	8.80E-06	9.60E-06	1.04E-05	1.12E-05
0	0	8827.371	8604.895	8387.845	8176.091	7969.509	7767.973	7571.365	7379.565	7192.461	7009.938	6831.888	6658.205	6488.783	6323.52
0.375	0	8827.476	8605.066	8388.079	8176.386	7969.861	7768.38	7571.824	7380.074	7193.016	7010.537	6832.53	6658.886	6489.501	6324.274
0.75	0	0	8605.6	8388.803	8177.29	7970.937	7769.62	7573.218	7381.616	7194.698	7012.352	6834.47	6660.945	6491.672	6326.551
1.125	0	0	8606.554	8390.071	8178.859	7972.79	7771.744	7575.6	7384.241	7197.555	7015.429	6837.755	6664.426	6495.34	6330.393
1.5	0	0	0	8391.975	8181.178	7975.505	7774.835	7579.048	7388.029	7201.665	7019.843	6842.458	6669.402	6500.572	6335.869
1.875	0	0	0	8394.632	8184.363	7979.193	7779.001	7583.669	7393.08	7207.124	7025.69	6848.671	6675.961	6507.458	6343.063
2.25	0	0	0	0	8188.547	7983.984	7784.368	7589.584	7399.515	7214.052	7033.084	6856.506	6684.213	6516.104	6352.08
2.625	0	0	0	0	0	7990.014	7791.071	7596.924	7407.461	7222.571	7042.147	6866.082	6694.274	6526.623	6363.031
3	0	0	0	0	0	0	7799.24	7605.818	7417.042	7232.803	7052.994	6877.512	6706.254	6539.121	6376.017
3.375	0	0	0	0	0	0	0	7616.384	7428.374	7244.861	7065.738	6890.904	6720.259	6553.703	6391.142
3.75	0	0	0	0	0	0	0	0	0	7258.832	7080.464	6906.342	6736.369	6570.447	6408.482
4.125	0	0	0	0	0	0	0	0	0	0	7097.231	6923.884	6754.642	6589.408	6428.091
4.5	0	0	0	0	0	0	0	0	0	0	0	0	6775.097	6610.606	6449.987
4.875	0	0	0	0	0	0	0	0	0	0	0	0	0	0	6474.149
5.25	0	0	0	0	0	0	0	0	0	0	0	0	0	0	0
5.625	0	0	0	0	0	0	0	0	0	0	0	0	0	0	0
6	0	0	0	0	0	0	0	0	0	0	0	0	0	0	0
6.375	0	0	0	0	0	0	0	0	0	0	0	0	0	0	0
6.75	0	0	0	0	0	0	0	0	0	0	0	0	0	0	0
7.125	0	0	0	0	0	0	0	0	0	0	0	0	0	0	0
7.5	0	0	0	0	0	0	0	0	0	0	0	0	0	0	0
7.875	0	0	0	0	0	0	0	0	0	0	0	0	0	0	0
8.25	0	0	0	0	0	0	0	0	0	0	0	0	0	0	0
8.625	0	0	0	0	0	0	0	0	0	0	0	0	0	0	0
9	0	0	0	0	0	0	0	0	0	0	0	0	0	0	0

Figure 3.7: Part of a sample output loading file. The left column specifies the location from the center of the plate. The top row indicates the time. The other numbers are the pressure values. Note that these values are for an arbitrary run and not a sample of any cases discussed in this study.

plotting the pressure values of each column of the loading output file. As the time increases, the pressure values decrease but span over more of the plate. Figures 3.10 and 3.11 are close-ups at different locations of Figure 3.9. In each of these figures, one curve is accented to show the intricate nature of this nonuniform loading. The vertical line on the right of each highlighted curve occurs because the loading has not reached further along on the plate at that instance of time. The intricate shapes occur due to the different exponential loading profiles at each location on the plate. In particular, the duration time of each exponential loading profile along the plate does not change monotonically, as seen in Figure 3.4, so when the various exponential loading profiles are combined together at a certain instance in time, it allows for various different and complex loading shapes along the plate.

3.10 Issues and Complications

One of the main issues in this field of study is units. For instance, the scaled distance, Z, can either be in ft/1b$^{1/3}$ or m/kg$^{1/3}$. In some references, there is no indication of which units

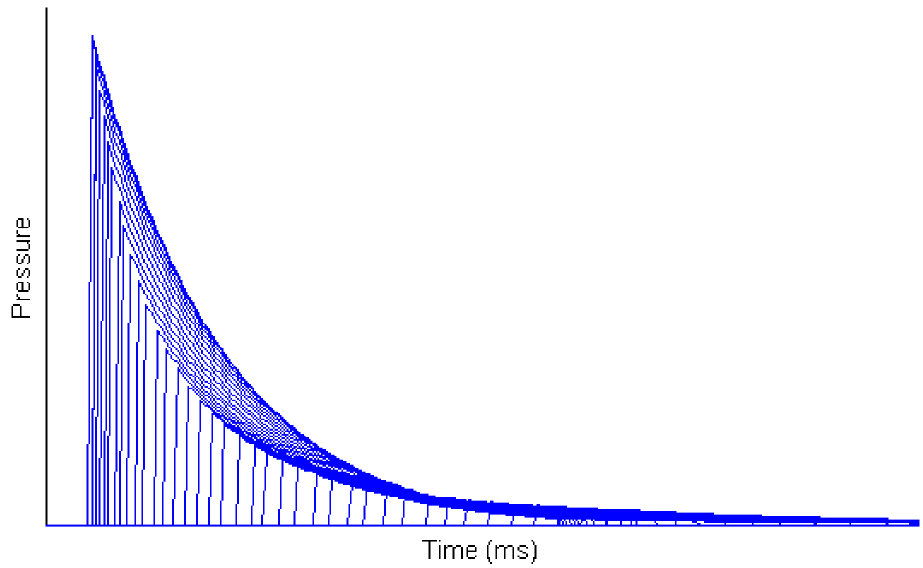

Figure 3.8: Sample plot of the pressure loading at various positions on the plate. Each curve in the plot represents the transient pressure profile at a specific point on the plate. Each of these points is evenly spaced along the entire plate.

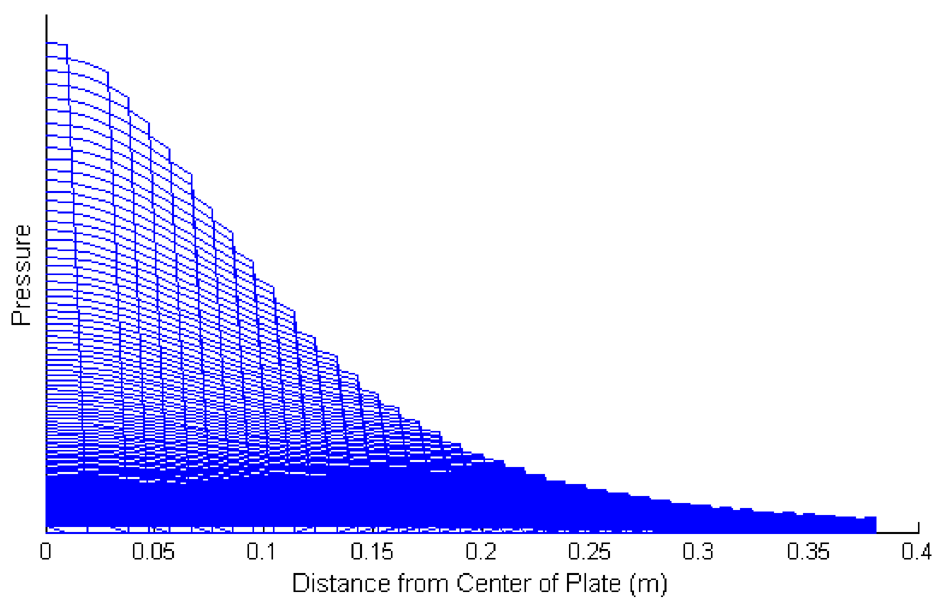

Figure 3.9: Sample plot of the pressure loading on the plate at various times. Each curve in the plot represents the pressure on the plate at a specific time. As the time increases, the pressure values decrease but span over more of the plate.

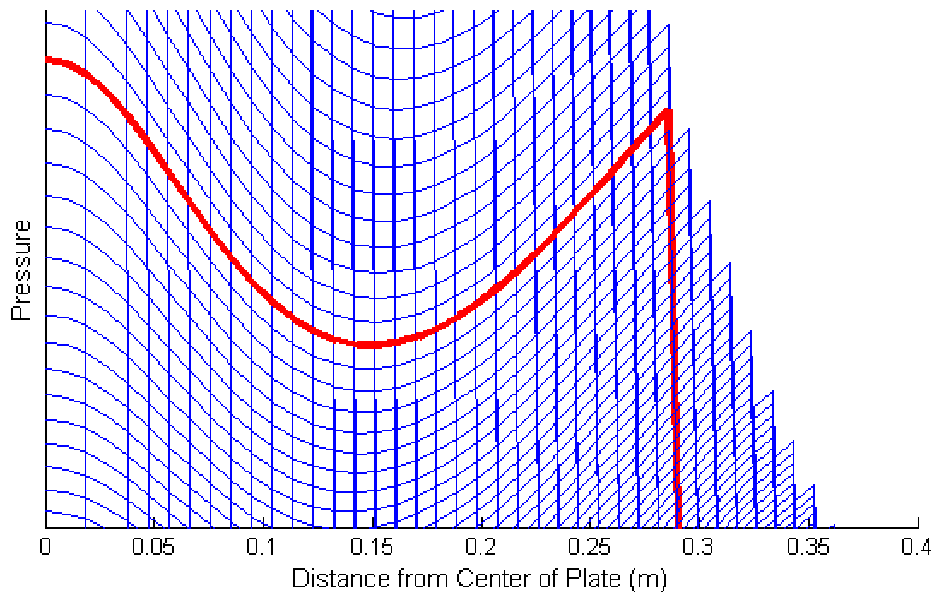

Figure 3.10: Close-up of Figure 3.9. Loading profile of plate at various times.

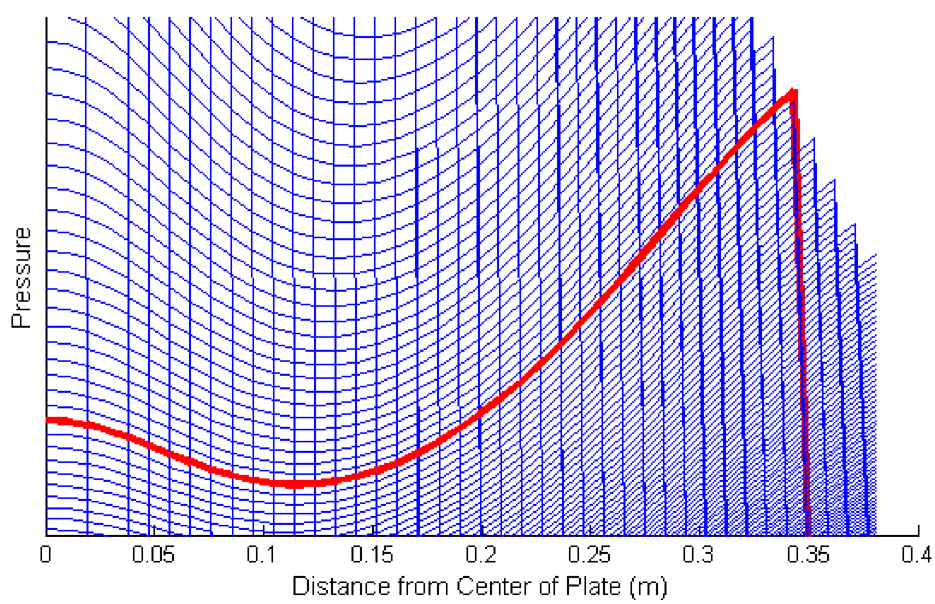

Figure 3.11: Close-up of Figure 3.9. Loading profile of plate at various times.

are being used. For the experimental results given, the setup and explosive configuration were given in English units, however, the results of the plate deflection were given in SI units. In addition, there are some data, such as the dashed lines in Figure 3.4 and Table 3.1, which are only represented in a specific set of units. Therefore, the nonuniform loading program discussed above initially converts all the input values to their proper English unit equivalence and then all the calculations are done in English units. Afterwards, if the user specifies SI units for the results, the proper conversion from English to SI units is made.

Another concern in this field of study is the dependence on empirical data. As mentioned before, the parameter values given in Figure 3.4 were gathered from a collection of various experiments. This, in addition to the scaling and TNT equivalence laws, produce some uncertainty in these values. In particular, there is a greater uncertainty in the parameter values when dealing with small scaled distances, as is the case for this study.

One limitation for this nonuniform loading model is that it works as a pre-process to the response model. This means that the loading model is unable to account for the deformation of the plate which would change the distance from the explosive charge center to the target, as well as the angle the airblast load hits the target. However, since the plate is kept in the elastic region and has small deflections, this limitation is not viewed as critical.

This nonuniform loading model is only used for spherical free-air blasts and not surface bursts which create greater pressures and can also generate Mach stems. It is also designed for an axisymmetric circular plate, therefore the loading it generates is spatially 1-D. Of course while keeping the same methodology, this program can easily be modified to incorporate a 2-D spatial nonuniform loading.

Chapter 4

Analytical Structural Model

The time dependent von Kármán model for circular plates is used to determine the plate deformation in the analytical model. A method for solving the von Kármán model is to assume a deformation shape [49]. For a circular plate, this assumed shape is usually taken as Equation 4.1. This equation has two constants that depend on boundary conditions. The values of these constants have no “real physical” meaning and are just chosen to allow Equation 4.1 to satisfy the boundary condition. In addition, since there are two constants used to satisfy the boundary condition, it is difficult to perform a sensitivity analysis on the boundary. Therefore, a new modified assumed shape is derived by adding torsional springs to the boundary of the circular plate. By doing so, an assumed shape with a single boundary condition parameter, with physical meaning, is created. The solution to the von Kármán equation is then derived for this new assumed shape. Finally, the numerical procedure used to solve for the transverse deflection of the circular plate is described.

4.1 Assumptions

The von Kármán model is a mathematical model for the large deflection of thin elastic plates. According to Szilard [50], a thin plate is typically characterized as having a ratio of thickness to governing length of less than 1/10. Although the von Kármán model is known as a large deflection model, it is only valid for deflections up to the same order as plate thickness, but small compared with the other plate dimensions. This is due to the assumption of small strains and moderately large rotations during its derivation. The assumption of small strains implies Hooke’s law holds. In addition to Hooke’s law, Krichhoff’s hypotheses is assumed to hold. Krichhoff’s hypotheses implies that tractions on the surfaces parallel to the middle surface are negligible and strains vary linearly within the plate thickness. In the derivation the slope everywhere is assumed to be small and the tangential displacements are assumed to be infinitesimal [51]. For this study, we assume axisymmetric plate response and applied pressure loading.

4.2 Derivation of Modified Assumed Shape for von Kármán Model

The well known von Kármán model for circular plates is modified to incorporate torsional springs on the boundary. The goal is to remove the two generic boundary condition constants from the assumed shape and replace them with one constant representing the stiffness of the torsional spring on the boundary of the plate. By modifying this torsional stiffness constant, we can simulate any deflection shape ranging from a fully fixed/clamped plate to a simply supported plate. In real situations there are no fully fixed or simply supported plates. By comparing experimental work to this model, one can determine what the boundary condition of the experimental setup truly is with respect to this assumed shape. In addition, a sensitivity analysis can now easily be performed on the boundary condition.

Figure 4.1 shows the geometry of the plate. We first assume the deformation shape of a circular plate [49]:

$$w(r,t) = h\left(1 + \frac{C_1 r^2}{a^2} + \frac{C_2 r^4}{a^4}\right)\tau(t) \tag{4.1}$$

where w is the deflection of the plate, h is the thickness of the plate, a is the radius of the plate, C_1 and C_2 are boundary condition constants, r is the position from the center of the plate and $\tau(t)$ is the time dependant function of the deflection. Notice how this assumption assumes the deflection is axisymmetric about the center of the plate. In addition, it separates the time dependant part of the response to the shape profile of the response.

The moment caused by a torsional spring is $-K\alpha$, where K is the spring constant and α is the angle of twist. The angle of twist of the boundary is represented by $-\frac{\partial w}{\partial r}$. Therefore the moment of the torsional spring is $(-K)\left(-\frac{\partial w}{\partial r}\right) = K\frac{\partial w}{\partial r}$. At the boundary, where $r = a$, the moment is

$$\left(K\frac{\partial w}{\partial r}\right)\bigg|_{r=a} = Kh\left(\frac{2C_1}{a} + \frac{4C_2}{a}\right) = \frac{2Kh\left(C_1 + 2C_2\right)}{a}. \tag{4.2}$$

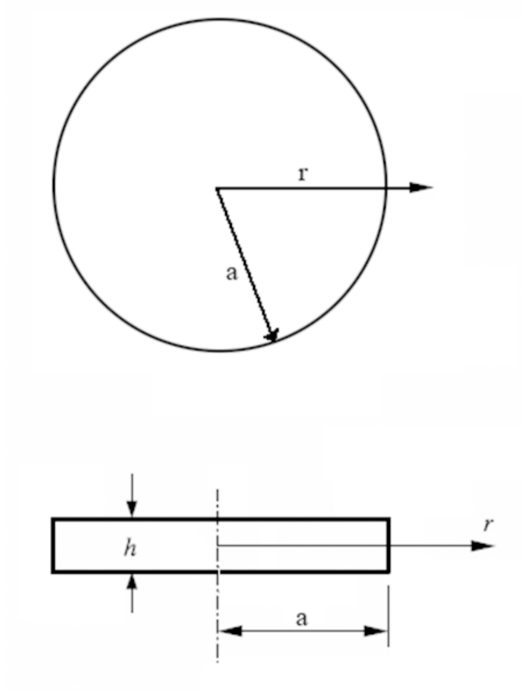

Figure 4.1: Plate geometry.

The internal bending moment per unit length of the circular plate is given by [49, 52]

$$\bar{M}_r = -D\left[\frac{\partial^2 w}{\partial r^2} + \upsilon\left(\frac{1}{r^2}\frac{\partial^2 w}{\partial \theta^2} + \frac{1}{r}\frac{\partial w}{\partial r}\right)\right] \tag{4.3}$$

where

$$D = \frac{Eh^3}{12\left(1-\upsilon^2\right)}.$$

D represents the flexural rigidity of the plate, E is Young's modulus and υ is Poisson's ratio. Since the problem is axisymmetric, the term with $\frac{\partial^2 w}{\partial \theta^2}$ is dropped simplifying Equation 4.3 to

$$\bar{M}_r = -D\left[\frac{\partial^2 w}{\partial r^2} + \upsilon\frac{1}{r}\frac{\partial w}{\partial r}\right]. \tag{4.4}$$

Substituting the shape profile part of Equation 4.1 into Equation 4.4 and multiplying by the circumference of the plate yields

$$M_r = \bar{M}_r \cdot 2\pi r = -\frac{2Dh\left(C_1a^2 + 6C_2r^2 + \nu C_1a^2 + 2\nu C_2r^2\right)}{a^4} \cdot 2\pi r. \tag{4.5}$$

At the boundary, where $r = a$, Equation 4.5 becomes

$$(M_r)|_{r=a} = -\frac{4\pi Dh\left(C_1 + 6C_2 + \nu C_1 + 2\nu C_2\right)}{a}. \tag{4.6}$$

Setting the torsional spring moment, Equation 4.2, and the internal moment of the circular plate at the boundary, Equation 4.6, equal to each other and solving for C_1 gives

$$C_1 = -\frac{2C_2\left(K + 6D\pi + 2D\pi\upsilon\right)}{K + 2D\pi + 2D\pi\upsilon}. \tag{4.7}$$

Substituting Equation 4.7 for C_1 in Equation 4.1 gives

$$w(r,t) = h\left(1 - \frac{2C_2\left(K + 6D\pi + 2D\pi\upsilon\right)r^2}{\left(K + 2D\pi + 2D\pi\upsilon\right)a^2} + \frac{C_2 r^4}{a^4}\right)\tau(t). \tag{4.8}$$

At this point, the assumed deflection shape no longer has one of its original boundary condition constants, C_1. Instead it is replaced by K and D.

Since the deflection at the boundary is zero, $(w)|_{r=a} = 0$, we substitute $r = a$ in Equation 4.8 and solve for C_2.

$$C_2 = \frac{K + 2D\pi + 2D\pi\upsilon}{K + 10D\pi + 2D\pi\upsilon}.$$

Substituting C_2 back into Equation 4.8 gives

$$w(r,t) = h\left(1 - \frac{2\left(K + 6D\pi + 2D\pi\upsilon\right)r^2}{\left(K + 10D\pi + 2D\pi\upsilon\right)a^2} + \frac{\left(K + 2D\pi + 2D\pi\upsilon\right)r^4}{\left(K + 10D\pi + 2D\pi\upsilon\right)a^4}\right)\tau(t). \tag{4.9}$$

This assumed displacement now only has one boundary parameter, the torsional spring constant K. By changing the value of K, the assumed shape function can represent a circular plate that can be simply supported or fully clamped, as well as any level of fixity in between. Figure 4.2 shows plots of Equation 4.9, normalized to $\tau(t) = 1$, for various values of K. The top curve, for $K = 0$ in lb/rad, represents a simply supported plate, while the bottom curve, when $K > 10,000,000,000$ in lb/rad, represents a nearly clamped plate.

4.3 von Kármán Model Solution

To complete the solution of Equation 4.9, $\tau(t)$ is needed. To solve for $\tau(t)$, the two von Kármán equations for polar coordinates are used. The first von Kármán equation is used to determine the constant that satisfies the in-plane boundary condition, which is a fixed

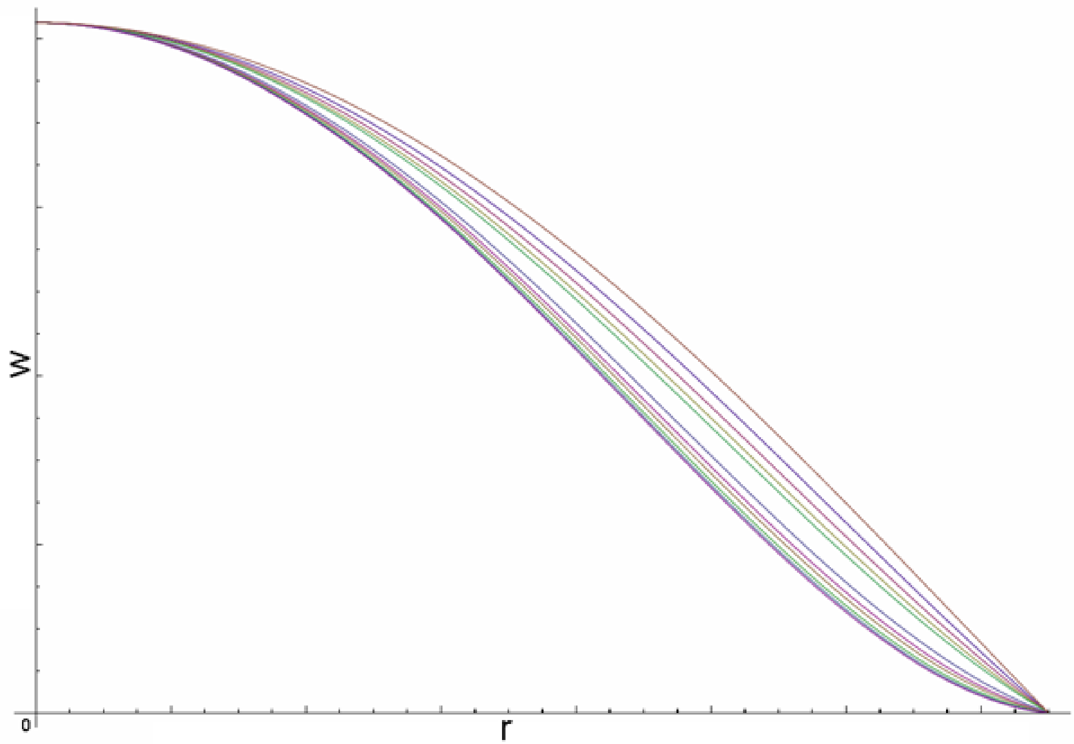

Figure 4.2: Plots of derived shape equation, normalized to $\tau(t) = 1$, for various values of K. The top curve, when $K = 0$ in lb/rad, represents a simply supported plate, while the bottom curve, when $K > 10,000,000,000$ in lb/rad, represents a nearly clamped plate. Plate properties used are shown in Table 4.1.

boundary in this work. The second von Kármán equation is used to set up the nonlinear ordinary differential equation to solve for $\tau(t)$.

The first von Kármán equation in cylindrical coordinates is [38, 49]

$$\nabla^4 F = -\frac{E}{r}\frac{\partial w}{\partial r}\frac{\partial^2 w}{\partial r^2}, \tag{4.10}$$

where ∇^4 is the biharmonic operator and F is the Airy Stress function. The Airy Stress function is defined as [52]

$$N_r = \frac{1}{r}\frac{dF}{dr} \tag{4.11a}$$

and

$$N_t = \frac{d^2 F}{dr^2}, \tag{4.11b}$$

where N_r and N_t are the in-plane membrane stresses in the radial and tangential direction, respectively. The biharmonic equation

$$\nabla^4 F = \frac{1}{r}\frac{d}{dr}\left\{r\frac{d}{dr}\left[\frac{1}{r}\frac{d}{dr}\left(r\frac{dF}{dr}\right)\right]\right\} + \frac{2}{r^2}\frac{\partial^4 F}{\partial\theta^2\partial r^2} + \frac{1}{r^4}\frac{\partial^4 F}{\partial\theta^4} - \frac{2}{r^3}\frac{\partial^3 F}{\partial\theta^2\partial r} + \frac{4}{r^4}\frac{\partial^2 F}{\partial\theta^2} \tag{4.12}$$

can be simplified by dropping the θ terms due to axisymmetry, yielding

$$\nabla^4 F = \frac{1}{r}\frac{d}{dr}\left\{r\frac{d}{dr}\left[\frac{1}{r}\frac{d}{dr}\left(r\frac{dF}{dr}\right)\right]\right\}. \tag{4.13}$$

Inserting this simplified biharmonic equation into Equation 4.10 gives

$$\frac{1}{r}\frac{d}{dr}\left\{r\frac{d}{dr}\left[\frac{1}{r}\frac{d}{dr}\left(r\frac{dF}{dr}\right)\right]\right\} = -\frac{E}{r}\frac{\partial w}{\partial r}\frac{\partial^2 w}{\partial r^2}. \tag{4.14}$$

We now reverse operate on the right side of Equation 4.14 to obtain the Airy Stress function, F. All the constants of integration are dropped while the reverse operation is being performed. This is because these constants would vanish when placed back into the left side of Equation 4.14 and therefore the equation will still be satisfied. By letting the Airy Stress function take the form [38, 49]

$$F(r,t) = f(r)\tau^2(t), \tag{4.15}$$

we get

$$f(r) = \text{see Appendix A.} \tag{4.16}$$

Then $C_3Eh^2\left(\frac{r}{a}\right)^2$ is added to $f(r)$. The expression $C_3Eh^2\left(\frac{r}{a}\right)^2$ which is added to $f(r)$ has the same form as one of the constants of integration and therefore will drop out when put back into the lefthand side of Equation 4.14 and still satisfy the equation. However, this added expression allows the Airy Stress function to satisfy the in-plane boundary condition. C_3 is the constant determined from the in-plane boundary condition.

In order to derive the equation for in-plane displacement in polar coordinates, we begin with the strain equation in the radial direction [52],

$$\epsilon_r = \frac{\partial u}{\partial r} + \frac{1}{2}\left(\frac{\partial w}{\partial r}\right)^2, \tag{4.17}$$

where ϵ_r is the radial strain and u is the in-plane displacement. This strain equation, which is also used in the derivation of the two von Kármán equations, is valid for moderately large deflections that are on the order of magnitude of the plate's thickness but are still small compared with the other plate dimensions. In addition, retaining the second term on the right of Equation 4.17 is the difference between the von Kármán model and the linear plate theory [51]. Solving for u in Equation 4.17 gives

$$u = \int_0^a \left[\epsilon_r - \frac{1}{2}\left(\frac{\partial w}{\partial r}\right)^2\right] dr. \tag{4.18}$$

Inserting the stress-strain relationship,

$$\epsilon_r = \frac{1}{E}\left(N_r - \nu N_t\right),$$

and Equations 4.11a and 4.11b into Equation 4.18, the expression for the in-plane displacement in terms of the Airy Stress function is derived,

$$u = \int_0^a \left[\frac{1}{E}\left[\frac{\partial F}{\partial r}\frac{1}{r} - \nu\frac{\partial^2 F}{\partial r^2}\right] - \frac{1}{2}\left(\frac{\partial w}{\partial r}\right)^2\right] dr. \tag{4.19}$$

Setting the in-plane displacement equal to zero, $u = 0$, we insert the Airy Stress function and the assumed deformation shape, Equation 4.8, into Equation 4.19. Then solving for the in-plane boundary condition constant, we find

$$C_3 = \text{see Appendix A.}$$

The complete Airy Stress function is then

$$F(r,t) = \text{see Appendix A.} \tag{4.20}$$

The second von Kármán equation in Leissa [49] is missing terms. The proper equation is given in Timoshenko [52]. The proper second von Kármán equation in polar coordinates is [38]

$$D\nabla^4 w + \rho h \frac{\partial^2 w}{\partial t^2} = \frac{h}{r}\frac{\partial F}{\partial r}\frac{\partial^2 w}{\partial r^2} + \frac{h}{r}\frac{\partial w}{\partial r}\frac{\partial^2 F}{\partial r^2} + P(r,t), \tag{4.21}$$

where ρ is the density of the plate and P is the loading pressure on the plate. Inserting Equation 4.20 and Equation 4.9 into Equation 4.21 yields an equation of

$$C_4(r)\ddot{\tau}(t) + C_5\tau(t) + C_6(r)\tau^3(t) - P(r,t) = 0 = \bar{R}, \tag{4.22}$$

where

$$\begin{aligned}
C_4(r) &= \rho h^2 + 8C_7 - \frac{2\rho h^2 r^2}{a^2} - \frac{8C_7 r^2}{a^2} + \frac{\rho h^2 r^4}{a^4} \\
C_5 &= \frac{64hD(K + 2D\pi + 2D\pi\nu)}{(K + 10D\pi + 2D\pi\nu)\,a^4} \\
C_6(r) &= \text{see Appendix A} \\
C_7 &= \frac{\rho h^2 r^2 D\pi}{(K + 10D\pi + 2D\pi\nu)\,a^2}.
\end{aligned}$$

As Bauer [38] mentions, Equation 4.20 and Equation 4.9 satisfy the boundary conditions as well as Equation 4.10, but one cannot expect them to also exactly satisfy Equation 4.21. Therefore the Galerkin method is used to obtain an approximate solution that satisfies all the governing equations and boundary conditions. The Galerkin method [50, 53] requires that

$$\int_0^{2\pi}\int_0^a \bar{R}\frac{w(r)}{h} r\,dr\,d\theta = 0. \tag{4.23}$$

The axisymmetric assumption implies $\int_0^{2\pi} d\theta = 2\pi$. Dividing Equation 4.23 by $\frac{2\pi}{h}$ yields

$$\ddot{\tau}(t)\int_0^a C_4(r)w(r)r\,dr + \tau(t)\int_0^a C_5 w(r)r\,dr + \tau^3(t)\int_0^a C_6(r)w(r)r\,dr - \int_0^a P(r,t)w(r)r\,dr = 0. \tag{4.24}$$

Performing the first three integrations of Equation 4.24 gives the nonlinear equation of motion

$$\psi\ddot{\tau}(t) + \beta\tau(t) + \gamma\tau^3(t) = \int_0^a P(r,t)w(r)r\,dr, \tag{4.25}$$

where

$$
\begin{aligned}
\psi &= \frac{80a^2h^2\rho C_8^2}{3} + 2a^2h^2\rho C_8 + \frac{a^2h^2\rho}{10} \\
\beta &= \frac{32hD\left(800C_8^2 + 20C_8 - 1\right)}{3a^2} \\
\gamma &= \text{see Appendix A} \\
C_8 &= \frac{D\pi}{5\left(K + 10D\pi + 2D\pi\nu\right)}.
\end{aligned}
$$

Now, plate properties, the value of K, and the pressure loading can be substituted into Equation 4.25 and we can solve for $\tau(t)$ numerically. Once $\tau(t)$ is determined, it can be substituted back into Equation 4.9 to obtain the plate deflection time-history or just multiplied by h to obtain the transient deflection at the center of the plate.

4.4 Numerical Method for Solving Structural Response

4.4.1 MATLAB

A MATLAB program is written to numerically solve Equation 4.25 for the plate's response. This program generates the nonuniform loading (discussed in Chapter 3) and solves for the response. MATLAB was chosen because of its simplicity to program, it is available and it also generates professional graphical results. If the models were more complicated and the runs took a long time to finish, perhaps a faster programming language would have been used, such as C or Fortran.

4.4.2 Runge-Kutta

To solve for $\tau(t)$ in Equation 4.25, a Runge-Kutta method is used. The Runge-Kutta method is a self-starting numerical method used to solve ordinary differential equations. As mentioned by Jaluria [54], the method has a high level of accuracy and good stability, it is simple to program, is applicable in a wide variety of problems, and exhibits an increased accuracy by decreasing the time step size. In this study, the classical fourth-order Runge-Kutta method is used to obtain the accuracy of a Taylor series expansion of the fourth order. The Runge-Kutta method uses a weighted average of the predicted slopes of the equation within the current time step.

Implementation of Runge-Kutta Method

The elastic Equation 4.25 is of the form

$$\psi\ddot{\tau}(t) + \beta\tau(t) + \gamma\tau^3(t) = \tilde{P}(t), \tag{4.26}$$

where

$$\tilde{P}(t) = \int_0^a P(r,t)w(r)rdr.$$

Equation 4.26 is converted into a system of first-order, ordinary differential equations, Equation 4.27, and then solved by implementing the Runge-Kutta method, Equation 4.28. By setting

$$\begin{aligned} \frac{d\tau}{dt} &= g \\ \frac{dg}{dt} &= \frac{\tilde{P}(t) - \beta\tau(t) - \gamma\tau^3(t)}{\psi}, \end{aligned} \tag{4.27}$$

the set of equations to be solved is

$$\begin{aligned} g_{i+1} &= g_i + \frac{J_1' + 2J_2' + 2J_3' + J_4'}{6} \\ \tau_{i+1} &= \tau_i + \frac{J_1 + 2J_2 + 2J_3 + J_4}{6}, \end{aligned} \tag{4.28}$$

where

$$\begin{aligned} J_1' &= \frac{\Delta t}{\psi}(\tilde{P}(t) - \beta\tau_i - \gamma\tau_i^3) \\ J_2' &= \frac{\Delta t}{\psi}\left[\tilde{P}(t) - \beta\left(\tau_i + \frac{J_1}{2}\right) - \gamma\left(\tau_i + \frac{J_1}{2}\right)^3\right] \\ J_3' &= \frac{\Delta t}{\psi}\left[\tilde{P}(t) - \beta\left(\tau_i + \frac{J_2}{2}\right) - \gamma\left(\tau_i + \frac{J_2}{2}\right)^3\right] \\ J_4' &= \frac{\Delta t}{\psi}\left[\tilde{P}(t) - \beta(\tau_i + J_3) - \gamma(\tau_i + J_3)^3\right] \\ J_1 &= \Delta t g_i \\ J_2 &= \Delta t\left(g_i + \frac{J_1'}{2}\right) \\ J_3 &= \Delta t\left(g_i + \frac{J_2'}{2}\right) \\ J_4 &= \Delta t(g_i + J_3') \end{aligned}$$

and Δt is the time increment between the last two time steps. Since the plate is initially at rest and undeformed, the initial values for g and τ in Equation 4.28 are set to zero. The deflection at the center of the plate, w_{i+1}, for every time step, i, is then obtained via

$$w_{i+1} = h\tau_{i+1}. \tag{4.29}$$

4.5 Parameter Values

Table 4.1 lists the values used in this study for the analytical model, unless otherwise stated. The plate dimensions and properties (4340 steel) were chosen to match the experimental setup of the Department of Homeland Security. Note that ρ needs to be converted to 734.99 $\text{lb}_f\ \text{ms}^2/\text{in}^4$ to be used in the equations derived within this chapter. The value for K is extremely large to represent a fully clamped plate. The time step was chosen to be small enough to capture the loading and plate response accurately, while keeping the runtime of the program to a minimum.

Variable	Value
a	15 in
h	0.819 in
ρ	0.284 lb_m/in^3
ν	0.29
E	2.97×10^7 psi
K	10^{27} in lb/rad
Δt	8×10^{-4} ms
P_0	0 psi
Radial Divisions	40
TNT Equiv i	1.19
TNT Equiv P	1.37

Table 4.1: Parameter values used for the analytical model.

Chapter 5

Finite Element Models

In addition to the analytical model, two finite element models are developed. These finite element models are used, in addition to the experimental data, for verification of the analytical model as well as the loading model. This chapter explains the specific details of the finite element models which were created using ANSYS Workbench®. Although the geometries are labeled as plates, the finite element models utilizes 3-D solid elements.

5.1 ANSYS Workbench

ANSYS Workbench is a commercially available finite element program capable of performing complex simulations. It has a graphical user interface which aids the setup of the simulation. In addition, the results of the simulations are easy to handle within ANSYS Workbench.

ANSYS Workbench 2.0, part of the ANSYS® 12.0 package, incorporates an explicit solver. An explicit solver would be ideal for this type of problem due to the small time steps needed, however, when the explicit solver is enabled, it is unable to apply the spatially and time dependant surface loading on the plate. Therefore the implicit solver had to be used. For this study, a flexible dynamic analysis in ANSYS Workbench, which comes in the ANSYS 11.0 package, was used.

Since the experimental results were given in SI units, the finite element models were created in SI units. This includes the plate geometries and loading.

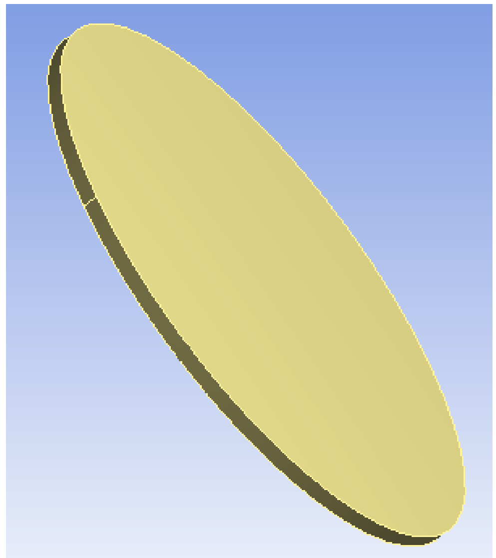

Figure 5.1: Simplified plate geometry (Comp-C). Flat circular plate with constant thickness.

5.2 Geometries

Two different geometries are used to model the plate. The first is a thin circular plate with constant thickness throughout. This simplified plate model, shown in Figure 5.1, will be referred as Comp-C. This circular plate has a radius of 15 in (0.381 m) and a thickness of 0.819 in (0.0208 m).

The second geometry, shown in Figure 5.2, represents the actual witness plate geometry. This includes the fillet to the thicker border of the plate as well as the 36 evenly spaced bolt holes. This geometry has an outer radius of 18 in (0.4572 m). The inner thickness is 0.819 in (0.0208 m) and the thicker border is 1.25 in (0.03175 m). Figure 5.3 shows a schematic with dimensions of the actual witness plate. This actual plate model will be referred as Comp-A.

5.3 Mesh

ANSYS Workbench automatically determines which element type with which to mesh the geometry. For Comp-C, it chose ANSYS element SOLID186. This is a 3-D 20-node solid element. Figure 5.4 shows the meshed surface of Comp-C which consists of 912 elements

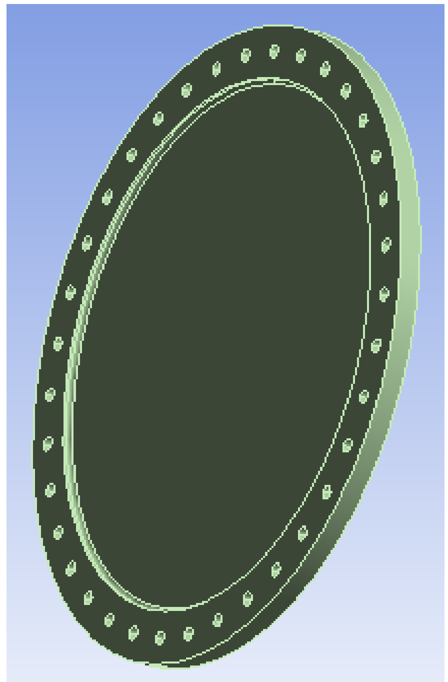

Figure 5.2: Actual plate geometry (Comp-A). The plate has a thicker outer edge with bolt holes used to attach the plate to the bulkhead fixture.

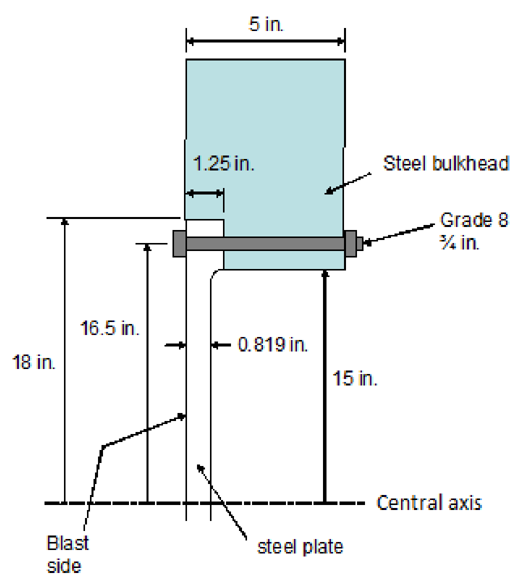

Figure 5.3: Schematic with dimensions of the experimental setup [2].

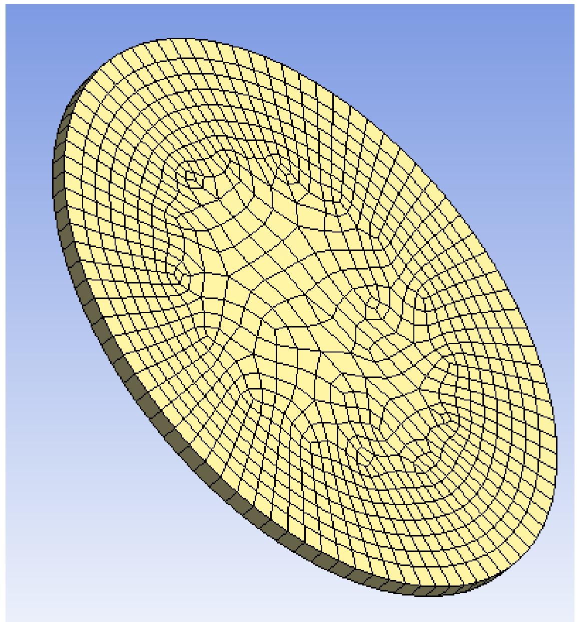

Figure 5.4: Mesh of the simplified plate geometry (Comp-C) which consists of 3-D 20-node solid elements.

and 6607 nodes.

For Comp-A, ANSYS Workbench chose ANSYS element SOLID187. This is a 3-D 10-node tetrahedral solid element. Figures 5.5 - 5.7 show the meshed surfaces of Comp-A which consists of 6297 elements and 13034 nodes. We note that the meshes generated for Comp-A and Comp-C are not axisymmetric.

5.4 Boundary Conditions

For Comp-C, the outer side of the plate, as indicated in Figure 5.8, is fixed in all directions. For Comp-A, the outer side as well as the surface of the plate with bolt holes which rests on the bulkhead are fixed in all directions. Figure 5.9 shows the two surfaces that are fixed for Comp-A. A test was conducted to see if the outer side supports on Comp-A affected the deflection results. A simulation was conducted without the outer side of the plate fixed. The conclusion is that it does not affect the results significantly.

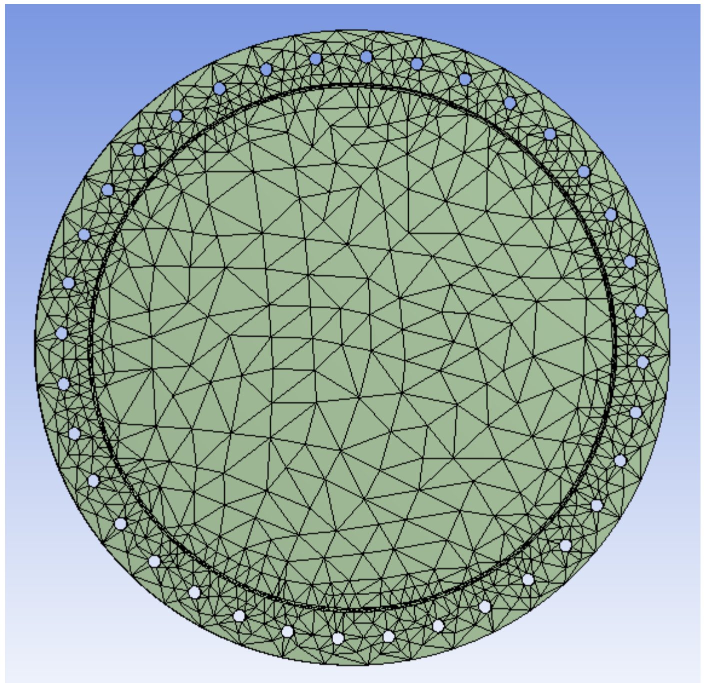

Figure 5.5: Mesh of the actual plate geometry (Comp-A) which consists of 3-D 10-node tetrahedral solid elements.

5.5 Loading

The pressure loadings on the plate in the finite element models are applied as surface forces. ANSYS Workbench reads in the loading table, which is generated from the loading program, and applies the spatial and time dependent loading on the proper surface of the plate.

Since Comp-C and Comp-A have different outer radii, the number of radial divisions for each model is different. For Comp-C, the radial divisions is 40 to match the analytical model. However, for Comp-A, the radial divisions is 48. This guarantees that, up to the radius of Comp-C, the locations where the loading is calculated and applied are the same for both Comp-C and Comp-A.

The time steps for the loading files are set at 8×10^{-4} ms to match the analytical model.

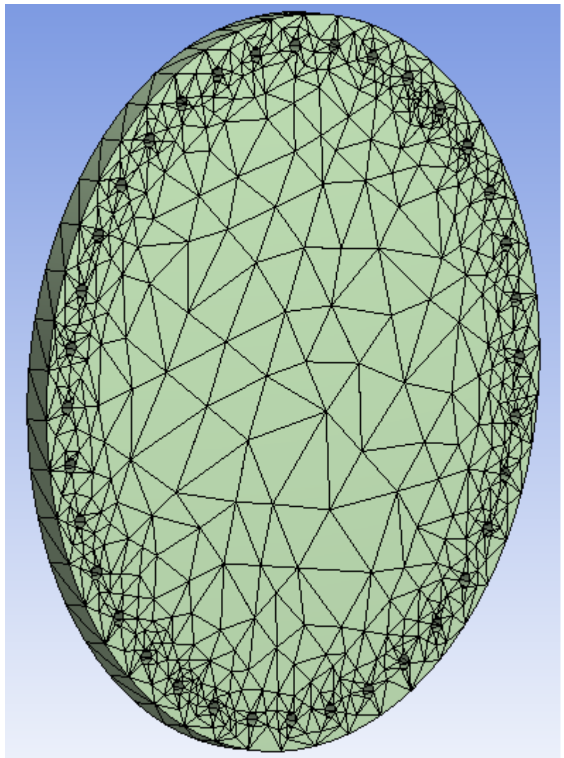

Figure 5.6: Mesh of the actual plate geometry (Comp-A) which consists of 3-D 10-node tetrahedral solid elements.

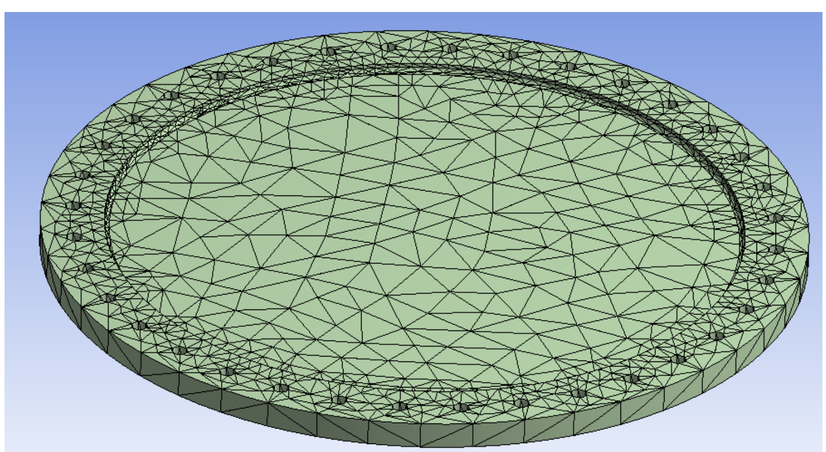

Figure 5.7: Mesh of the actual plate geometry (Comp-A) which consists of 3-D 10-node tetrahedral solid elements.

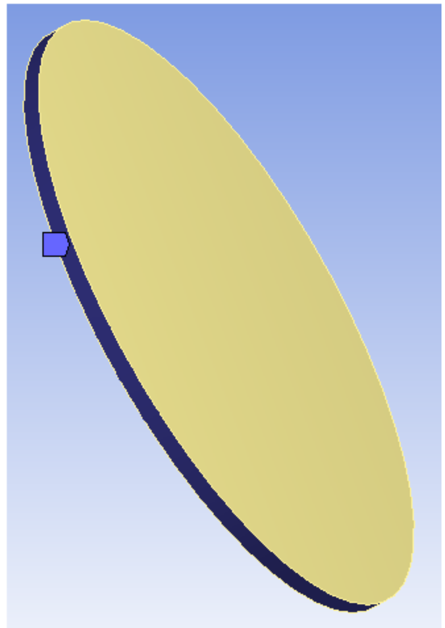

Figure 5.8: Fixed support of the simplified plate geometry (Comp-C). The outer surface along the thickness of the plate is fixed.

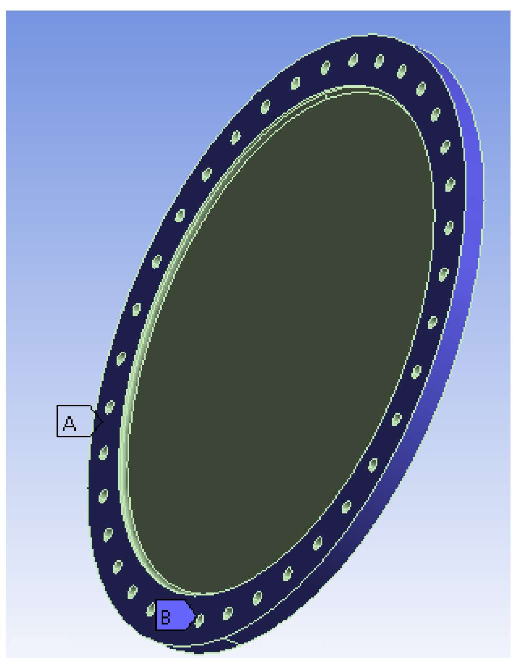

Figure 5.9: Fixed support of the actual plate geometry (Comp-A). The outer surface along the thickness of the plate is fixed as well as the bolted surface which rests against the bulkhead.

5.6 Material Properties and Parameter Values

ANSYS Workbench has libraries of material properties, of which the structural steel material library was used. The values for Young's modulus and Poisson's ratio were slightly modified to match the actual 4340 steel plate properties [55]. Table 5.1 lists the material properties used in the finite element models. β is the material damping coefficient, which is derived in the following section.

The finite element time steps are set to an initial value of 4×10^{-4} ms, which is also the maximum time step allowed. The minimum time step allowed is set to 1×10^{-4} ms.

Variable	Value
E	2.05×10^{11} Pa
ν	0.29
ρ	7850 kg/m^3
β	4.0258×10^{-5}

Table 5.1: Material property values used for the finite element models.

5.6.1 Calculating Material Damping Coefficient for ANSYS Workbench

The material (Beta) damping coefficient used in ANSYS Workbench is defined as

$$\beta = \frac{2\zeta}{\omega_n},$$

where 2ζ is the structural damping factor and ω_n is the natural frequency. In order to determine the material damping properties of the witness plate, the Beta damping value is extracted from the experimental results using the logarithmic decrement technique [56]. The equations for the logarithmic decrement are

$$\bar{\delta} = \ln\left(\frac{x_1}{x_2}\right)$$

and

$$\zeta = \frac{\bar{\delta}}{\sqrt{4\pi^2 + \bar{\delta}^2}},$$

where x_1 is the amplitude of the first maximum peak and x_2 is the amplitude of the second maximum peak. Since the response is an underdamped system, $\zeta^2 < 1$, the equation for the undamped natural frequency is

$$\omega_n = \frac{2\pi}{T_d\sqrt{1-\zeta^2}},$$

where T_d is the period of the damped system which can be calculated by subtracting the time of the second maximum peak from the time of the first maximum peak.

This calculation has been done for two of the experimental results. Although both experimental results give slightly different Beta damping values, they are very similar and therefore the Beta damping value derived from one of the experimental results (Case 2 which is defined in the following chapter), $\beta = 4.0258 \times 10^{-5}$, is used for all the finite element models. We note that $\zeta = 3.8354 \times 10^{-2}$ for this particular case.

Chapter 6

Results and Discussions

This chapter presents plate deformation due to near field explosions. The loading and structural models along with experimental data are compared. The results are shown as surface contours of the deformed plate, maximum center plate deflections and strains. To show the importance of nonuniform loading for near field explosions, displacements with uniform and nonuniform loading are compared. In addition, to validate the proposed loading model, displacements were obtained using the averaged TNT equivalence factors for pressure and impulse and compared to the proposed loading model, which uses each of the factors individually to generate loading parameters. All the results validate the loading and structural models proposed.

6.1 Models and Cases

The results from the analytical and computational finite element models will be compared with experimental results provided by The Department of Homeland Security [2]. The Department of Homeland Security provided four sets of experimental results, which we call Case 1 through Case 4. The three plate models (analytical, Comp-A and Comp-C) were run for each of these cases. The ordering from greatest to least for standoff distance, charge mass and scaled distance is given in Table 6.1.

Standoff Distance:	Case 2 $>$ Case 3 $>$ Case 4 $>$ Case 1
Charge Mass:	Case 2 $=$ Case 3 $>$ Case 1 $>$ Case 4
Scaled Distance:	Case 2 $>$ Case 4 $>$ Case 1 $>$ Case 3

Table 6.1: Comparison of standoff distance, charge mass and scaled distance values for the four cases.

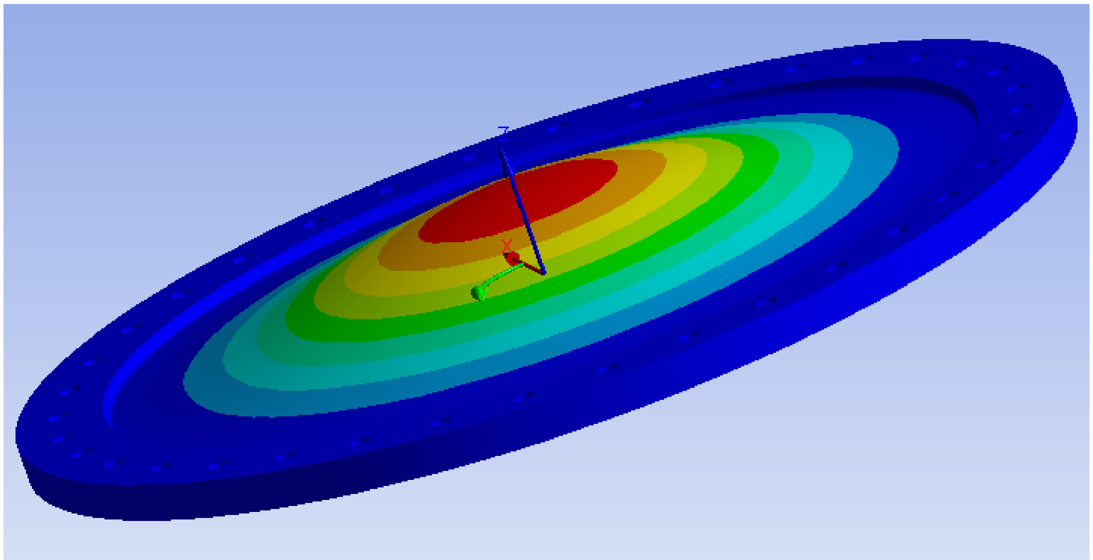

Figure 6.1: ANSYS Workbench surface deformation contour for Comp-A model.

6.2 Surface Deformation Contours and Axisymmetry

We wish to first demonstrate that the plate behaves correctly qualitatively.

Figures 6.1 - 6.4 depict the deformation of the witness plate at a specific time for Comp-A and Figures 6.5 - 6.8 for Comp-C. All the cases have similar looking deformation contours. An experimental data deformation contour is shown in Figure 6.9. The finite element models have similar deformation contours as the experimental data. One important observation to note is that the responses are axisymmetric, as can easily be seen in Figures 6.3 and 6.7. This gives reassurance that the loading table in the finite element models are being applied axisymmetrically on the witness plate.

To verify the axisymmetric response in the experimental data, the transverse displacement along four diameter lines on the plate were superimposed. Each of these transverse displacement lines represent a straight line on the plate's surface oriented at 0°, 45°, 90° and 135° and shown in Figure 6.10. Since all four of the transverse deformation lines essentially match, the experimental response of the plate is shown to be axisymmetric. Note that the deformations in these contour figures are exaggerated.

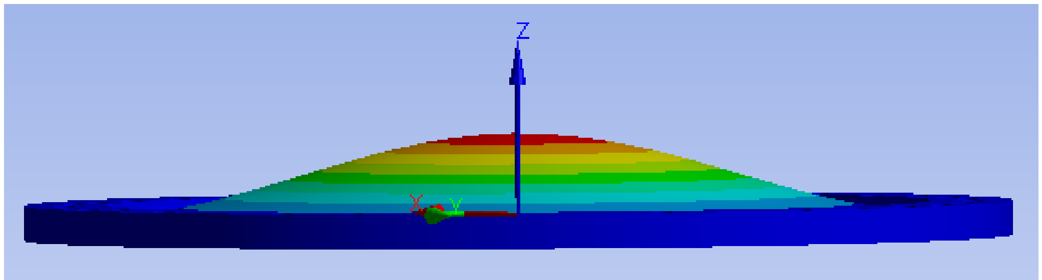

Figure 6.2: Side view of ANSYS Workbench surface deformation contour for Comp-A model.

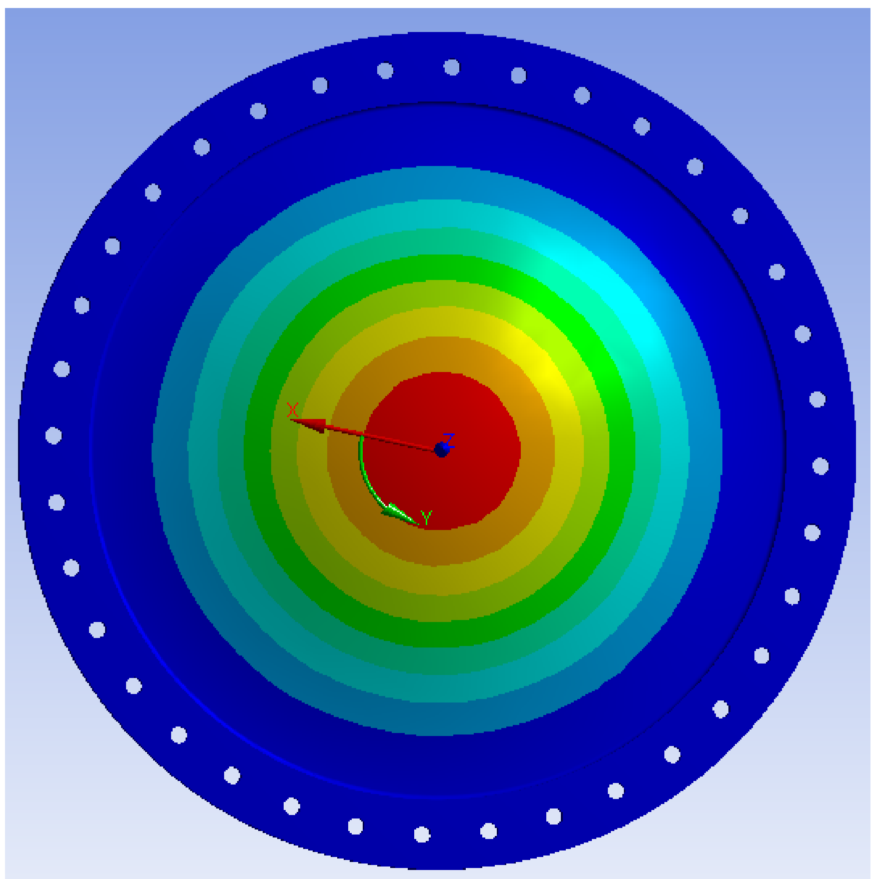

Figure 6.3: Top view of ANSYS Workbench surface deformation contour for Comp-A model. This view shows the axisymmetric deformation.

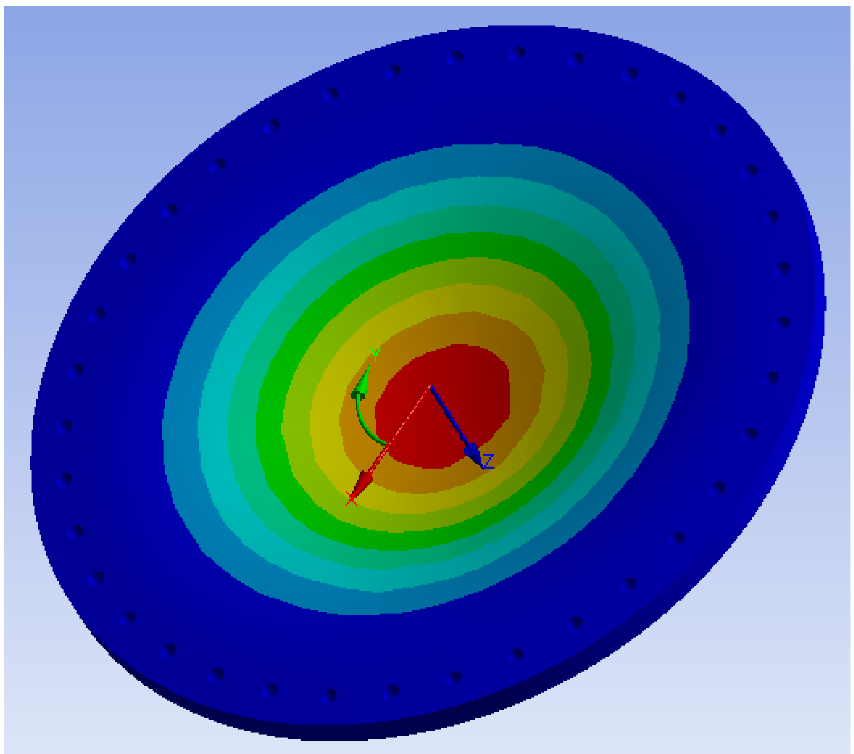

Figure 6.4: Bottom of the ANSYS Workbench surface deformation contour for Comp-A model.

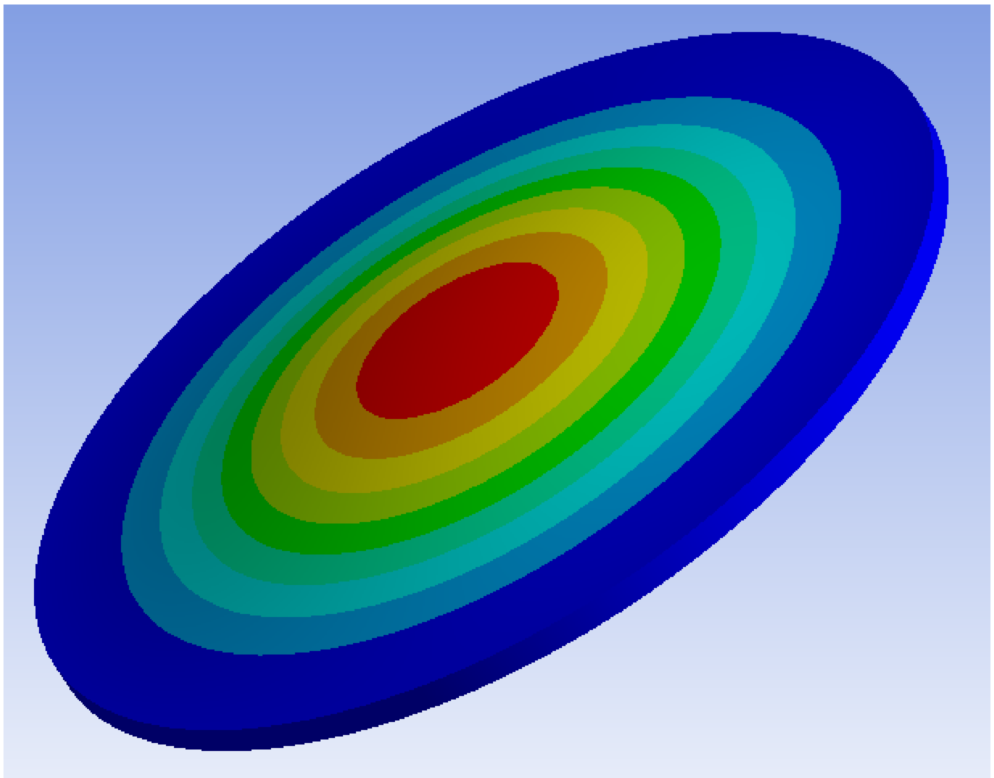

Figure 6.5: ANSYS Workbench surface deformation contour for Comp-C model.

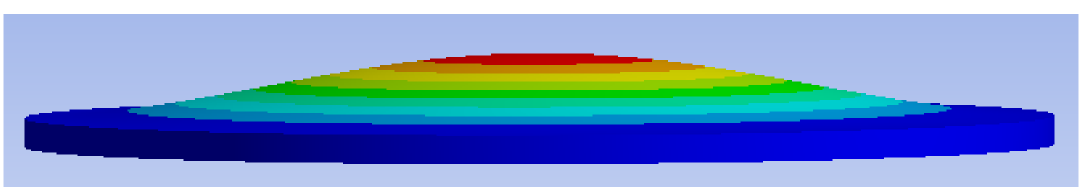

Figure 6.6: Side view of ANSYS Workbench surface deformation contour for Comp-C model.

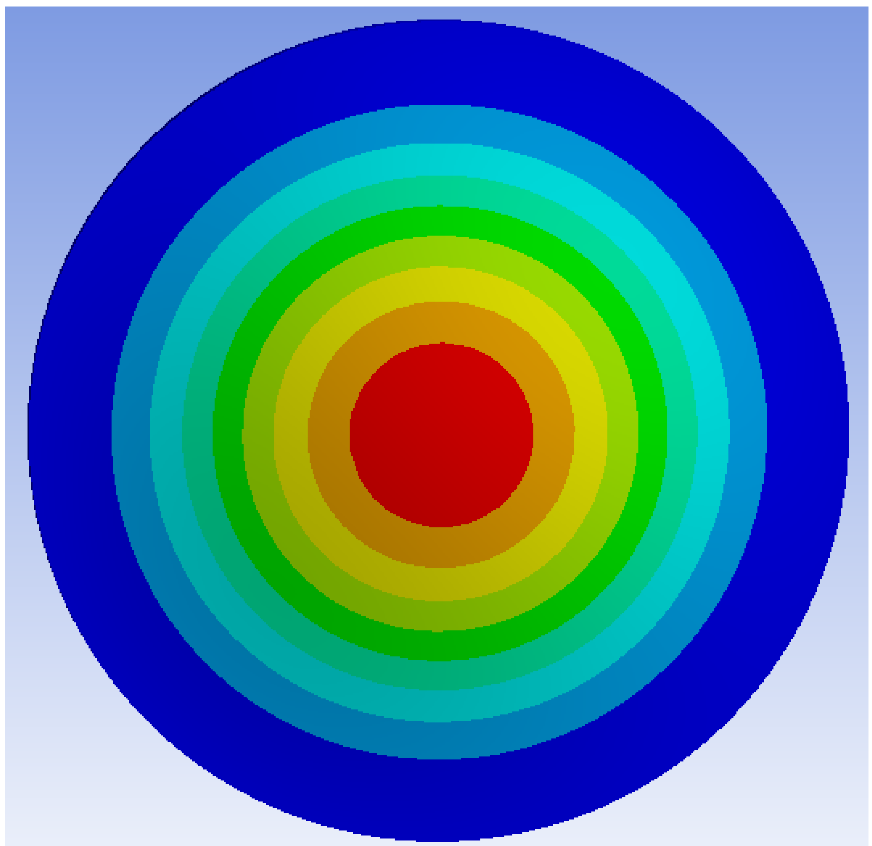

Figure 6.7: Top view of ANSYS Workbench surface deformation contour for Comp-C model. This view shows the axisymmetric deformation.

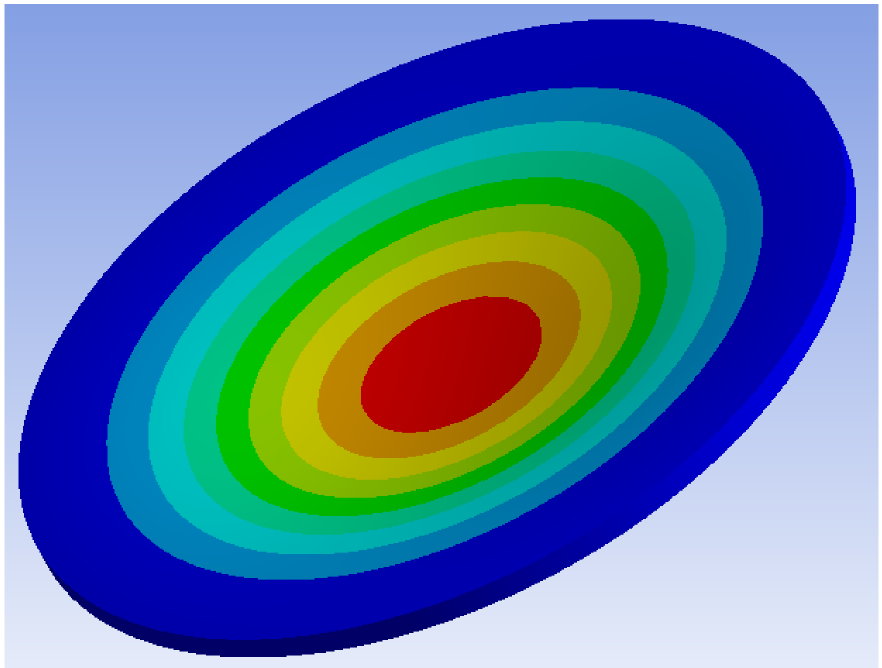

Figure 6.8: Bottom of the ANSYS Workbench surface deformation contour for Comp-C model.

6.3 Maximum Center Plate Deflection

Our primary interest is to calculate maximum deflections. For our axisymmetric circular plate, the maximum deflection occurs at the center of the plate. Therefore, the following results are for the plate's center, unless otherwise stated. Figures 6.11 - 6.14 show the transient transverse displacement for Cases 1 - 4, respectively. Each figure shows the results for the experiment, analytical model and the two finite element models, Comp-A and Comp-C.

By examining these results, it is apparent that while the analytical model does not incorporate any damping, the experimental and finite element models contain damping. The Comp-A and Comp-C models incorporate material damping with a damping factor extracted from the experimental results of Case 2. By observing each local maximum of the plate's deflection in Figures 6.11 and 6.12, it appears that this material damping factor is suitable for both Cases 1 and 2 because the amplitudes of the finite element models match very well with the experimental data. Unfortunately, the experimental data provided

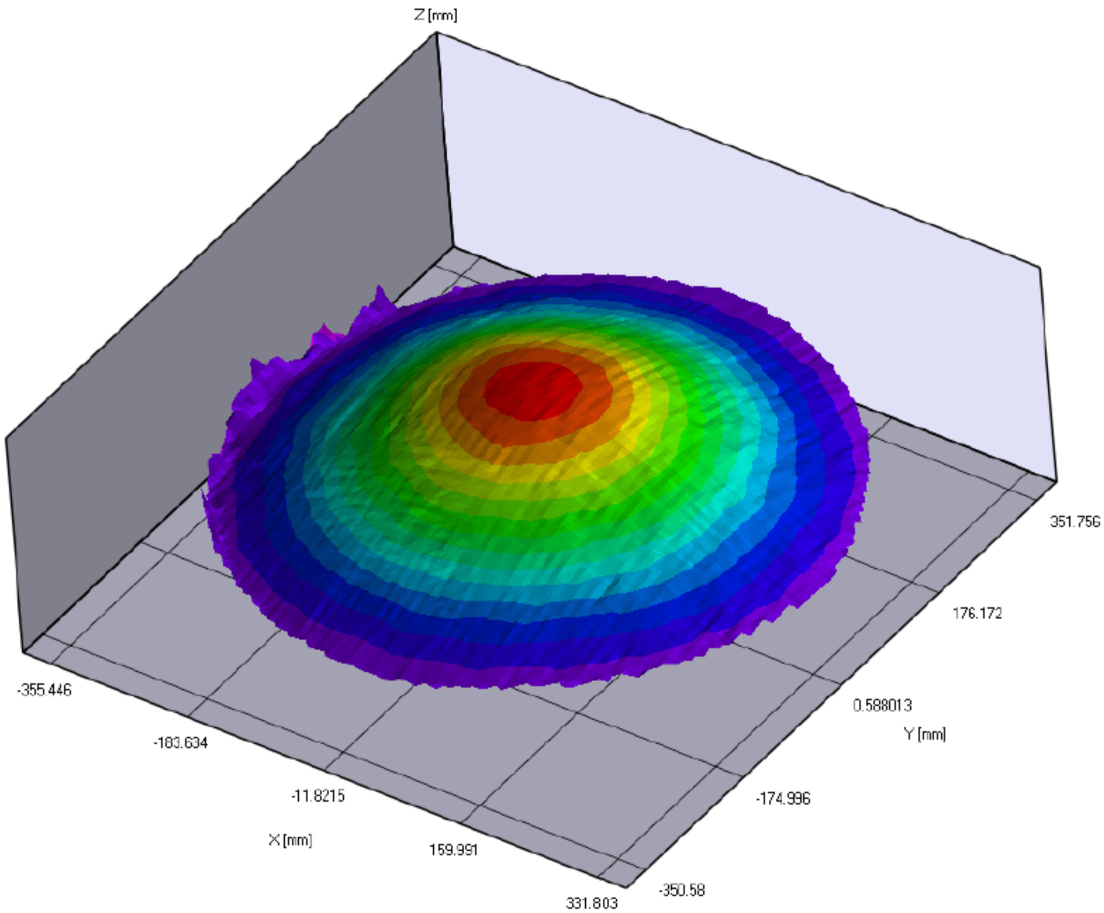

Figure 6.9: Contour of experimental data [2].

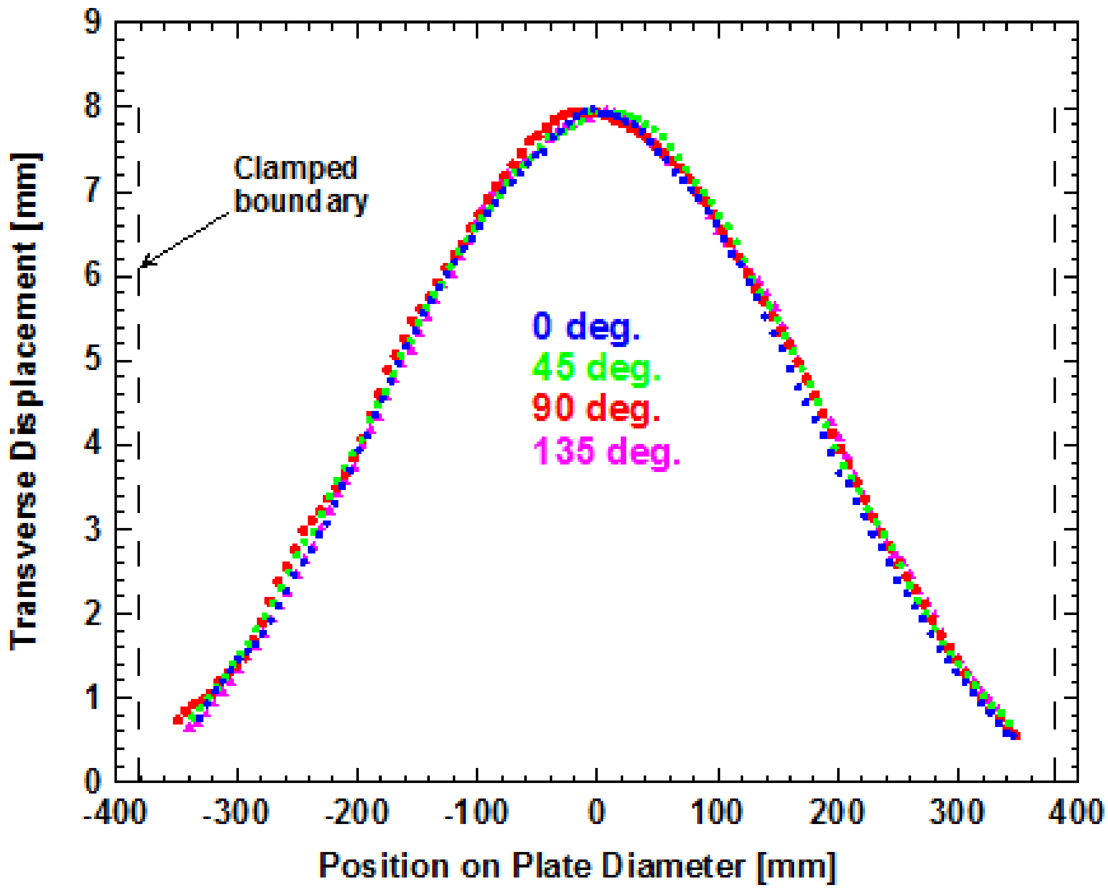

Figure 6.10: Experimental data showing the plate's axisymmetric response to the explosion [2]. Each of the transverse displacement lines represents a straight line on the plate's surface oriented at 0°, 45°, 90° and 135°.

for Cases 3 and 4, Figures 6.13 and 6.14, did not contain more than one period of plate oscillation so it is not possible to verify the accuracy of the material damping factor using these cases.

Aside from the analytical model not incorporating damping, overall the analytical, Comp-A and Comp-C models match well in amplitudes as well as frequencies. Comp-C, with its flat circular plate geometry, is more representative of the analytical model configuration and therefore, its frequency matches better with the analytical model than Comp-A. Comp-C has a slightly larger frequency than Comp-A.

These results show the flat circular plate geometry is a good simplified model for the actual problem. However, it appears that the experimental results have a small lag in the initial part of the response when compared to the models. In addition, the frequencies of the experimental results are slightly smaller than the models. This may be due to various possibilities. For instance, there may be some nonlinear effects that the models are not accounting for, or the boundary conditions of the models may not be representing the boundary as it is in the experimental setup. In addition, the instantaneous rise in the loading can possibly introduce high frequency components into the models.

In all the cases, the maximum plate deflection occurs during the first oscillation cycle, as expected. Figures 6.15 - 6.18 show close ups of the first peaks of Figures 6.11 - 6.14, respectively. In addition, Table 6.2 provides the maximum deflections of the experimental and the three model results. For maximum deflection, there seems to be extremely good agreement between the experimental data and the three models for all cases except Case 3.

For Case 3, all the models are in good agreement, however, they overestimate the maximum experimental deflection. This indicates that there is a problem in the loading model for Case 3. After further investigation, the reason for the experimental data and models not matching well for Case 3 is because it has a small scaled distance, Z, where there is significant uncertainty in the loading parameters. This result confirms the importance and difficulty in obtaining the loading parameters for the small scaled distance region, as well as the large uncertainty in the current loading parameter values in this range.

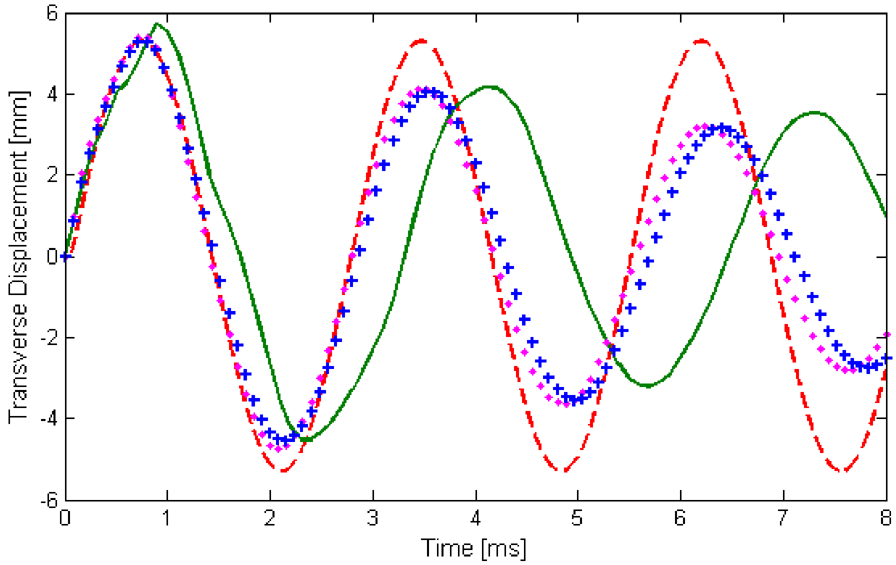

Figure 6.11: Transverse displacements of the plate center for Case 1. Results are from experimental [2] (–), analytical model (- -), Comp-A (+) and Comp-C (·). The entire loading for Case 1 ends at 0.438 ms.

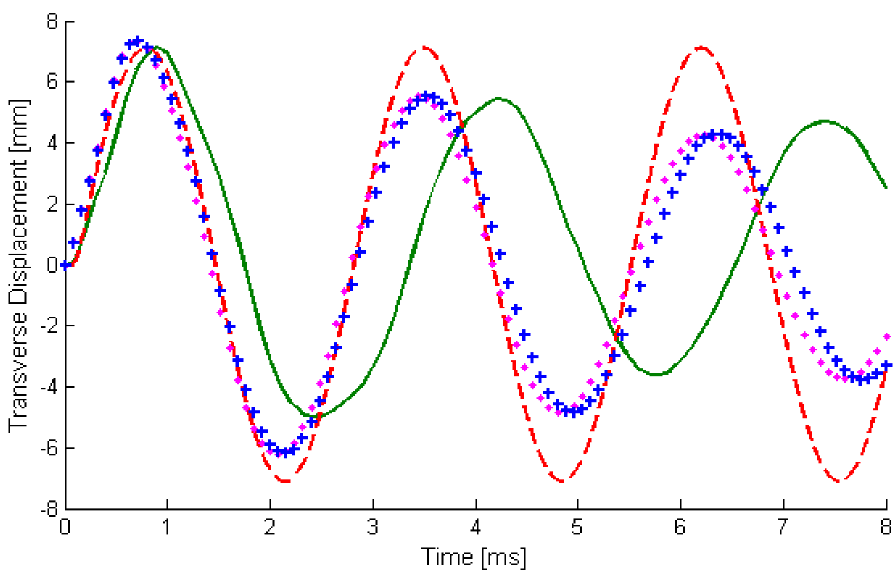

Figure 6.12: Transverse displacements of the plate center for Case 2. Results are from experimental [2] (–), analytical model (- -), Comp-A (+) and Comp-C (·). The entire loading for Case 2 ends at 0.406 ms.

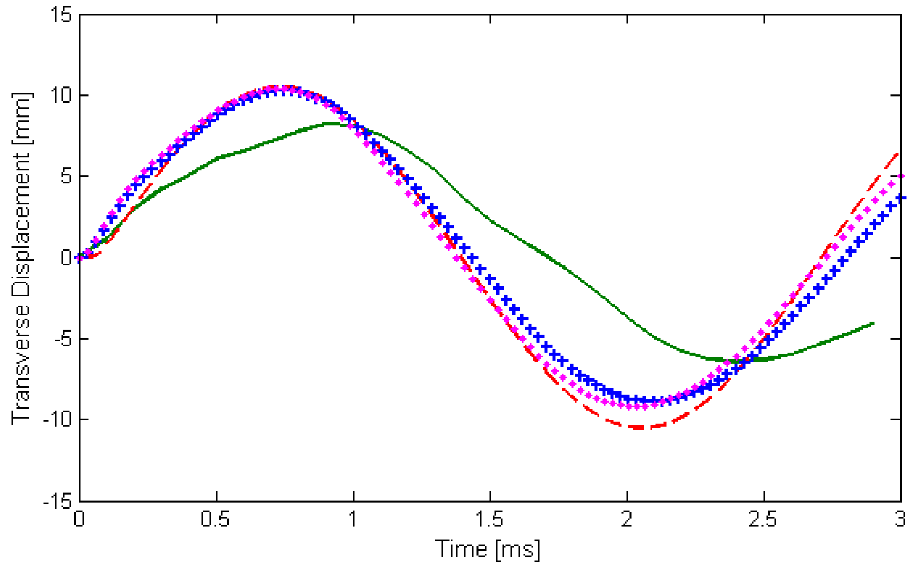

Figure 6.13: Transverse displacements of the plate center for Case 3. Results are from experimental [2] (–), analytical model (- -), Comp-A (+) and Comp-C (·). The entire loading for Case 3 ends at 0.334 ms.

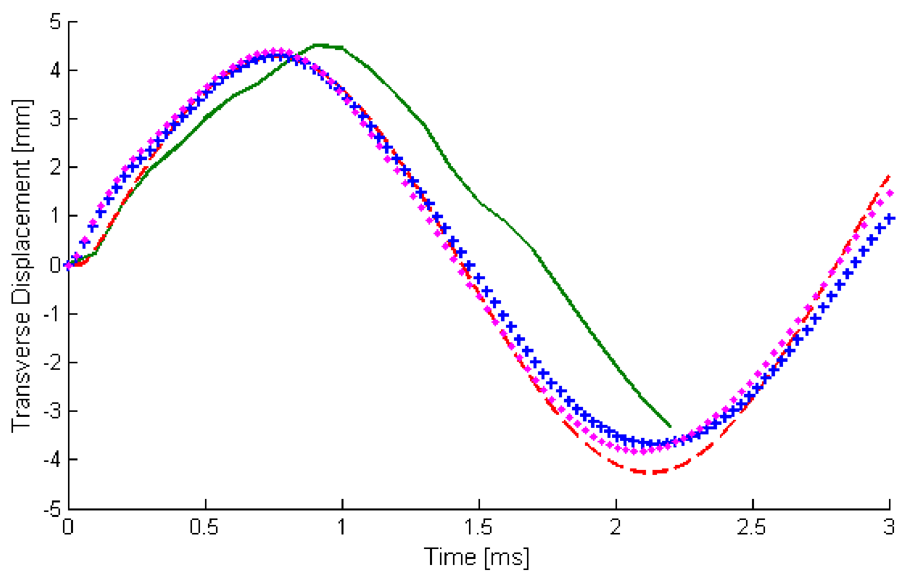

Figure 6.14: Transverse displacements of the plate center for Case 4. Results are from experimental [2] (–), analytical model (- -), Comp-A (+) and Comp-C (·). The entire loading for Case 4 ends at 0.864 ms.

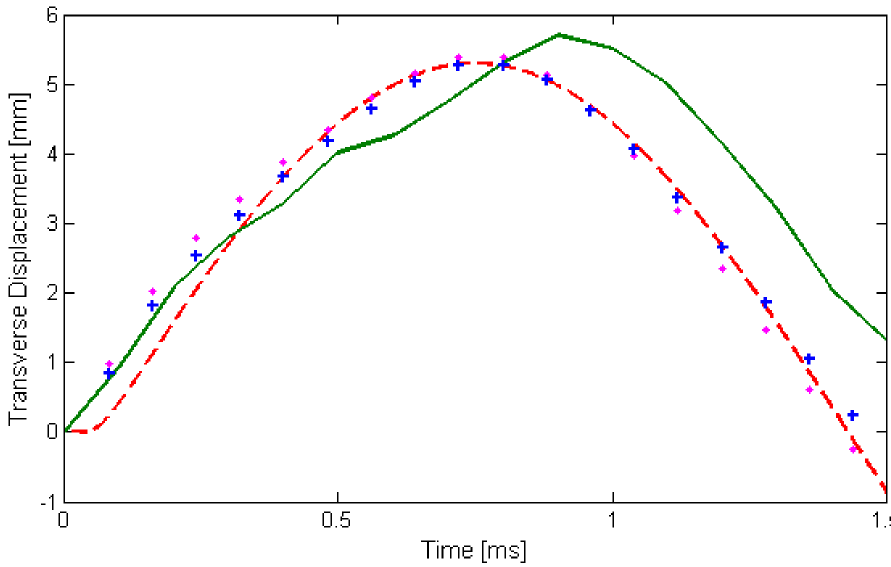

Figure 6.15: First 1.5 ms of Figure 6.11. Transverse displacements of the plate center for Case 1. Results are from experimental [2] (–), analytical model (- -), Comp-A (+) and Comp-C (·).

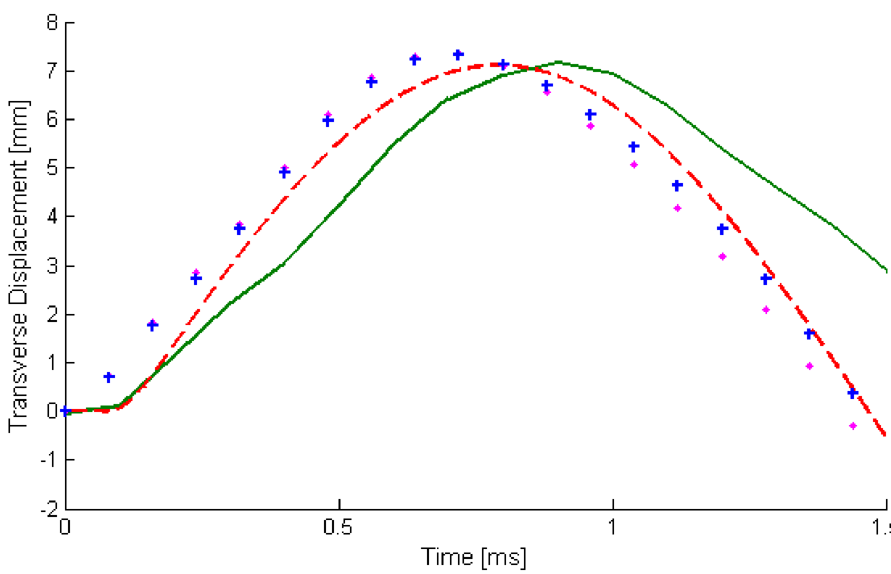

Figure 6.16: First 1.5 ms of Figure 6.12. Transverse displacements of the plate center for Case 2. Results are from experimental [2] (–), analytical model (- -), Comp-A (+) and Comp-C (·).

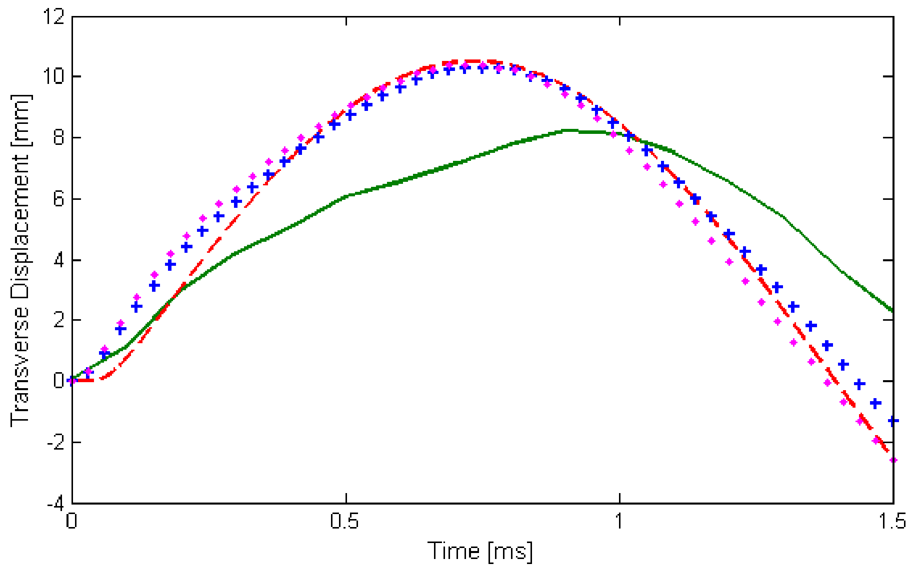

Figure 6.17: First 1.5 ms of Figure 6.13. Transverse displacements of the plate center for Case 3. Results are from experimental [2] (–), analytical model (- -), Comp-A (+) and Comp-C (·).

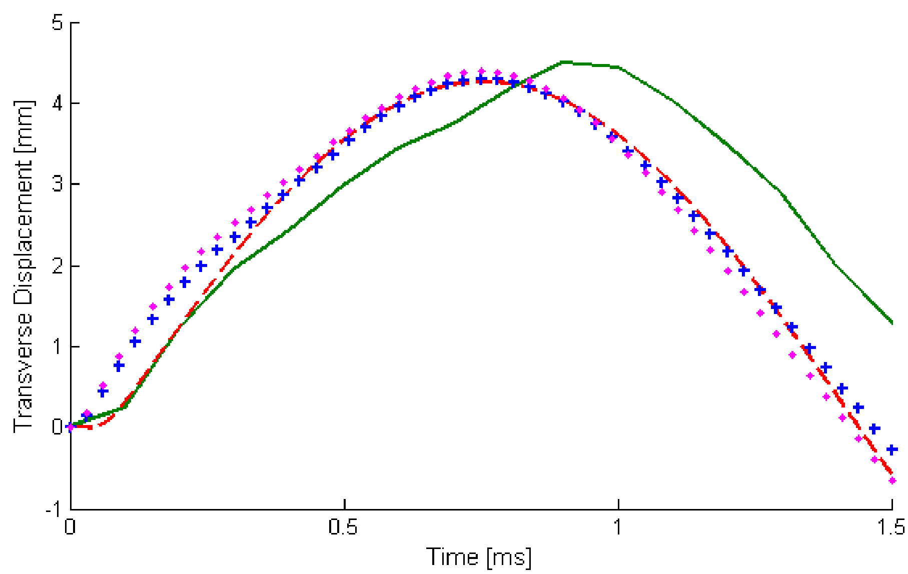

Figure 6.18: First 1.5 ms of Figure 6.14. Transverse displacements of the plate center for Case 4. Results are from experimental [2] (–), analytical model (- -), Comp-A (+) and Comp-C (·).

Case #	Experimental [2] Maximum Deflection	Analytical Maximum Deflection	Comp-A Maximum Deflection	Comp-C Maximum Deflection
1	5.71	5.30 (7.18%)	5.27 (7.71%)	5.38 (5.78%)
2	7.16	7.11 (0.70%)	7.32 (2.23%)	7.35 (2.65%)
3	8.23	10.52 (27.83%)	10.30 (25.15%)	10.40 (26.37%)
4	4.49	4.26 (5.12%)	4.29 (4.45%)	4.39 (2.23%)

Table 6.2: Max deflection of plate center for each case: experimental results [2], analytical model, computational model of actual plate geometry (Comp-A) and computational model of flat circular plate geometry (Comp-C). Units are in millimeters. Values in parentheses are the percent errors to the experimental results.

6.4 Strain at Plate Center

The Department of Homeland Security provided the principal strains at the center of the plate for Cases 1 and 2. These principal strains are in the plane of the plate surface. Since the plate's response is axisymmetric, the two principle strains along the plate surface should be the same. The experimental results for the strain are fairly close to each other, therefore only one principle strain is presented in the following results. Figures 6.19 and 6.20 show the principle strain experimental data as well as the Comp-A and Comp-C models for Cases 1 and 2, respectively. As for the deflection results, the strain results for Comp-A and Comp-C are very similar. They differ slightly from the experimental data, but not in a significant way. The experimental data has a short phase shift in the response compared to the finite element models. Figures 6.21 and 6.22 show a close up of the first three milliseconds of Figures 6.19 and 6.20, respectively.

We believe that the humps prior to the maximum peak occur when the majority of the loading on the witness plate has dissipated. These humps are observed in both the experimental results as well as the finite element models.

6.5 Uniform Loading vs Nonuniform Loading

To show the necessity of using a nonuniform loading for these near field explosions, the computational model with the actual plate configuration, Comp-A, was run for Cases 1 and 2 using a uniform load. To generate the uniform loading, the pressure loading at the center of the plate was placed uniformly on the entire plate. Figures 6.23 and 6.24 show the

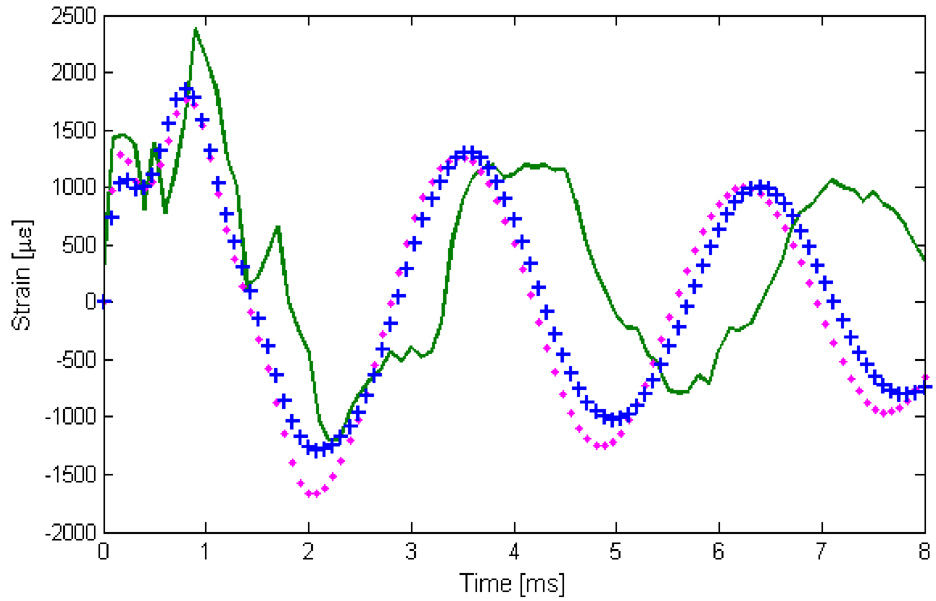

Figure 6.19: Strains at the plate center for Case 1. Results are from experimental [2] (–), Comp-A (+) and Comp-C (·).

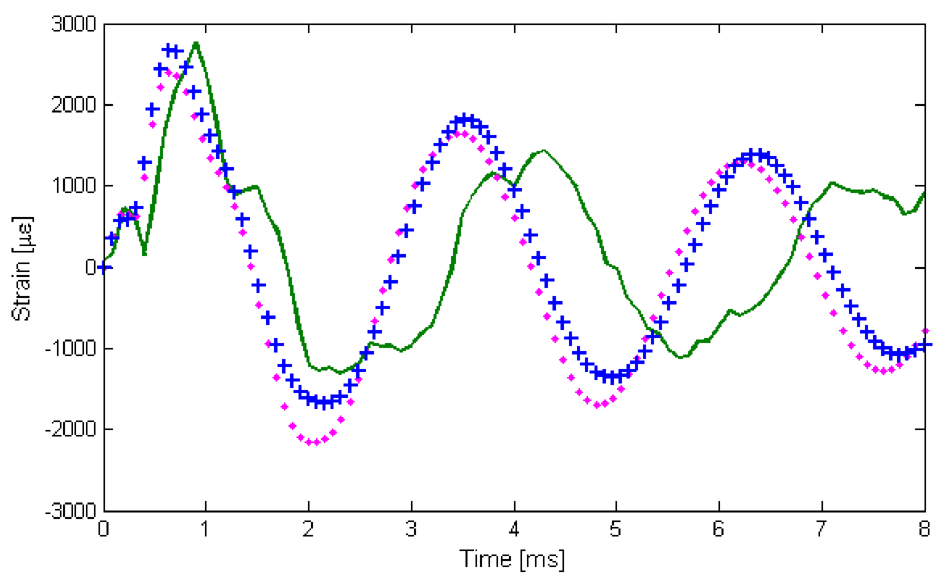

Figure 6.20: Strains at the plate center for Case 2. Results are from experimental [2] (–), Comp-A (+) and Comp-C (·).

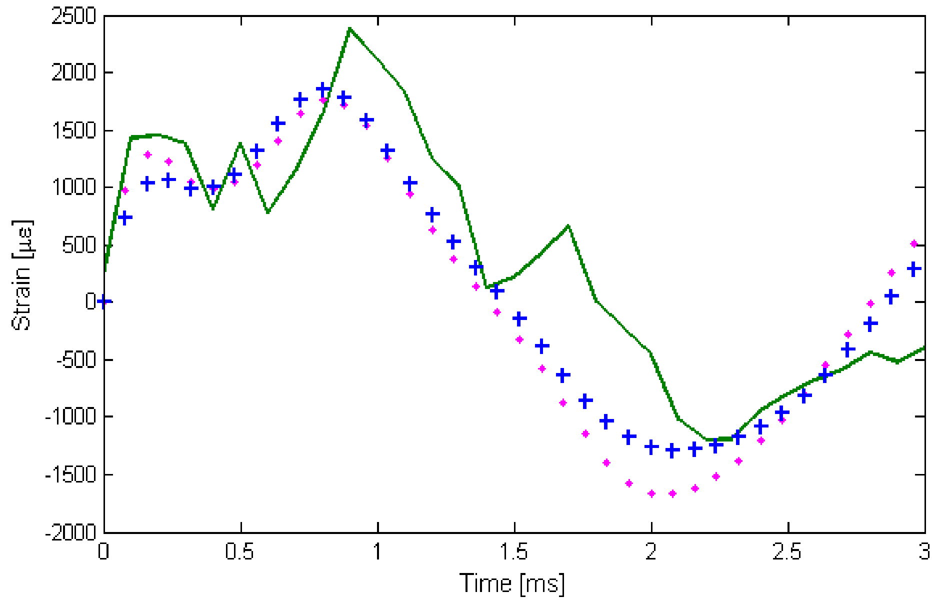

Figure 6.21: First 3 ms of Figure 6.19. Strains at the plate center for Case 1. Results are from experimental [2] (–), Comp-A (+) and Comp-C (·).

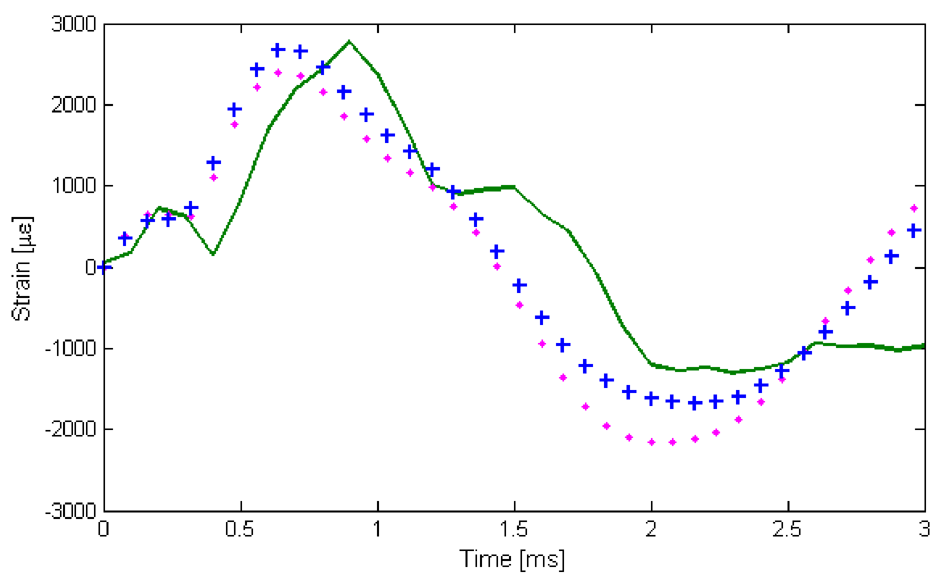

Figure 6.22: First 3 ms of Figure 6.20. Strains at the plate center for Case 2. Results are from experimental [2] (–), Comp-A (+) and Comp-C (·).

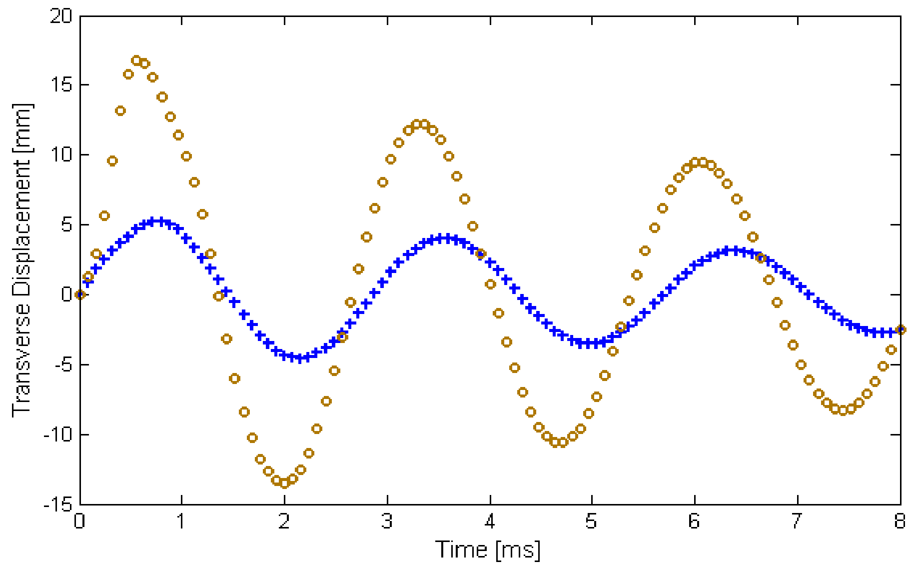

Figure 6.23: Transverse displacements of plate center for Case 1 with a uniform load (∘) and nonuniform load (+). These results were obtained from ANSYS Workbench using the actual plate model, Comp-A.

transient deflections of the plate center in response to uniform and nonuniform loadings. As expected, the uniform loading generates a much larger maximum deflection than the nonuniform loading. This larger deflection greatly overestimates the actual plate deflection given in the experiments. The uniform loading results have a slightly larger frequency than the nonuniform loading results, but they are very close.

6.5.1 Z Value Comparisons along Plate

To demonstrate the complexity of nonuniform loading, Figures 6.25 and 6.26 show a comparison between the scaled distances of Cases 1 and 2 versus distance from the center of the plate using the TNT equivalence factors for pressure and impulse. These results were obtained using the analytical model. Initially, Case 1 has a smaller scaled distance value. However, further along the plate it becomes larger than the value for Case 2. This is due to the difference in slant distance to standoff distance. The charge weight for each case remains the same, however, as one moves away from the plate's center the slant distance becomes larger. The smaller the standoff distance, the larger the ratio of slant distance to

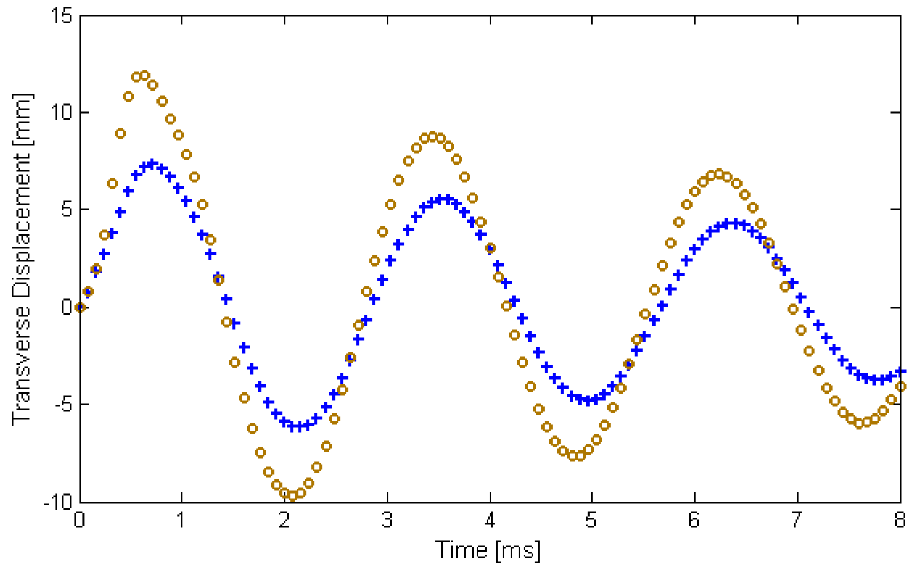

Figure 6.24: Transverse displacements of plate center for Case 2 with a uniform load (○) and nonuniform load (+). These results were obtained from ANSYS Workbench using the actual plate model, Comp-A.

standoff distance becomes as we move further away from the plate's center. In these cases, Case 1 has a smaller standoff distance than Case 2 so the slant distance of Case 1 increased faster than for Case 2, allowing the scaled distance to eventually become larger.

6.6 TNT Equivalence

To see the difference between the new loading method of using both TNT equivalence factors for impulse and pressure, versus averaging them, as do many loading models such as ConWep (see Section 3.7.1), the analytical and Comp-A models were also run with the TNT equivalence factors averaged. Figures 6.27 - 6.30 show plate center deflections with both loadings for the first three milliseconds of Cases 1 - 4, respectively. Plate center deflections for the Comp-A model using both TNT equivalence factors for impulse and pressure, which are shown in Figures 6.11 - 6.14, are not shown in these figures for clarity. In addition, Table 6.3 provides the maximum deflections for each model and case. In these figures and table, it can be seen that when the TNT equivalence factors are averaged, the plate's maximum deflection becomes slightly greater when compared to the unaveraged TNT equivalence

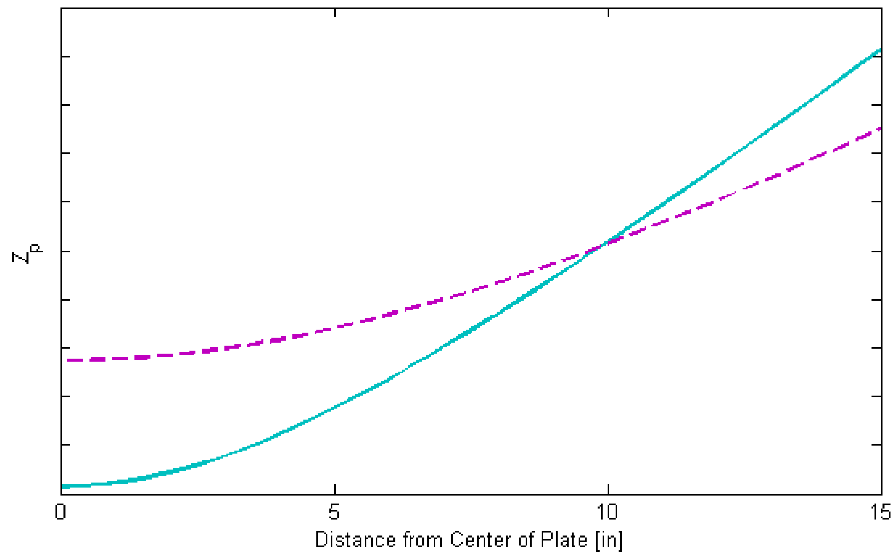

Figure 6.25: Scaled distance with TNT equivalent weight for pressure, Z_p, along the plate radius for Case 1 (–) and Case 2 (- -). These results were obtained from the analytical model.

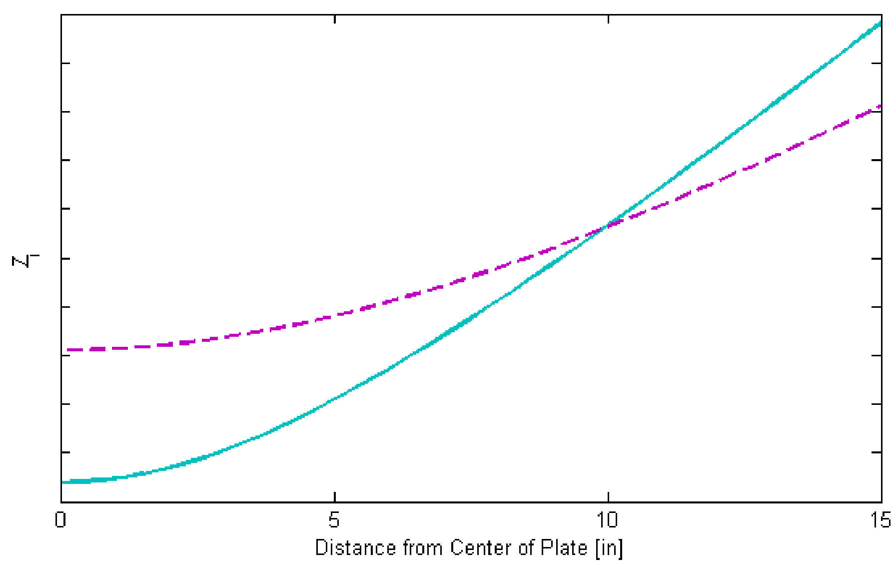

Figure 6.26: Scaled distance with TNT equivalent weight for impulse, Z_i, along the plate radius for Case 1 (–) and Case 2 (- -). These results were obtained from the analytical model.

factors for impulse and pressure.

These results are for a certain weight range of C-4. If the explosive is of a different type, with a bigger difference between the TNT equivalence factors of pressure and impulse, the difference of the plate's maximum deflection when comparing the two loading methods may be greater. In addition, if the weight of the explosive was greater, the difference in the plate's maximum deflection between the two loading methods would increase. These results show that there is a difference in the newly proposed loading model, which utilizes both TNT equivalence factors versus the methods generally used which average the two TNT equivalence factors. Since the TNT equivalence factors for pressure and impulse are experimentally obtained and have different values for different explosives, we conclude that the current approach yields a more realistic load.

Case #	Analytical Model TNT Equiv i & P Maximum Deflection	Analytical Model TNT Equiv avg Maximum Deflection	Comp-A TNT Equiv i & P Maximum Deflection	Comp-A TNT Equiv avg Maximum Deflection
1	5.30	5.61	5.27	5.62
2	7.11	7.47	7.32	7.74
3	10.52	11.17	10.30	11.00
4	4.26	4.50	4.29	4.56

Table 6.3: Max deflection comparisons using TNT equivalence for impulse and pressure vs their average value with the analytical model. ConWep along with other loading models use the average value of TNT equivalence for impulse and pressure, as opposed to the proposed loading model which uses both values individually. Units are in millimeters.

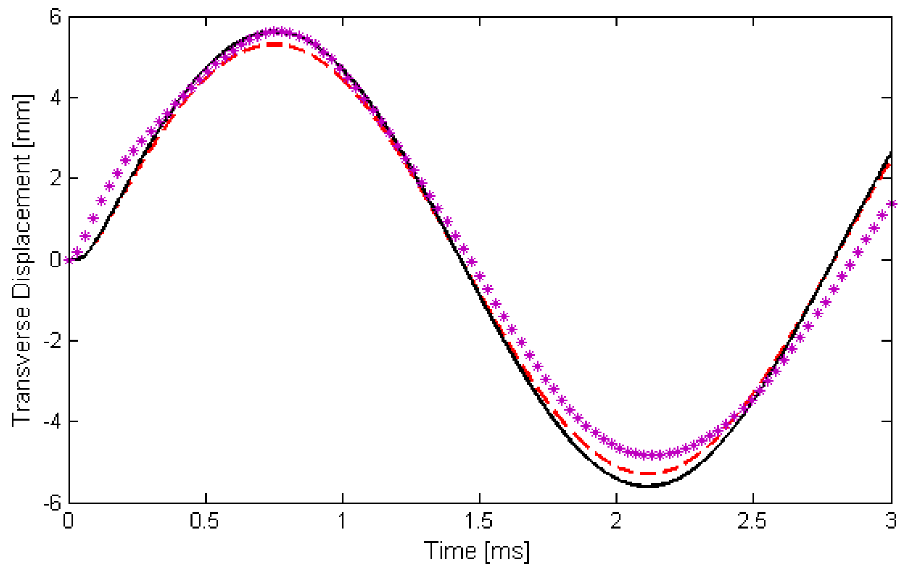

Figure 6.27: Transverse displacements of plate center for Case 1 with TNT equivalence factors for impulse and pressure (- -) and an averaged TNT equivalence factor (–). These results were obtained using the analytical model. Comp-A results (∗) with an averaged TNT equivalence factor are also shown.

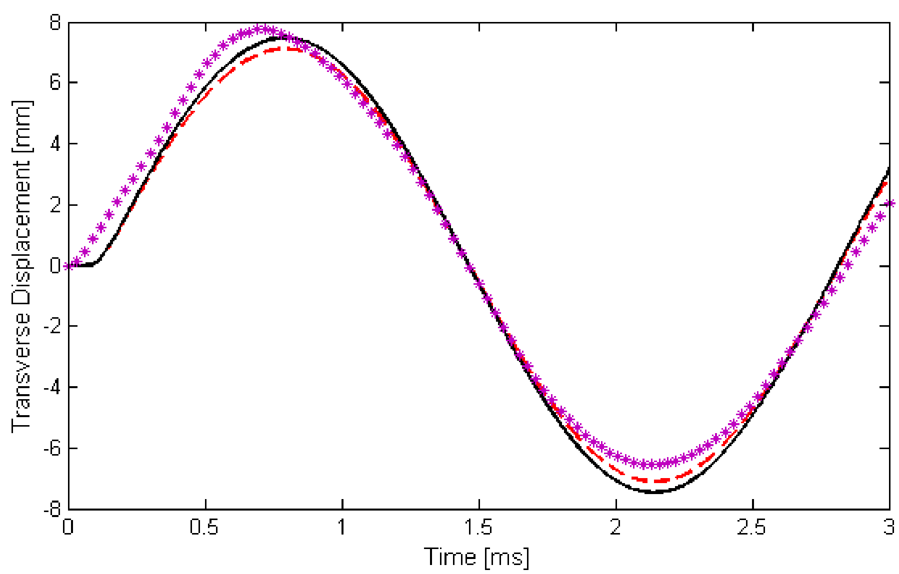

Figure 6.28: Transverse displacements of plate center for Case 2 with TNT equivalence factors for impulse and pressure (- -) and an averaged TNT equivalence factor (–). These results were obtained using the analytical model. Comp-A results (∗) with an averaged TNT equivalence factor are also shown.

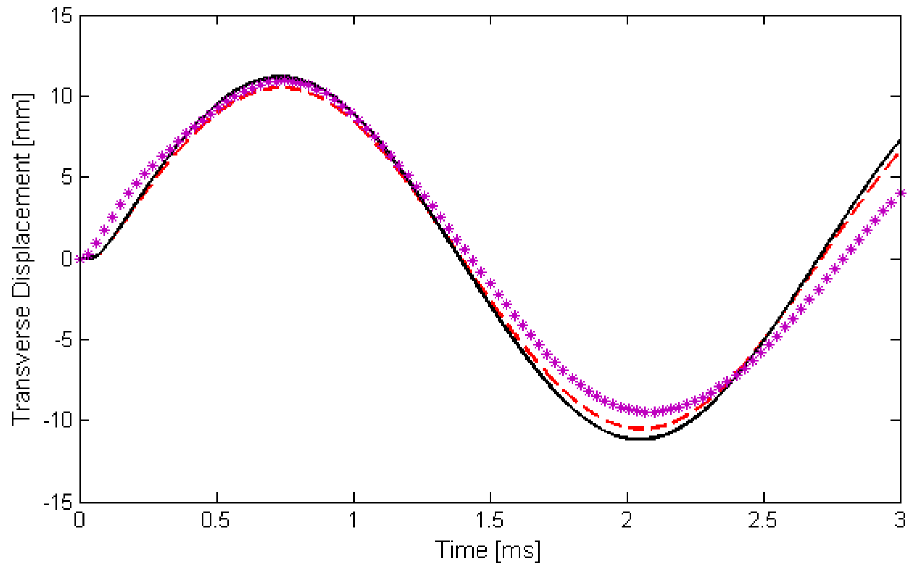

Figure 6.29: Transverse displacements of plate center for Case 3 with TNT equivalence factors for impulse and pressure (- -) and an averaged TNT equivalence factor (–). These results were obtained using the analytical model. Comp-A results (∗) with an averaged TNT equivalence factor are also shown.

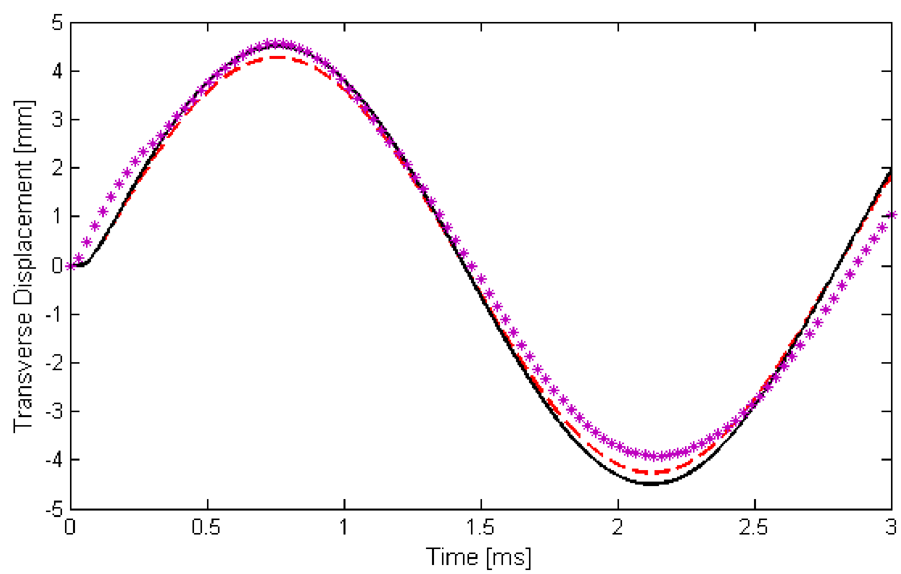

Figure 6.30: Transverse displacements of plate center for Case 4 with TNT equivalence factors for impulse and pressure (- -) and an averaged TNT equivalence factor (–). These results were obtained from the analytical model. Comp-A results (∗) with an averaged TNT equivalence factor are also shown.

Chapter 7

Uncertainty Analysis

Since the study of explosive loads inherently contains numerous uncertainties, it is appropriate to quantify these in our analyses. In particular, a sensitivity analysis of the response to various parameter values is performed. In addition, this analysis provides information on the trends of the results as each parameter is changed. Finally, a Monte Carlo scheme is implemented to determine the sensitivity of maximum plate deflection to each loading parameter's uncertainty. These studies show which parameters need to be measured more precisely than the others because their variation has more effect on plate deflection. In this chapter, all analyses utilize the analytical model.

7.1 Parameter Sensitivity

In order to calculate the sensitivity of the plate deflection to variations in structural and loading parameters, the following procedure was implemented for all cases:

1) We took actual parameter values for each case as their mean values, except for K. In order to determine the sensitivity of plate deflection to variations in K, it was decided to assign a value for K that would not represent a fully clamped or fully simply supported plate, but somewhere between the two. Therefore, for this sensitivity analysis, the mean value for K was set to 10,000,000 in lb/rad. We will denote each case that uses this new value of K with a superscript asterisk, for example, Case 1 with this new value of K will be labeled as Case 1*.

2) Taking one parameter at a time, we subtract 10% of its mean value and calculate the maximum deflection of the plate center. 10% was selected to give a realistic uncertainty level.

3) Taking one parameter at a time, we then add 10% of its mean value and calculate

the maximum deflection of the plate center.

4) For each parameter, we take the difference between the two maxima of Step 2 and Step 3.

5) The greater the absolute difference, the greater the sensitivity of maximum plate deflection to variation of that parameter.

For example, consider parameter K for Case 1*. The following steps correspond to the list from the numbered procedure listed above.

1) We set K_{mean} = 10,000,000 in lb/rad.

2) We subtract 10% from the mean of parameter K, $K_1 = 0.9 \times K_{mean} = 0.9 \times 10{,}000{,}000 = 9{,}000{,}000$ in lb/rad. We do this while keeping all the other parameter values at their mean value, their original values for Case 1*. The analytical model is then run with $K = K_1 = 9{,}000{,}000$ in lb/rad. The maximum deflection at the plate center is then recorded. In this case the maximum deflection is 7.2096 mm.

3) Next, we add 10% from the mean value, $K_2 = 1.1 \times K_{mean} = 1.1\times$ $10{,}000{,}000 = 11{,}000{,}000$ in lb/rad. The analytical model is now run with $K = K_2 = 11{,}000{,}000$ in lb/rad. The maximum deflection at the plate center is then recorded. For this run, the maximum deflection is 7.0686 mm.

4) The difference between the two runs is $7.2096 - 7.0686 = 0.1410$ mm.

5) The greater the absolute value of this difference, the more sensitive the maximum plate deflection is to variations in parameter K.

This procedure is repeated for each parameter.

Tables 7.1-7.4 show the results of this procedure for all the loading and structural parameters of Case 1* to Case 4*. These results are ordered from most sensitive to least. The order of sensitivity due to a certain parameter slightly changes depending on the case. However certain generalizations can be made.

For all the cases the plate thickness, h, is by far the parameter which causes the most sensitivity. The parameters for weight of explosive, plate radius and TNT equivalence factor for impulse generate the second to fourth most sensitivity. The plate density, Young's modulus and standoff distance are the group of parameters to produce the fifth to seventh most sensitivity. Following, the viscosity and the boundary stiffness parameters generate less sensitivity. The TNT equivalence factor for pressure is the parameter causing the least amount of sensitivity, however, it is the parameter with greatest uncertainty along with the TNT equivalence factor for impulse and the boundary stiffness.

For the loading parameters, their order of causing sensitivity from greatest to least is; weight of explosive, TNT equivalence factor for impulse, standoff distance and TNT equivalence factor for pressure. Since the TNT equivalence for impulse is one of the parameters which generate more sensitivity and typically one of the hardest to accurately measure, this study shows the need for a better understanding and more accurate measurements of this factor.

Table 7.5 shows the results of the sensitivity procedure with a $\pm 20\%$ uncertainty for Case 1*. When comparing the results from this table to those of Table 7.1, we can see that the order of sensitivity between the plate radius, a, and the TNT equivalence factor for impulse, TNT Equiv i, change. This example shows the nonlinear nature of this problem. Due to this nonlinear behavior, the statistical analysis is dependent on the case and uncertainty level.

Case 1* Parameter	-10% [mm]	$+10\%$ [mm]	Difference [mm]
h	8.3501	6.1489	2.2012
W	6.5704	7.6704	-1.1000
a	6.5816	7.6493	-1.0677
TNT Equiv i	6.5947	7.6475	-1.0528
ρ	7.4975	6.8234	0.6741
E	7.4209	6.8865	0.5344
R	7.3315	6.8993	0.4322
ν	7.2052	7.0628	0.1424
K	7.2096	7.0686	0.1410
TNT Equiv P	7.1091	7.1585	-0.0494

Table 7.1: Maximum plate deflection for -10% and $+10\%$ of the specified parameter for Case 1*. The greater the absolute difference the more sensitivity the parameter produces. TNT Equiv i and TNT Equiv P are the TNT equivalence factors of impulse and pressure, respectively. Case 1* has the same parameter values as Case 1 with the exception of K =10,000,000 in lb/rad. The deterministic run for Case 1* has a maximum plate deflection of 7.1365 mm.

Case 2* Parameter	−10% [mm]	+10% [mm]	Difference [mm]
h	11.5360	8.7092	2.8271
a	8.8164	11.0970	−2.2802
W	9.2383	10.7220	−1.4835
TNT Equiv i	9.2861	10.6690	−1.3833
R	10.6680	9.3555	1.3122
ρ	10.4810	9.5821	0.8988
E	10.3790	9.6672	0.7116
ν	10.0960	9.8986	0.1977
K	10.0990	9.9091	0.1894
TNT Equiv P	9.9427	10.0470	−0.1039

Table 7.2: Maximum plate deflection for −10% and +10% of the specified parameter for Case 2*. The greater the absolute difference the more sensitivity the parameter produces. TNT Equiv i and TNT Equiv P are the TNT equivalence factors of impulse and pressure, respectively. Case 2* has the same parameter values as Case 2 with the exception of K =10,000,000 in lb/rad. The deterministic run for Case 2* has a maximum plate deflection of 10.0008 mm.

7.2 Trends

Tables 7.1 - 7.4 show the trends in the plate maximum deflection to parameter variations. The parameters that have a negative difference in these tables have a tendency to increase the plate maximum deflection as that parameter's value increases. The parameters with positive differences reduce the maximum deflection as their value increases. Therefore, for the explosive weight, the radius of the plate or either of the two TNT equivalence factors increase, the plate maximum deflection will increase. All the other parameters will reduce the maximum deflection as they increase.

7.3 Sensitivity to Uncertainty - Monte Carlo Analysis

7.3.1 Overview

Since the measurement of loading parameters (R, W, TNT Equiv i and TNT Equiv P) are typically more difficult to measure accurately, the following analysis is performed only for the loading parameters. Using the analytical model and making one of the loading parameters random while leaving the rest deterministic, the average maximum deflection at the center of the plate is evaluated using a Monte Carlo scheme as described by Benaroya

Case 3* Parameter	−10% [mm]	+10% [mm]	Difference [mm]
h	15.3842	11.8489	3.5353
W	12.4626	14.4866	−2.0240
TNT Equiv i	12.4848	14.4649	−1.9801
a	12.5212	14.3457	−1.8245
ρ	14.0868	12.9532	1.1336
R	14.0078	13.0076	1.0002
E	13.9864	13.0395	0.9469
ν	13.6078	13.3493	0.2585
K	13.5806	13.3907	0.1899
TNT Equiv P	13.4588	13.5020	−0.0432

Table 7.3: Maximum plate deflection for −10% and +10% of the specified parameter for Case 3*. The greater the absolute difference the more sensitivity the parameter produces. TNT Equiv i and TNT Equiv P are the TNT equivalence factors of impulse and pressure, respectively. Case 3* has the same parameter values as Case 3 with the exception of K =10,000,000 in lb/rad. The deterministic run for Case 3* has a maximum plate deflection of 13.4829 mm.

[57].

The Monte Carlo procedure is a deterministic computational method that results in a converged "exact" solution obtained by taking a number of random samples and averaging them. The accuracy of this method increases as more random samples are averaged. The Monte Carlo procedure calculates the convergence of the averaged response after each computational cycle and uses a predefined criterion for convergence. By comparing the maximum deflections of the random runs to the deterministic run for each parameter, the sensitivity of maximum deflection to parameter uncertainty of all the loading parameters are calculated [58, 59]. A random parameter is considered to result in a greater sensitivity to uncertainty if the maximum deflection has a greater difference from the respective maximum of the deterministic run.

7.3.2 Probabilistic Distribution

Since blast loads are best modeled as random and there is not much information on the different loading parameters' randomness, all the random variables are assumed to have uniform distributions. Since all the random variables have the same type of distribution, it is possible to compare the accuracy of the response as a function of the level of randomness

Case 4* Parameter	-10% [mm]	$+10\%$ [mm]	Difference [mm]
h	6.8675	5.0215	1.8460
a	5.3649	6.3084	-0.9435
W	5.3880	6.2874	-0.8994
TNT Equiv i	5.4123	6.2627	-0.8504
ρ	6.1464	5.5838	0.5626
E	6.0794	5.6386	0.4408
R	6.0243	5.6594	0.3649
K	5.9086	5.7857	0.1229
ν	5.9015	5.7839	0.1176
TNT Equiv P	5.8166	5.8672	-0.0506

Table 7.4: Maximum plate deflection for -10% and $+10\%$ of the specified parameter for Case 4*. The greater the absolute difference the more sensitivity the parameter produces. TNT Equiv i and TNT Equiv P are the TNT equivalence factors of impulse and pressure, respectively. Case 4* has the same parameter values as Case 4 with the exception of K =10,000,000 in lb/rad. The deterministic run for Case 4* has a maximum plate deflection of 5.8448 mm.

for each variable.

In addition, using a uniform distribution makes it easier to specify a range of values for each random variable. As in [58, 59], the term half-range is used to describe the range between the mean value and upper and lower limit of the density, which is half of the total range in a uniform distribution. For a uniform distribution

$$\sigma = \frac{HR}{\sqrt{3}}, \tag{7.1}$$

where σ is the standard deviation and HR is the half-range. See Figure 7.1 for a visual explanation of the uniform distribution and half-range. The values of each random variable's half-range is a percentage of its mean value.

7.3.3 Random Variables

The deterministic parameter values for the different parameters being tested (standoff distance, weight of explosive, TNT equivalence factor for impulse and TNT equivalence factor for pressure) are taken to be the mean values for the Monte Carlo scheme. To obtain realizations for each parameter, a standard uniform number is generated and then transformed using

Case 1* Parameter	−20% [mm]	+20% [mm]	Difference [mm]
h	9.8626	5.3364	4.5262
W	5.9608	8.2429	−2.2821
TNT Equiv i	6.0053	8.1948	−2.1895
a	6.0019	8.1219	−2.1200
ρ	7.9199	6.5482	1.3717
E	7.7491	6.6638	1.0853
R	7.5321	6.6971	0.8350
ν	7.2688	6.9836	0.2852
K	7.2882	7.0053	0.2829
TNT Equiv P	7.0743	7.2356	−0.1613

Table 7.5: Maximum plate deflection for −20% and +20% of the specified parameter for Case 1*. The greater the absolute difference the more sensitivity the parameter produces. TNT Equiv i and TNT Equiv P are the TNT equivalence factors of impulse and pressure, respectively. Case 1* has the same parameter values as Case 1 with the exception of K =10,000,000 in lb/rad. The deterministic run for Case 1* has a maximum plate deflection of 7.1365 mm.

$$n(l) = \mu(l) + HR(l) \times (2 \times rand - 1), \tag{7.2}$$

where $n(l)$ is the realization for parameter l, $\mu(l)$ is the mean value and $HR(l)$ is the half-range, where $HR(l) = \mu(l) \times HR_f$ and HR_f is the half-range factor. The half-range factor is a number between 0 and 1, which determines the level of uncertainty for the parameter. The closer the half-range factor is to 1 the higher the level of uncertainty is for the parameter. For this study, HR_f is set to 0.1 which indicates that there is a ±10% uncertainty in the parameters. This value was selected to give a realistic uncertainty to those parameters which may have a fair amount of uncertainty in their measurements. *rand* is an internal MATLAB® function that generates a uniformly distributed random number between the range of 0 to 1. For each random variable run, the seed for the *rand* command in MATLAB® is reset. This ensures that the same sequence of random numbers are generated with each run.

7.3.4 Convergence Function

In order to determine when the solution converges to an “exact” solution, there are three criteria that need to be simultaneously satisfied. To guarantee that the first few runs do not

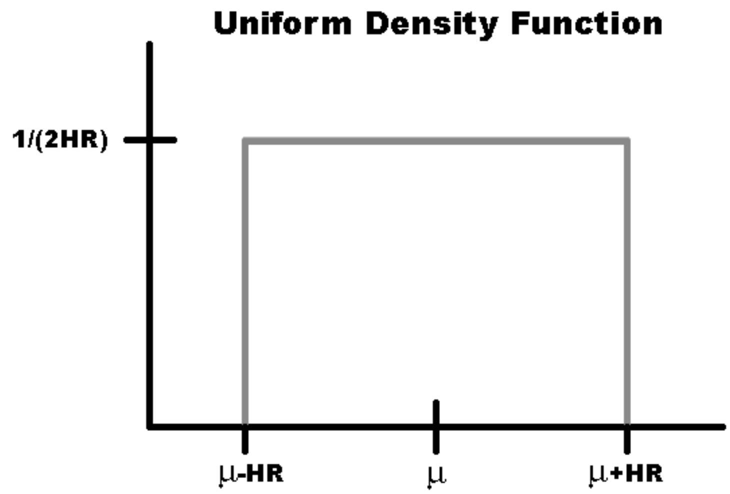

Figure 7.1: Visual representation of half-range where μ is the mean and HR represents the half-range.

satisfy the convergence function and stop the procedure due to having similar randomness, a set number of trial runs must be completed before this convergence function is taken into effect. For all the cases shown in this work, the minimum number of trial runs for the Monte Carlo procedure is 100.

For the next criterion, the newly calculated average of maximum deflection is compared to the previous average of maximum deflection. The absolute value of the difference between the current average of maximum deflection and the previous average of maximum deflection are calculated after every trial run. This value is then compared to a predefined convergence value, chosen to be 0.0001 for this study. If the difference value is less than this predefined convergence value, this criterion is satisfied, assuring us that the average value does not change by more than this predefined convergence value after adding additional runs.

The final criterion takes the absolute value of the difference between the previous average of maximum deflection and the current maximum deflection of that trial run. It then compares this value to a predetermined value. The predetermined value for this criterion is set as ten times the predefined convergence value from the previous criterion. If the difference value for this criterion is greater than the predetermined value, this criterion is said to converge. The final criterion is used to assure us that the previous criterion is not satisfied by luck or circumstance.

Mathematically, these convergence criteria are given by

$$\# \text{ of trial runs} > 100, \tag{7.3}$$

$$|Avg_c - Avg_p| < 0.0001, \tag{7.4}$$

$$|Avg_p - Max_c| > 0.001, \tag{7.5}$$

where Avg_c is the current average value of maximum deflection, Avg_p is the previous average value of maximum deflection and Max_c is the current value of maximum deflection. Once all three of these criteria are satisfied, the Monte Carlo simulation is complete.

7.3.5 Statistical Evaluations

Sensitivity to Parameter Uncertainty

The average maximum deflection for each probabilistic response is found and used to determine the sensitivity of maximum plate deflection to parameter uncertainty. For each of the four cases, the maximum of the deterministic response is calculated and used as the testing value. Table 7.6 shows the averaged maximum deflection for each Monte Carlo simulation for various parameters as well as the maximum deflection of the deterministic runs for all cases. The difference between the averaged maximum plate deflection of the random parameter to the deterministic maximum plate deflection is calculated for each specific case and tabulated in Table 7.7. The absolute value of these differences is used to determine the sensitivity of maximum deflection to that parameter's uncertainty of that parameter for the particular case. The greater the absolute value of the difference, the greater the sensitivity to the parameter's uncertainty.

Depending on the case, different parameters generate the most sensitivity of maximum plate deflection with their uncertainty. For Case 1, the TNT equivalence factor for pressure is the parameter causing the greatest sensitivity due to its uncertainty, while for Case 2 it is the standoff distance parameter. For both Cases 3 and 4, the TNT equivalence factor for impulse is the parameter causing the greatest sensitivity due to its uncertainty. These results show that this nonlinear problem's sensitivity of maximum plate deflection due to uncertainty in the loading parameters depend greatly on each specific case and therefore no single parameter's uncertainty can be singled out to always generate the greatest sensitivity of maximum plate deflection.

Case #	R	W	TNT Equiv i	TNT Equiv P	Deterministic
1	5.2771	5.2754	5.2736	5.2666	5.2993
2	7.1051	7.1148	7.1115	7.1086	7.1103
3	10.5128	10.5204	10.5314	10.5227	10.5162
4	4.2570	4.2731	4.2944	4.2793	4.2639

Table 7.6: Average maximum plate deflection with each loading parameter as the random variable. In addition, the deterministic values are also presented. Units are in millimeters.

Case #	R	W	TNT Equiv i	TNT Equiv P
1	0.0222	0.0239	0.0257	0.0327
2	0.0052	-0.0045	-0.0012	0.0017
3	0.0034	-0.0042	-0.0152	-0.0065
4	0.0069	-0.0092	-0.0305	-0.0154

Table 7.7: Deterministic maximum plate deflection minus average maximum plate deflection from Table 7.6 for each random variable and case. The greater the absolute value, the greater the sensitivity to uncertainty. Units are in millimeters.

Standard Deviation

The standard deviation for each probabilistic deflection is calculated by

$$\sigma = \sqrt{\frac{\sum_{q=1}^{N} \left(w_{max_q} - w_{max_{avg}}\right)^2}{N}}, \tag{7.6}$$

where σ is the standard deviation, w_{max_q} is the maximum deflection of iteration q, N is the total number of runs, and $w_{max_{avg}}$ is the average of the maximum deflections for all runs. This standard deviation is a measure of the spread, or scatter, of the response values. The standard deviations are shown in Table 7.8. In addition, Table 7.9 shows how many trial runs each probabilistic simulation needed to satisfy the convergence criteria.

Table 7.8 shows for Cases 1, 3 and 4, the greatest standard deviation is when the weight of explosive is the random variable. When the TNT equivalence factor for impulse is the random variable the standard deviation is slightly less to when the weight of explosive is the random variable. For Case 2, the standard deviation is greatest when the standoff distance is the random variable. This is partially due to the fact that Case 2 has the largest standoff distance compared to the other cases.

For all cases, the standard deviation is the smallest when the TNT equivalence factor for pressure is the random variable. Looking at Table 7.9, when the TNT equivalence factor for pressure is the random variable, the simulation converges with the minimum number of trail runs allowed for all cases. This helps confirm that the TNT equivalence factor for pressure does not create a large sensitivity of maximum plate deflection.

Case #	R	W	TNT Equiv i	TNT Equiv P
1	0.1268	0.2590	0.2494	0.0100
2	0.3450	0.3345	0.3124	0.0228
3	0.3057	0.5158	0.5063	0.0096
4	0.1054	0.2046	0.1951	0.0102

Table 7.8: Standard Deviation of Monte Carlo simulations. Units are in millimeters.

Case #	R	W	TNT Equiv i	TNT Equiv P
1	108	105	105	101
2	132	105	105	101
3	105	187	187	101
4	105	104	104	101

Table 7.9: Number of trial runs needed to satisfy convergence criteria for Monte Carlo simulation.

Chapter 8

Summary of Key Results and Future Work

8.1 Summary of Key Results

In this study, a nonuniform loading model was developed. This nonuniform loading model is unique as it retains both TNT equivalent factors for pressure and impulse while calculating the various loading parameters. In addition, an analytical structural model was developed to analyze a circular clamped plate's deformation when subjected to a near field explosion. This analytical model uses a new derived assumed shape. This assumed shape has one boundary parameter that represents the stiffness of a torsional spring. By varying this parameter the model can simulate fully clamped to simply supported circular plates. In addition, sensitivity analyses of the deflection due to the variation in the boundary parameter can now be performed.

Two finite element models were created to simulate the circular plate deformation. One model uses a simplified circular plate geometry while the other is an accurate representation of the actual plate used in the experimental setup. These models are able to incorporate the spatial and time dependent loading produced by the nonuniform loading model.

The results of four experiments were provided by the Department of Homeland Security to verify these models. All the models and experimental data produced axisymmetric deformations of the plate. For all models for the plate center deflection, the experimental data seems to have a slight 'lag' compared to the models. Also, all the models and experimental data match very well with the exception of Case 3, which has the smallest scaled distance. For Case 3, all the models match but they over estimate the deflection in the experimental data. This result proves that the loading parameters are not very accurate at small scaled distances.

The experimental data validates the proposed loading and structural models. It was also shown that the assumption of uniform loading greatly overestimates the maximum plate deflection caused by near field explosions.

The sensitivity of the plate maximum deflection to parameter changes was estimated. The maximum deflection is most sensitive to plate thickness, as expected. A variation in K does not cause a large sensitivity for the maximum plate deflection. Due to the nonlinear nature of this problem, the order of sensitivity due to the variation of each parameter, as Shown in Tables 7.1-7.4, can change depending on the uncertainty level used to perform the sensitivity analysis.

The sensitivity of maximum deflection to parameter uncertainties was calculated for the loading parameters. Depending on the case, different parameter's uncertainty caused the greatest sensitivity of maximum deflection.

8.2 Future Work

First of all, more cases can be compared for extensive validation of these models. Comparing more cases can also show if there are any limits for accurate results in these models. Other types of explosives, as well as other plates with different properties, can be compared and used to validate these models.

Currently, the loading model uses the Hopkinson-Cranz scaling law and loading parameter values from Figure 3.4, which are designed for explosions that occur at sea level. The loading model can be modified to use Sachs scaling law to accommodate explosions at various altitudes. In addition, the current loading model is designed for the axisymmetric plate problem and produces a 1-D spatial loading. This loading model can be modified to generate 2-D spatial loadings.

As the results of this work show, the parameter values at small scaled distances are not very accurate. This finding has been mentioned in other literature. A better set of data at these small scaled distances would be of great use. Also, finding a cutoff scaled distance where the parameter values for the current data begins to be inaccurate would be of some use.

The current loading model is performed as a preprocessor to the structural response models. This does not allow the loading model to take into account the plate's current deformation state at each point in time. The loading model can be combined with the structural response models to recalculate the loading on the plate after each time step, while taking into account the deformation of the plate. Since we are currently analyzing small deflections, this will not impact the results in this study. However, if we begin to look at plates with larger deflections or plates which reach plastic deformation, combining loading with response may be of some use.

The analytical model can be enhanced to include damping. This can be done by using a model that incorporates a damping term or by adding a damping function which manipulates the output of the current model to simulate a damped response. The analytical model can also be expanded to include plastic deformation. Currently the model is only valid in the elastic region.

Since the explosive loading is a very fast process and computationally needs short time steps to encapsulate its details, an explicit solver would be more efficient for the finite element analysis. If this finite element analysis can be redone in a program which allows for an explicit solver and a spatial and time dependant surface loading, the time needed to complete each analysis would reduce greatly.

An analysis on various time steps and the number of radial divisions can be conducted to see how the accuracy of the plate's response and the time needed to complete the analysis changes. With this analysis, an optimal time step and number of radial divisions can be chosen for further analysis.

Appendix A

Long Equations and Coefficients

$$\mathrm{f(r)} = \text{-}\ \mathrm{r}^4\, E\, h^2 (144\, K\, \mathrm{D}\, \pi\, \nu\, a^4 - 64\, r^2\, K\, \mathrm{D}\, \pi\, \nu\, a^2 + 12\, r^4\, K\, \mathrm{D}\, \pi\, \nu + 36\, K^2\, a^4$$
$$- 16\, r^2\, K^2\, a^2 + 3\, r^4\, K^2 + 432\, K\, \mathrm{D}\, \pi\, a^4 - 128\, r^2\, K\, \mathrm{D}\, \pi\, a^2 + 864\, \mathrm{D}^2\, \pi^2\, \nu\, a^4$$
$$- 256\, r^2\, \mathrm{D}^2\, \pi^2\, \nu\, a^2 + 144\, \mathrm{D}^2\, \pi^2\, \nu^2\, a^4 - 64\, r^2\, \mathrm{D}^2\, \pi^2\, \nu^2\, a^2 + 12\, r^4\, K\, \mathrm{D}\, \pi$$
$$+ 24\, r^4\, \mathrm{D}^2\, \pi^2\, \nu + 12\, r^4\, \mathrm{D}^2\, \pi^2\, \nu^2 + 1296\, \mathrm{D}^2\, \pi^2\, a^4 - 192\, r^2\, \mathrm{D}^2\, \pi^2\, a^2 + 12\, r^4\, \mathrm{D}^2\, \pi^2)$$
$$\Big/ (144\, (K + 10\, \mathrm{D}\, \pi + 2\, \mathrm{D}\, \pi\, \nu)^2\, a^8)$$

$$\mathrm{C3} = (4\, \mathrm{D}^2\, \pi^2\, \nu + 68\, \mathrm{D}^2\, \pi^2\, \nu^2 - 84\, K\, \mathrm{D}\, \pi - 436\, \mathrm{D}^2\, \pi^2 - 5\, K^2 + 12\, K\, \mathrm{D}\, \pi\, \nu^2$$
$$+ 12\, \mathrm{D}^2\, \pi^2\, \nu^3 + 3\, \nu\, K^2 + 24\, K\, \mathrm{D}\, \pi\, \nu) \Big/ (12(-100\, \mathrm{D}^2\, \pi^2 + \nu\, K^2 + 16\, K\, \mathrm{D}\, \pi\, \nu$$
$$+ 4\, K\, \mathrm{D}\, \pi\, \nu^2 - K^2 - 20\, K\, \mathrm{D}\, \pi + 60\, \mathrm{D}^2\, \pi^2\, \nu + 36\, \mathrm{D}^2\, \pi^2\, \nu^2 + 4\, \mathrm{D}^2\, \pi^2\, \nu^3))$$

$$\mathrm{f(r,\ t)} = \frac{1}{144}(-36\, r^2\, K^2\, a^4\, \nu + 16\, r^4\, K^2\, a^2\, \nu + 144\, a^6\, \mathrm{D1}^2\, \pi^2\, \nu^3 - 12\, \mathrm{D1}^2\, \pi^2\, r^6\, \nu^2$$
$$+ 12\, \mathrm{D1}^2\, \pi^2\, r^6\, \nu - 192\, \mathrm{D1}^2\, \pi^2\, r^4\, a^2 + 12\, \mathrm{D1}\, \pi\, r^6\, K - 12\, \mathrm{D1}^2\, \pi^2\, r^6\, \nu^3$$
$$- 1008\, a^6\, K\, \mathrm{D1}\, \pi + 48\, a^6\, \mathrm{D1}^2\, \pi^2\, \nu + 816\, a^6\, \mathrm{D1}^2\, \pi^2\, \nu^2 + 1296\, r^2\, \mathrm{D1}^2\, \pi^2\, a^4$$
$$+ 36\, r^2\, K^2\, a^4 + 12\, \mathrm{D1}^2\, \pi^2\, r^6 - 5232\, a^6\, \mathrm{D1}^2\, \pi^2 - 16\, r^4\, K^2\, a^2 + 36\, \nu\, a^6\, K^2 + 3\, r^6\, K^2$$
$$- 60\, a^6\, K^2 - 3\, r^6\, K^2\, \nu + 144\, a^6\, K\, \mathrm{D1}\, \pi\, \nu^2 - 144\, \mathrm{D1}^2\, \pi^2\, r^2\, a^4\, \nu^3$$
$$+ 64\, \mathrm{D1}^2\, \pi^2\, r^4\, a^2\, \nu^3 + 192\, \mathrm{D1}^2\, \pi^2\, r^4\, \nu^2\, a^2 - 64\, \mathrm{D1}^2\, \pi^2\, r^4\, a^2\, \nu - 12\, \mathrm{D1}\, \pi\, \nu^2\, r^6\, K$$
$$- 128\, \mathrm{D1}\, \pi\, r^4\, K\, a^2 + 288\, a^6\, K\, \mathrm{D1}\, \pi\, \nu + 432\, r^2\, K\, \mathrm{D1}\, \pi\, a^4 - 432\, r^2\, \mathrm{D1}^2\, \pi^2\, \nu\, a^4$$
$$- 720\, r^2\, \mathrm{D1}^2\, \pi^2\, \nu^2\, a^4 - 288\, r^2\, K\, \mathrm{D1}\, \pi\, \nu\, a^4 + 64\, \mathrm{D1}\, \pi\, r^4\, a^2\, K\, \nu^2$$
$$- 144\, \mathrm{D1}\, \pi\, r^2\, K\, a^4\, \nu^2 + 64\, \mathrm{D1}\, \pi\, r^4\, K\, a^2\, \nu) r^2\, E\, h^2\, \tau(t)^2 \Big/ ((\nu - 1)$$
$$(K + 10\, \mathrm{D1}\, \pi + 2\, \mathrm{D1}\, \pi\, \nu)^2\, a^8)$$

$$\mathrm{C6(r)} = 4\, \mathrm{h}^4\, E(20\, r^6\, K^3\, a^2 - 30\, r^4\, K^3\, a^4 + 22\, r^2\, K^3\, a^6 + 3\, a^8\, K^3\, \nu + 5\, r^8\, K^3\, \nu$$
$$- 18\, r^2\, K^3\, \nu\, a^6 + 30\, r^4\, K^3\, a^4\, \nu - 20\, r^6\, K^3\, a^2\, \nu - 80\, r^8\, \mathrm{D}^3\, \pi^3\, \nu + 480\, r^6\, \mathrm{D}^3\, \pi^3\, a^2$$
$$- 2160\, r^4\, \mathrm{D}^3\, \pi^3\, a^4 + 4336\, r^2\, \mathrm{D}^3\, \pi^3\, a^6 + 80\, r^8\, \mathrm{D}^3\, \pi^3\, \nu^3 - 940\, \mathrm{D}^2\, \pi^2\, K\, a^8$$
$$- 114\, \mathrm{D}\, \pi\, K^2\, a^8 + 40\, \mathrm{D}^3\, \pi^3\, r^8\, \nu^4 + 24\, \mathrm{D}^3\, \pi^3\, \nu^4\, a^8 + 208\, \mathrm{D}^3\, \pi^3\, \nu^3\, a^8$$

$$+ 416\,\mathrm{D}^3\,\pi^3\,\nu^2\,a^8 - 848\,\mathrm{D}^3\,\pi^3\,\nu\,a^8 - 30\,r^8\,K^2\,\mathrm{D}\,\pi - 60\,r^8\,K\,\mathrm{D}^2\,\pi^2$$
$$- 240\,\mathrm{D}^2\,\pi^2\,r^6\,\nu^3\,a^2\,K + 180\,\mathrm{D}\,\pi\,r^4\,\nu^2\,a^4\,K^2 - 108\,\mathrm{D}\,\pi\,r^2\,K^2\,\nu^2\,a^6$$
$$- 320\,r^6\,\mathrm{D}^3\,\pi^3\,\nu^2\,a^2 + 640\,r^6\,\mathrm{D}^3\,\pi^3\,\nu\,a^2 + 1920\,r^4\,\mathrm{D}^3\,\pi^3\,\nu^2\,a^4 - 1440\,r^4\,\mathrm{D}^3\,\pi^3\,\nu\,a^4$$
$$- 2016\,r^2\,\mathrm{D}^3\,\pi^3\,\nu^2\,a^6 + 1728\,r^2\,\mathrm{D}^3\,\pi^3\,\nu\,a^6 - 1800\,r^4\,K\,\mathrm{D}^2\,\pi^2\,a^4$$
$$+ 200\,r^6\,K^2\,\mathrm{D}\,\pi\,a^2 + 560\,r^6\,K\,\mathrm{D}^2\,\pi^2\,a^2 - 1088\,r^2\,\mathrm{D}^3\,\pi^3\,\nu^3\,a^6 + 1440\,r^4\,\mathrm{D}^3\,\pi^3\,\nu^3\,a^4$$
$$+ 30\,\mathrm{D}\,\pi\,\nu^2\,r^8\,K^2 + 32\,\mathrm{D}\,\pi\,K^2\,\nu\,a^8 - 144\,\mathrm{D}^3\,\pi^3\,r^2\,\nu^4\,a^6 + 240\,\mathrm{D}^3\,\pi^3\,r^4\,\nu^4\,a^4$$
$$- 160\,\mathrm{D}^3\,\pi^3\,r^6\,\nu^4\,a^2 + 188\,\mathrm{D}^2\,\pi^2\,K\,\nu^2\,a^8 - 20\,\mathrm{D}^2\,\pi^2\,K\,\nu\,a^8 + 60\,\mathrm{D}^2\,\pi^2\,r^8\,\nu^3\,K$$
$$+ 36\,\mathrm{D}^2\,\pi^2\,K\,\nu^3\,a^8 + 18\,\mathrm{D}\,\pi\,K^2\,\nu^2\,a^8 - 640\,r^6\,\mathrm{D}^3\,\pi^3\,\nu^3\,a^2 - 60\,r^8\,K\,\mathrm{D}^2\,\pi^2\,\nu$$
$$+ 60\,r^8\,K\,\mathrm{D}^2\,\pi^2\,\nu^2 + 404\,r^2\,K^2\,\mathrm{D}\,\pi\,a^6 + 2504\,r^2\,K\,\mathrm{D}^2\,\pi^2\,a^6 - 420\,r^4\,K^2\,\mathrm{D}\,\pi\,a^4$$
$$- 2616\,\mathrm{D}^3\,\pi^3\,a^8 - 40\,r^8\,\mathrm{D}^3\,\pi^3 - 560\,r^6\,K\,\mathrm{D}^2\,\pi^2\,\nu^2\,a^2 + 240\,r^6\,K\,\mathrm{D}^2\,\pi^2\,\nu\,a^2$$
$$- 80\,r^6\,K^2\,\mathrm{D}\,\pi\,\nu\,a^2 + 1320\,r^4\,K\,\mathrm{D}^2\,\pi^2\,\nu^2\,a^4 + 120\,r^4\,K\,\mathrm{D}^2\,\pi^2\,\nu\,a^4$$
$$+ 240\,r^4\,K^2\,\mathrm{D}\,\pi\,\nu\,a^4 - 1000\,r^2\,K\,\mathrm{D}^2\,\pi^2\,\nu^2\,a^6 - 200\,r^2\,K\,\mathrm{D}^2\,\pi^2\,\nu\,a^6$$
$$- 184\,r^2\,K^2\,\mathrm{D}\,\pi\,\nu\,a^6 - 120\,\mathrm{D}\,\pi\,r^6\,\nu^2\,a^2\,K^2 + 360\,\mathrm{D}^2\,\pi^2\,r^4\,\nu^3\,a^4\,K$$
$$- 216\,\mathrm{D}^2\,\pi^2\,r^2\,K\,\nu^3\,a^6 - 5\,r^8\,K^3 - 5\,a^8\,K^3) \Big/ (3\,(\nu-1)\,(K + 10\,\mathrm{D}\,\pi + 2\,\mathrm{D}\,\pi\,\nu)^3$$
$$a^{12})$$

$$\gamma = h^4\,E(-23\,K^4 + 8352\,\mathrm{D}^4\,\pi^4\,\nu^3 - 7008\,\mathrm{D}^4\,\pi^4\,\nu^2 - 856\,\mathrm{D}\,\pi\,K^3 + 144\,\mathrm{D}^4\,\pi^4\,\nu^5$$
$$+ 2000\,\mathrm{D}^4\,\pi^4\,\nu^4 - 13096\,\mathrm{D}^2\,\pi^2\,K^2 - 139312\,\mathrm{D}^4\,\pi^4\,\nu + 9\,K^4\,\nu - 297840\,\mathrm{D}^4\,\pi^4$$
$$+ 2816\,\mathrm{D}^3\,\pi^3\,\nu^3\,K + 4928\,\mathrm{D}^3\,\pi^3\,\nu^2\,K - 29696\,\mathrm{D}^3\,\pi^3\,\nu\,K + 216\,\mathrm{D}^2\,\pi^2\,K^2\,\nu^3$$
$$- 1336\,\mathrm{D}^2\,\pi^2\,K^2\,\nu + 72\,\mathrm{D}\,\pi\,K^3\,\nu^2 + 1224\,\mathrm{D}^2\,\pi^2\,K^2\,\nu^2 + 112\,\mathrm{D}\,\pi\,K^3\,\nu$$
$$+ 288\,\mathrm{D}^3\,\pi^3\,\nu^4\,K - 96608\,\mathrm{D}^3\,\pi^3\,K) \Big/ (63\,(\nu-1)\,(K + 10\,\mathrm{D}\,\pi + 2\,\mathrm{D}\,\pi\,\nu)^4\,a^2)$$

References

[1] DOE/TIC-11268. A Manual for the Prediction of Blast and Fragment Loadings on Structures. U.S. Department of Energy, Washington, DC, 1992.

[2] U.S. Department of Homeland Security (DHS) Transportation Security Laboratory (TSL).

[3] J. R. Florek. *Study of Simplified Models of Aircraft Structures Subjected to Generalized Explosive Loading*. PhD thesis, Rutgers University, NJ, 2007.

[4] W. E. Baker. *Explosions in Air*. University of Texas Press, Austin, TX, 1973.

[5] TM 5-1300. Design of structures to resist the effects of accidental explosions. U.S. Department of the Army, Washington, DC, 1990.

[6] M. W. Nansteel and C. C. Chen. High speed photography and digital image correlation for the study of blast structural response. *International Test and Evaluation Association*, 30:45–56, 2009.

[7] G. F. Kinney and K. J. Graham. *Explosive Shocks in Air*. Springer-Verlag, New York, NY, second edition, 1985.

[8] W. E. Baker, P. A. Cox, P. S. Westine, J. J. Kulesz, and R. A. Strehlow. *Explosions Hazards and Evaluation*. Elsevier Science Publishers B.V., Amsterdam, The Netherlands, 1983.

[9] P. D. Smith and J. G. Hetherington. *Blast and Ballistic Loading of Structures*. Butterworth-Heinemann Ltd., Oxford, UK, 1994.

[10] J. Henrych. *The Dynamics of Explosion and Its Use*. Elsevier Scientific Publishing Company, Amsterdam, The Netherlands, 1979.

[11] A. J. Kappos, editor. *Dynamic Loading and Design of Structures*. Spon Press, London, UK, 2002.

[12] J. R. Florek and H. Benaroya. Pulse–pressure loading effects on aviation and general engineering structures—review. *Journal of Sound and Vibration*, 284:421–453, 2005.

[13] A. M. Remennikov. A review of methods for predicting bomb blast effects on buildings. *Journal of Battlefield Technology*, 6:5–10, 2003.

[14] TM 5-855-1. Fundamentals of Protective Design for Conventional Weapons. U.S. Department of the Army, Washington, DC, 1986.

[15] A. Gupta T. Ngo, P. Mendis and J. Ramsay. Blast loading and blast effects on structures - an overview. *Electronic Journal of Structural Engineering*, pages 76–91, 2007.

[16] R. Rajendran and J. M. Lee. Blast loaded plates. *Marine Structures*, 22:99–127, 2009.

[17] F. B. A. Beshara. Modelling of blast loading on aboveground structures—I. General phenomenology and external blast. *Computers & Structures*, 51:585–596, 1994.

[18] J. M. K. Chock and R. K. Kapania. Review of two methods for calculating explosive air blast. *Shock and Vibration Digest*, 33:91–102, 2001.

[19] C. N. Kingery and G. Bulmash. *Airblast parameters from TNT spherical air burst and hemispherical surface burst.* ARBRL-TR-02555, Aberdeen Proving Ground, MD, 1984.

[20] Edward D. Esparza. Blast measurements and equivalency for spherical charges at small scaled distances. *Int. J. Impact Engng*, 4:23–40, 1986.

[21] M. J. Hargather and G. S. Settles. Optical measurement and scaling of blasts from gram-range explosive charges. *Shock Waves*, 17:215–223, 2007.

[22] J. A. Gatto and S. Krznaric. Pressure loading on a luggage container due to an internal explosion. In Y. S. Shin and J. A. Zukas, editors, *Structures Under Extreme Loading Conditions-1996*, pages 29–35. ASME, New York, NY, 1996.

[23] R. L. Veldman, J. Ari-Gur, C. Clum, A. DeYoung, and J. Folkert. Effects of pre-pressurization on blast response of clamped aluminum plates. *International Journal Impact Engineering*, 32:1678–1695, 2006.

[24] R. L. Veldman, J. Ari-Gur, and C. Clum. Response of pre-pressurized reinforced plates under blast loading. *International Journal Impact Engineering*, 35:240–250, 2008.

[25] M. C. Simmons and G. K. Schleyer. Pulse pressure loading of aircraft structural panels. *Thin-Walled Structures*, 44:496–506, 2006.

[26] Y. P. Zhao, T. X. Yu, and J. Fang. Large dynamic plastic deflection of a simply supported beam subjected to rectangular pulse. *Archive of Applied Mechanics*, 64:223–232, 1994.

[27] L. Zhu and T. X. Yu. Saturated impulse for pulse-loaded elastic-plastic square plates. *Int. J. Solids Structures*, 34(14):1709–1718, 1997.

[28] Y. P. Zhao. Saturated duration of rectangular pressure pulse applied to rectangular plates with finite-deflections. *Mechanics Research Communications*, 24(6):659–666, 1997.

[29] H. L. Brode. Numerical solutions of spherical blast waves. *Journal of Applied Physics*, 26:766–775, 1955.

[30] H. L. Brode. Blast wave from a spherical charge. *The Physics of Fluids*, 2:217–229, 1959.

[31] Charis J. Gantes and Nikos G. Pnevmatikos. Elastic-plastic response spectra for exponential blast loading. *International journal of Impact Engineering*, 30:323–343, 2004.

[32] A. J. Watson. Loading from explosions and impact. In A. J. Kappos, editor, *Dynamic loading and design of structures*, pages 231–284. Spon Press, London, New York, 2002.

[33] A. Neuberger, S. Peles, and D. Rittel. Scaling the response of circular plates subjected to large and close-range spherical explosions. Part I: Air-blast loading. *International Journal of Impact Engineering*, 34:859–873, 2007.

[34] D. Bogosian, J. Ferritto, and Y. Shi. Measuring uncertainty and conservatism in simplified blast models. In *Proceedings of the 30th Explosives Safety Seminar*, Atlanta, GA, 2002.

[35] ABS Consulting Ltd. Design, materials and connections for blast-loaded structures. Research Report 405, 2006.

[36] M. J. Hargather and G. S. Settles. Laboratory-scale techniques for the measurement of a material response to an explosive blast. *International Journal of Impact Engineering*, 36:940–947, 2009.

[37] G. F. Dargush G. J. Ballantyne, A. S. Whittaker and A. J. Aref. Air-blast effects on structural shapes of finite width. *Journal of Structural Engineering*, 136:152–159, 2010.

[38] H. F. Bauer. Nonlinear response of elastic plates to pulse excitations. *ASME J. Appl. Mech.*, 35:47–52, 1968.

[39] S. K. Singh and V. P. Singh. Mathematical modelling of damage to aircraft skin panels subjected to blast loading. *Def. Sci. J.*, 41:305–316, 1991.

[40] PDC-TR 6-01. Methodology Manual for the Single-Degree-of-Freedom Blast Effects Design Spreadsheets (SBEDS). U. S. Army Corps of Engineers, Washington, DC, 2006.

[41] UFC 3-340-02. Structures to Resist the Effects of Accidental Explosions. U.S. Army Corps of Engineering, Naval Facilities Engineering Command and Air Force Civil Engineering Support Agency, Washington, DC, 2008.

[42] D. W. Hyde. *ConWep: Conventional Weapons Effects Program.* U. S. Army, Vicksburg, MS, 2005.

[43] H. J. Goodman. Compiled free air blast data on bare spherical Pentolite. BRL report 1092, Aberdeen Proving Ground, MD, 1960.

[44] C. N. Kingery. Air blast parameters versus distance for hemispherical TNT surface bursts. BRL report 1344, Aberdeen Proving Ground, MD, 1966.

[45] R. Reisler, B. Pellet, and L. Kennedy. Air burst data from height-of-burst studies in Canada, Vol. II: HOB 45.4 to 144.5 feet. BRL report 1990, Aberdeen Proving Ground, MD, 1977.

[46] Jr M. M. Swisdak. Explosion effects and properties: Part I—explosion efects in air. NSWC/WOL/TR 75-116, Naval Surface Weapons Center, White Oaks, Silver spring, MD, October 1975.

[47] V. W. Davis, T. Goodale, K. Kaplan, A. R. Kriebel, H. B. Mason, J. F. Melichar, P. J Morris, and J. N. Zaccor. Nuclear weapons blast phenomena, Vol. IV—Simulation of nuclear airblast phenomena with high explosives (U). DASA Report 1200-IV, Washington, DC, 1973. (SECRET - FRD).

[48] N. Trefethen and Z. Battles. Chebfun. Version 3. Oxford University Mathematical Institute. http://www2.maths.ox.ac.uk/chebfun/, 2002–2010.

[49] A. Leissa. *Vibration of Plates (NASA SP-160)*. Government Printing Office, Washington, US, 1969. (reprinted 1993 by The Accoustical Society of America).

[50] R. Szilard. *Theories and Applications of Plate Analysis: Classical, Numerical, and Engineering Methods*. John Wiley, Hoboken, NJ, 2004.

[51] Y. C. Fung. *Foundations of Solid Mechanics*. Prentice-Hall, Inc., Englewood Cliffs, NJ, 1965.

[52] S. Timoshenko and S. Woinowsky-Krieger. *Theory of Plates and Shells*. McGraw-Hill, Inc., New York, NY, second edition, 1959.

[53] L. V. Kantorovich and V. I. Krylov. *Approximate Methods of Higher Analysis*. P. Noordhoff Ltd, The Netherlands, 1964.

[54] Y. Jaluria. *Computer Methods for Engineering*. Taylor and Francis, Washington, DC, 1996.

[55] www.matweb.com.

[56] W. Bottega. *Engineering Vibrations*. CRC Press, Boca Raton, FL, 2006.

[57] H. Benaroya and S. M. Han. *Probability Models in Engineering and Science*. CRC Press, Boca Raton, FL, 2005.

[58] E. Borenstein. Sensitivity analysis of blast loading parameters and their trends as uncertainty increases. Master's thesis, Rutgers University, NJ, 2007.

[59] E. Borenstein and H. Benaroya. Sensitivity analysis of blast loading parameters and their trends as uncertainty increases. *Journal of Sound and Vibration*, 321:762–785, 2009.

Vita

Elan Borenstein

1994-98 Marlboro High School, Marlboro, New Jersey

1998-2003 B.S. in Mechanical and Aerospace Engineering, Rutgers University, New Brunswick, New Jersey

1998-2003 B.S. in Mathematics, Rutgers University, New Brunswick, New Jersey

1998-2003 B.S. in Physics, Rutgers University, New Brunswick, New Jersey

2004-2007 M.S. in Mechanical and Aerospace Engineering, Rutgers University, New Brunswick, New Jersey

2007-2010 Ph.D. in Mechanical and Aerospace Engineering, Rutgers University, New Brunswick, New Jersey

2005-2006 Teaching Assistant, Rutgers University, New Brunswick, New Jersey

2006-2008 Graduate Assistant, The Center for Mathematics, Science and Computer Education, Rutgers University, New Brunswick, New Jersey

2008 Summer Instructor, Rutgers University, New Brunswick, New Jersey

2008-2010 Teaching Assistant, Rutgers University, New Brunswick, New Jersey

2009 Aerospace Nuclear Safety Engineer (Intern), Jet Propulsion Laboratory, Pasadena, California

2010- Aerospace Nuclear Safety Engineer, Jet Propulsion Laboratory, Pasadena, California

2006 E. Borenstein, "Sensitivity Analysis of Shock Loading Parameters," presented at the William J. Hughes Technical Center, Pomona, N.J., Jan. 10, 2006.

2007 E. Borenstein, "Brief Overview of: A Sensitivity Analysis of Simplified Blast Loading Parameters to Uncertainty," presented at Rutgers University, Piscataway, N.J., Mar. 14, 2007.

2007 E. Borenstein, "Sensitivity Analysis of Blast Loading Parameters and Their Trends as Uncertainty Increases," presented at the 4th International Aviation Security Technology Symposium, Washington, D.C., Nov. 28, 2007.

2007 E. Borenstein and H. Benaroya, "Sensitivity Analysis of Blast Loading Parameters and Their Trends as Uncertainty Increases," in proceedings of the 4th International Aviation Security Technology Symposium, Washington, D.C., Nov. 28, 2007.

2009 E. Borenstein, "General Overview of Current Work Towards a Blast Loading Inverse Model," presented at the Aviation Security Meeting at CAIT/Rutgers University, Piscataway, N.J., Oct. 30, 2009.

2009 E. Borenstein, "Update to DHS on the Forward Problem of Nonuniform Explosive Loadings on Circular Plates," presented to TSA at William J. Hughes Technical Center, Pomana, N.J., Nov. 19, 2009.

2009 E. Borenstein and H. Benaroya, "Sensitivity Analysis of Blast Loading Parameters and Their Trends as Uncertainty Increases," Journal of Sound and Vibration, 321:762-785, 2009.